Physics performance studies for the ALICE experiment at the CERN LHC

J. Daniel Tapia Takaki

Thesis submitted for the degree of
Doctor of Philosophy

Particle Physics Group,
School of Physics and Astronomy,
The University of Birmingham.

17th December, 2007.

Synopsis

A Large Ion Collider Experiment (ALICE) will study the strong interaction sector (QCD) of the Standard Model at the CERN Large Hadron Collider (LHC). ALICE has been designed as a general-purpose heavy-ion detector in order to address the most interesting phenomena of strongly interacting matter and the quark-gluon plasma (QGP) at extreme values of energy density and temperature in nucleus-nucleus collisions.

ALICE has a unique design with a very different optimisation of its physics performance relative to the dedicated proton-proton LHC experiments. A physics programme on the proton-proton runs at the top LHC energy has also been prepared for ALICE with the aim to provide a reference data for the heavy-ion run but also to address a series of strong-interaction topics that will complement the studies of other LHC experiments.

The ALICE experiment was approved in 1997, and its detectors have been built by an international collaboration which currently includes over 1,000 physicist and engineers from 102 institutes in 30 countries. Most of the detector systems will be installed and ready for data taking by mid 2008 when the LHC is scheduled to start operation, while the high luminosity ion runs are expected in 2010 and after. This thesis presents two physics performance studies in ALICE: ϕ meson and di-lepton production in proton-proton collisions. Additionally, it describes a systematic test of cable signal transmission in the ALICE trigger system.

Abstract

A Large Hadron Collider Experiment (ALICE) at the CERN Large Hadron Collider (LHC) will explore a primordial state of matter that existed in the early Universe. Resonance production at the LHC is of great interest in the study of the phase state of hadronic matter known as a Quark Gluon Plasma (QGP). Results are presented on the prospects for $\phi(1020)$ meson production from LHC start-up to optimal running conditions in pp collisions. A careful analysis of background subtraction methods with particular attention to ϕ meson production during the first physics run is also presented. A discussion about the discrepancies between different versions of the PYTHIA event generator in charged-particle multiplicity and its implications in ϕ production is given.

An overview of the physics of strongly interacting matter at high energy densities, the QGP signatures and experimental results from previous experiments in the field of heavy-ion physics is given. The ALICE experimental apparatus, detectors and systems are briefly described as well as the results of performance studies on tracking, vertex and particle identification.

The key features of the ALICE trigger system, and the synchronisation of trigger inputs are discussed. A description of a systematic test of cable signal transmission that allows bit-error rate (BER) measurements is also given. A feasibility study of the electromagnetic process $pp \to ppe^+e^-$ at central rapidities in ALICE is also presented.

Author's contribution

ϕ meson production in pp collisions at $\sqrt{s} = 14$ TeV

All work presented in this thesis relating to the ϕ meson production from the ALICE simulated data set, produced by myself and obtained by the ALICE collaboration in the data challenge productions of years 2004, 2005 and 2006, is my own. However, due to the collaborative nature of experimental High Energy Physics the analysis makes use of the analysis software framework (AliRoot), currently in development, available to all within the collaboration.

I have developed the software and strategies in order to carry out a performance study of ϕ meson production, for which I have been responsible in the ALICE Physics Working Group 2 ("Soft-Physics") over the last three years. More specifically, I have estimated the signal significance and signal-to-background ratio of the ϕ meson produced in pp collisions, by optimising the selection criteria needed to reconstruct this particle. I have been responsible for developing the strategies of this selection and its implementation within the analysis software in order to make estimations from LHC start-up to optimal running conditions. I have compared the charged-particle multiplicity from different extrapolations to LHC energies in pp collisions from two currently used versions of the PYTHIA event generator, particularly to understand its implications in ϕ meson production and the origin of any discrepancies.

Although not presented in this thesis, I have studied ϕ meson production in Pb-

Pb collisions using the data sample of the data challenge production 2004 prepared by the ALICE collaboration. Some of these results can be found in my Mid-term report.

Two conference posters, based on results on the ϕ meson study, were awarded prizes. The first of them at the Annual Particle Physics Conference 2006, that was held at the University of Warwick, and another one at the Birmingham Graduate School Poster and Networking Conference 2007. Some preliminary results were published in *J. Phys. G* **35** (2008) 044058. This as part of the proceedings contributions to the International Conference on Strangeness in Quark Matter 2007, that was held in Slovakia.

Lepton-pair production at central rapidities in pp collisions at $\sqrt{s} = 14$ TeV

I have undertaken a feasibility study of the electromagnetic process $pp \rightarrow pe^+e^-p$ that can be used as a luminosity monitor in ALICE. Using a signal sample prepared by my colleagues, I estimated the number of events for one normalised year of the signal after the full-simulation method along with a comprehensive study of potential backgrounds both at the level of generation and reconstruction.

A systematic test of cable signal transmission

I have implemented the software in the ALICE trigger system that controls the timing logic that deals with bit-error rate measurements. I was also responsible for carrying out various measurements of the so-called LVDS tester, and I also wrote the user manual for this software.

Daniel Tapia Takaki.

To my parents:

Ofelia and Daniel.

Acknowledgements

I would like to take this opportunity to acknowledge all those colleagues, friends and family who have supported me during this time. I have been looking forward for this moment as there are so many things that remind me how much thanks I owe to so many people (I will try not to waffle).

Birmingham ALICE group My letter starts firstly recognising the great help and support that I have received from my supervisors Dr. Orlando Villalobos Baillie and Dr. David Evans. Both of them have been exceptionally generous with their time and support over the past three years. I thank you Orlando for being the oracle on carrying out research in the Birmingham ALICE group. I am deeply indebted to you for your help and always wise discussions. Without a doubt, this thesis wouldn't be the same without your help and patience during the proofreading of this thesis. I thank you David for your generosity and for your support in difficult times, and for have invited me to your parent's house for Christmas 2004.

I would like to thanks the heavy ion group at Birmingham: Dr. David Evans, Dr. Orlando Villalobos Baillie, Dr. Gron Jones, Dr. Roman Lietava, Dr. Cristina Lazzeroni, Dr. Pedja Jovanovic, Mr. Anton Juskon, Dr. Anju Bashin, Dr. Marian Krivda, Prof. John Kinson, and Dr. Frank Votruba. I would also like to thanks all the present and past ALICE students: Steve Bull, Paul Bacon, Richard Platt, Liam

Daniel, and Hannah Scott. The new students cannot escape to be acknowledged too, namely Zoe Matthews, Sparsh Navin and Ravjeet Kour. The help of all of them both during the discussion at weekly meetings make my PhD a very good academic experience. More than anything, I would like to thank them for giving me the confidence to take an active role at weekly meetings, CERN and conference talks.

I am indebted to Pedja, Anton, Roman, Orlando and Marian for working with me in a trigger project. Working on a trigger project was something that I always wanted to get involved with, and only thanks to their willingness to supervise me at CERN this project was crystallied, and was successfully completed. Special thanks also to Cristina for being actively involved in the thesis proofreading. Thanks also to Gron for his motivational chats and proofreading too.

ALICE collaboration and colleagues I have been very lucky to work for the ALICE Collaboration within the CERN's Large Hadron Collider project. A note of thanks to Karel Šafařík, Andreas Morsch, Peter Hristov, Juri Belikov, Federico Carminati, Boris Hippolyte and Boris Batiounia for their help in times when no many people where involved in physics performance studies. I would like also to thanks Christian Kuhn, Luciano Ramello for their comments during so many physics working groups meetings at CERN. Additionally, although not a member of the ALICE collaboration, a special thanks to Prof. Torbjorn Sjöstrand for his help on understanding different features of PYTHIA. I would like also to thanks Dr. Darious Bocian for the discussions at CERN on the dilepton production study presented in this thesis.

Birmingham Particle Physics group I would like to thanks Prof. Peter Watkins and Prof. Dave Charlton for offered me a place in the Birmingham group. Additionally, a special thanks to Ms. Norma Simpson and Dr. Alan Watson for helping me in the admission process. Many thanks to Dave and Norma for the exchange of emails for almost 9 months prior to my take up as a PhD student. In my very first arrival to Birmingham, Prof. Peter Watkins was waiting for me at the airport. Not only he gave me a lift that day, but without a doubt he has given me lots of advice in general matters during these years. A special thanks must also go to Dr. Lawrie Lowe, who truly deserved a paragraph in this letter for his computing support over past the years. I would also like to thanks Dr. John Wilson for invited me on spark chamber visits to local schools. Thanks also to Dr. Paul Newman for invited me to take part on the 4th year particle physics talks during the past three years.

Too numerous to list here Moving out from Mexico to the United Kingdom for my studies was something that required me not only to adjust my watches but also my entire life. A special thanks to my dear helpful friends that throughout the years have helped me to cope with such a transition in my life, always attempting to tackle my workaholism.

I would like to thanks Liam Daniel for always keeping up with my tea-drinking habits, for helping on producing some of the good schematic diagrams shown on this thesis, and for so many other things. I would like also to thanks his parents, Pam and Roger, for all the moral support. I would like to thanks my friends from Bury St. Edmunds, namely Glenn, Alex and Ray who all made me feel part of Bury. Thanks also go to Louise and Liam who have prepared so much tea and dinner for me.

I would like also to thanks my officemates: Tamsin Moye for her office discussions, Richard Platt for being sometimes so mysterious and for all the physics discussions too, Paul Bacon for all his footie chats, Steve Bull for his admirable determination and useful advice, and Hannah Scott and Dimitri Typaldos for providing with good company. A special mention also go to Pablo del Amo Sanchez who had made sure that my Spanish remains to good standards, thanks to so many interesting discussions that I am beginning to miss. I would like to thanks Richard Booths, Rachel Shaw-West, Chris Curtis, Mark Stockton, Neil Collins, Martin Gallacher, David Hadley. Special note of thanks to Chris for setting up the "postgraduate day out project" and for looking after my cactus. Thanks also to Mark, who has invited me to his Church, for staying late sometime while I was writing up. If there is something that I am not too grateful about my officemates is that none of them needed my blender, despite it is such a good one. I want to thanks Yves Coppens for has offered me a place to say when I was homeless, and for all the discussions, not to mention all the Belgian chocolates he has given me.

I would like to thanks my friends from Jarrat Hall during my first year, namely Nancy, Hector, Panos, Maria, Maria from Cyprus, and Feras. Not only they prepared those delicious Greek dinners, but they kept sending me so much Greek products after they all went back to their countries. I also would like to thanks Oliver and his family for making the visits to town a fun thing to do while they were in Birmingham. Thanks again to Nancy for her inspiration during her second year in Birmingham. Last, I better not forget all these anonymously, randomly met people that provided me with a such a warm welcome to Birmingham and to this Country. I am sure they will appreciate this small dedication.

Notes of thanks that are entirely unavoidable I would like to thanks the UK Overseas Research Students Award Scheme (ORSAS), the University of Birmingham, and the European Union who all partially funded my PhD studies. The EU support came from the Alβan scholarship programme (grant number E04D039028MX). Thanks also to the Universidad de Sonora for its flexibility regarding the date of my final exams during my master studies. I am grateful for use of the computing facilities of the University of Birmingham, the e-Science cluster, and the CERN facilities as well. They have helped in carrying out the research work described in this thesis.

On a more personal basis, I would like to thanks my family who whatever the weather, it is always there supporting me. In particular, thanks to my brothers David and Alan, to my grandfather Rafael Takaki, and to my auntie Tía Yoya for their moral support and motivation throughout my life. Finally, but certainly not least, thanks to my parents Ofelia and Daniel. This thesis is dedicated to you both. I have learnt the values of determination and hard work by watching you. Thank you.

J.D. Tapia Takaki.

Contents

List of Figures

List of Tables

Chapter 1

Introduction to heavy-ion physics

This first chapter presents a general introduction to the physics of strongly interacting matter under extreme conditions of temperature and energy density: the physics of ultra-relativistic heavy-ion collisions. This introduction is intended for non-experts of this field. This chapter also provides an overview of the physics role of ALICE at the Large Hadron Collider (LHC). It concludes with an outline for the rest of this thesis. A more detailed description of the topics covered here is given in Chapter 2.

1.1 Quark-gluon soup

It is believed that in the very early Universe, about 10 μs after the big-bang, today's ordinary hadronic matter (i.e. the hadronic matter composed by mesons and baryons - see section 2.1) existed under extreme conditions of energy density and temperature in the form of a deconfined state of quarks and gluons [1], a Quark Gluon Plasma (QGP). For more than 20 years, experimentalists have been trying to re-create such physics system (or "little-bangs") under laboratory conditions. To achieve this, they have been colliding atomic nuclei (usually referred as heavy-ions) at very high energies. Such reactions are known as ultra-relativistic heavy-ion collisions; normally the collision takes place using the heaviest nuclei available, say lead (Pb) or gold (Au), as a way to access a larger volume of matter relative to more elementary particles (protons). It is only in these ultra-relativistic collisions that sufficient energy densities lasting long enough for a phase transition to a QGP phase can occur [2].

To put this down in numbers, let us consider the energy density and its corresponding pressure during the early Universe (about 10 μs after the Big Bang):

$$\begin{aligned} \epsilon_{\mathrm{early-Universe}} &\simeq 1\,\mathrm{GeV\,fm^{-3}} \\ &= 1.8\times 10^{15}\mathrm{g\,cm^{-3}}, \end{aligned} \tag{1.1}$$

$$\begin{aligned} \mathrm{P}_{\mathrm{early-Universe}} &\simeq \frac{1}{3}\,\epsilon_{\mathrm{early-Universe}} \\ &= 0.52\times 10^{30}\,\mathrm{bar} \end{aligned} \tag{1.2}$$

While, on the other hand, the energy density in a normal nucleus is given by:

$$\epsilon_0 = \frac{\mathrm{m_N}}{\mathrm{V_N}} = 0.17\,\mathrm{m_N\,fm^{-3}} \tag{1.3}$$

where $\mathrm{m_N}$ is the mass of the nucleon, which means that $\epsilon_0 \sim 0.16$ GeV fm^{-3} [2].

In previous ultra-relativistic heavy-ion (HI) experiments at CERN, energy densities in excess of 1 GeV fm^{-3} have already been achieved. The CERN press office released a statement in February 2000 stating [3]: *A common assessment of the collected data leads us to conclude that we now have compelling evidence that a new state of matter has indeed been created, at energy densities which has never been reached over appreciable volumes in laboratory experiments before and which exceed by more than a factor 20 that of normal nuclear matter. The new state of matter found in heavy-ion collisions at the SPS features many of the characteristics of the theoretically predicted quark-gluon plasma.*

At the time of this statement, the properties of this state of matter were not fully understood, and additional experiments at higher energies were required to investigate this further.

1.2 The phase diagram of hadronic matter

Before introducing the experimental and theoretical results related to a QGP phase, it is worthwhile explaining where the QGP is located in the phase diagram of strongly interacting (QCD) matter. There are two variables that are normally used to describe the phase diagram of QCD matter; these are the temperature (T) and the baryonic chemical potential μ_B, where μ_B is essentially a variable that reflects the net quark density, i.e. the number of quarks minus the number of antiquarks per unit volume. The phase diagram is shown in figure 1.1, showing two distinct phases of hadronic matter and the QGP phase.

Ordinary hadronic matter exists at low temperature and for values of μ_B close to that of the proton. However, at higher values of T and at higher μ_B, the region of QGP appears. The phase transition between normal hadronic matter and the QGP phase can be seen clearly on this diagram. The solid line represents the phase boundary where the phase transition is believed to be of first order. However, at low μ_B it is believed that a cross-over region from hadronic to quark matter exists. Between this and the phase boundary, a "critical point" should exist [4].

What is important to remark here is that hadronic matter can enter the QGP region only at very high temperatures or densities. If the nuclei are compressed without increasing the temperature of the system, the aftermath of such a process will be located on the right of the diagram, as the volume available of the system has been reduced although the net number of quarks remained the same. Hence, the process of heating the matter moves the system upwards on the diagram. In other words, the QCD vacuum undergoes a melting process, in a way that the quarks and gluons presented in such hadronic matter become free due to the QGP phase.

In addition, there are some further points of interest on the QCD phase diagram. The figure 1.1 also shows that the QGP phase should have existed in the primordial Universe (with very low net baryon density) and in neutron stars (with very high baryon density), which are about 10^{14} times more dense than the Sun. The order of the phase transition as predicted in QCD is beyond the scope of this review.

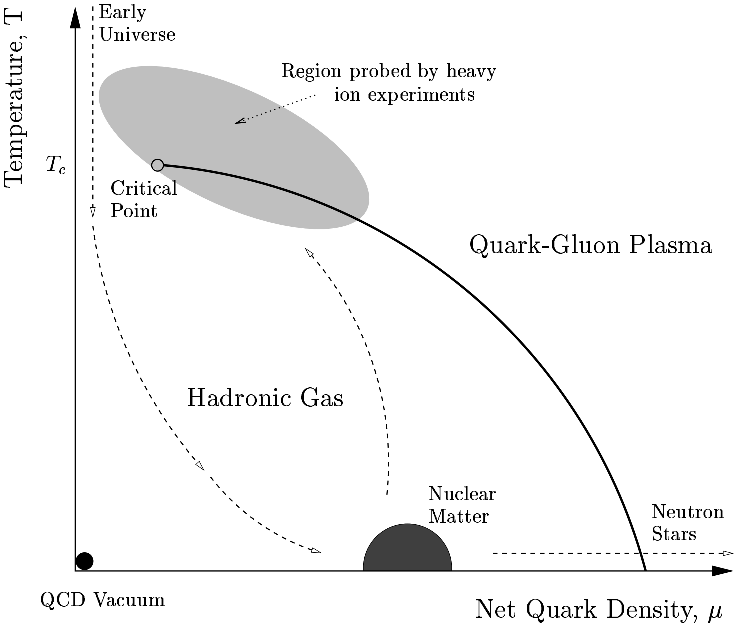

Figure 1.1: Phase diagram of hadronic and partonic matter in the temperature (T) and baryon chemical potential (μ_β) plane. The solid line represents the phase boundary where the phase transition is believed to be of first order. (Courtesy of S.A. Bull [5].)

By colliding heavy ions at very high energy one would expect to reach and exceed the critical energy density. If so, the system will then undergo a phase transition into a QGP. The formation of a QGP phase is expected to occur about a temperature of T $\sim$ 170 MeV. Hence, in a QCP phase, as in the primordial Universe, the temperature exceeds $2.2\times\ 10^{12}$ K, which is about 150,000 times hotter than the core of the Sun.

Ultra-relativistic heavy ion experiments are designed to search in the shaded region shown in figure 1.1 where the QGP phase transition is expected to take place. Thus, the focus of heavy-ion physics is the study and understanding of the macroscopic properties, and collective phenomena emerging from ultra-relativistic nucleus-nucleus collisions. This is achieved by modelling the strong interaction theory of elementary-particle physics.

1.3 Fireballs

As mentioned earlier, ultra-relativistic heavy-ion collisions are expected to create conditions similar to the early Universe. Figure 1.2 shows a visualisation of the heavy-ion collision between two lead nuclei leading to a QGP phase. The systems created in these collisions are referred to as *fireballs*, i.e. a spatially localised drop of highly excited, hot and dense hadronic matter [2][1].

As in the big-bang model, fireballs expand due to the high internal pressure [2]. However, there are also several differences between them; for example fireballs evolve much more rapidly than is the case in the evolution of the Universe. Since the nuclear size is about 6 fm and the speed of the expansion is about 0.6 times the speed of light, the life span for these fireballs is $\tau \sim 3 \times 10^{-23}$s. In the case of the early Universe, however, the QGP phase lasted $\tau \sim 10\ \mu$s [2].

From about 10μs after the Big Bang, the hot "soup of quarks and gluons" was transformed back into a dense system of hadronic matter called a hadron gas. However, it is believed that there could be a "mixed phase" between a QGP phase and a hadron gas, which could be probed experimentally by studying unstable particles such as resonances because their lifetime are comparable to that of the QGP (see chapter 8).

Therefore, the fireballs are believed to undergo various stages of evolution in terms of space and time. In general, the composition of the emitted hadrons is governed by the chemical freeze out period, defined as the moment when the inelastic

---

[1] The concept of a fireball was introduced by R. Hagedorn in the 60s. He defined it as a statistical equilibrium of an undetermined number of all kinds of fireballs, each of which, in turn, is considered to be a statistical equilibrium of the same kind [6].

[2] This can also be seen by noticing that the expansion of the early Universe was governed by dominant gravitational attraction of the matter within it, while in these fireballs no significant gravitational effects are present that can slow down the fireball expansion. Reference [7] discusses the possible effects of dark matter at the time of the hadronisation of the early Universe.

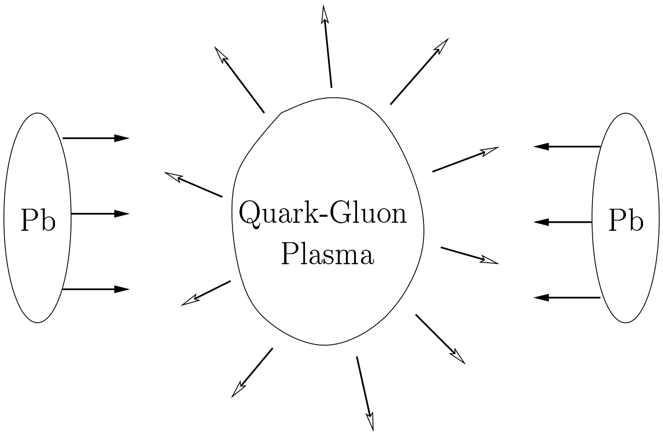

Figure 1.2: Pictorial representation of the creation of a Quark-Gluon Plasma by a Pb-Pb collision in the laboratory, the Pb ions are Lorentz contracted as they are travelling close to the speed of light.

interactions cease. It is *chemical* because it is the stage where the relative abundances of both hadrons and partons are determined. However, elastic scattering may still be present until kinetic freeze out is reached. Particles that hadronise out of a system are known as “soft” ($p_t < 1 - 2$ GeV/c), and those coming from primordial partonic interactions are called “hard” ($p_t > 5 - 6$ GeV/c). Particles are detected at the stage of the collision known as final freeze-out.

Another difference observed in a heavy-ion reaction compared to an elementary particle collision is the production of many more low-energy (soft) particles in the final state, which is due to the conversion of kinetic energy of the collision. In other words, heavy-ion reactions have a high particle multiplicity; how large the particle multiplicity is depends on the centrality of the collision which describes the ‘overlap’ of two incoming ions at the point at which they collide (see figure 1.3). The centrality of an event is generically classified as central (high overlap, then high multiplicity) or peripheral (small overlap, then small multiplicity). Because the centrality is a function of the charged particles produced in a collision, the higher the multiplicity the greater the energy density of the system.

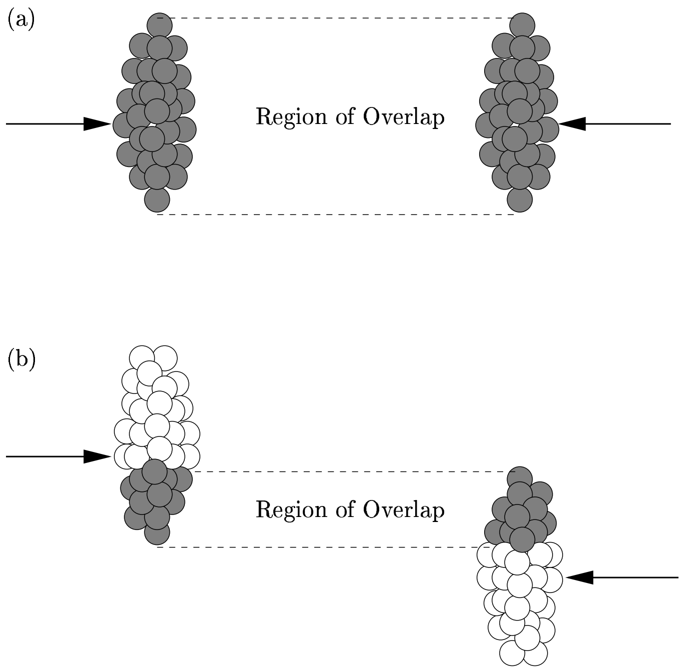

Figure 1.3: Pictorial representation of (a) a central and (b) a peripheral collision. Central collisions have a large number of participant nucleons (shaded) and high multiplicity whereas peripheral collisions have a small number of participant nucleons and low multiplicity. (Courtesy of S.A. Bull [5].)

Various experiments at the CERN SPS and at BNL RHIC energies have shown experimental evidence that a QGP phase has been created under laboratory conditions. In order to assess whether or not a QGP phase has been created, experiments have observed different signatures of its formation as a manifestation of the phase transition. In the following section, an overview of the recent history in the field of ultra-relativistic heavy-ion physics is given, and the most interesting results obtained will be discussed in section 2.3.

1.4 Overview of the recent history in experimental heavy-ion physics

The Super Proton Synchrotron (SPS) at CERN, and the Alternating Gradient Synchrotron (AGS) in Brookhaven National Laboratory were the pioneering experimental facilities in the field of ultra-relativistic heavy ion collisions. Both of them started heavy-ion operation in 1986. The search for a new state of strongly interacting matter at CERN started with beams of oxygen and sulphur, from 1994 continued with lead beams. Measurements of hadronic and leptonic observables from the SPS fixed-target programme are now almost complete thanks to the measurements of the NA49 [8], CERES [9], NA57 [10] and NA60 [11] experiments among others.

Heavy-ion physics has been studied in collider mode since 2000, by the relativistic Heavy Ion Collider (RHIC) [12, 13] experiments (STAR, PHENIX, PHOBOS and BRAHMS) at Brookhaven National Laboratory (BNL). In the near future the challenge passes to the CERN Large Hadron Collider and especially to ALICE (A Large Ion Collider Experiment), which will be the only dedicated LHC experiment for heavy-ion physics, and will measure the highest-energy collisions ($\sqrt{s_{NN}}$=5.5 TeV) of heavy nuclei ever achieved under laboratory conditions; almost 30 times higher than at RHIC. In chapter 3, a more detailed discussion about the LHC and the ALICE detectors is presented. The GSI laboratory is expected to house the Compressed Baryon Matter experiment (CBM) that will be part of the new accelerator facility (FAIR) [14]. CBM will study nucleus-nucleus collisions from 10 to 45 AGeV [3]in order to explore the QCD phase diagram in the region of highest baryon densities and the phase boundary region, its first beams are scheduled for 2014.

The Birmingham Particle Physics group has been involved in the CERN heavy-ion programme since 1987 and, in particular, has played a major part in the data analysis of the WA85, WA94, WA97 and NA57 experiments [3]. In ALICE, the

---

[3] This follows the convention of beam energy or momentum per nucleon in the nucleus.

Birmingham group responsibilities include the design, construction, installation and maintenance of the ALICE Central Trigger Processor (CTP) and Local Trigger Units (LTUs) as well as all the corresponding control and monitoring software. Birmingham is also responsible for the overall trigger coordination within ALICE. In chapter 4, the key features of the ALICE trigger system are presented. In terms of physics, Birmingham is currently interested in resonance production in ALICE, and more recently in heavy flavour and hard physics.

1.5 The physics role of ALICE at the LHC

In this section, a motivation for the developments in the field of ultra-relativistic heavy-ion physics is given. In particular, the significant and unique opportunities that will be exploited in the ALICE experiment at the Large Hadron Collider are described briefly. The physical observables in ALICE will be discussed in section 2.4.

At LHC energies, the fireball with its envisaged high multiplicity is expected to have a relatively much longer lifetime (up to about 10 fm/c) compared to SPS and RHIC energies. By colliding nucleus-nucleus collisions, the LHC will exceed the energy densities available at RHIC energies by over an order of magnitude. ALICE will be able to study the strongly interacting matter at high energy densities in the regime of $\epsilon \sim$ 1-1,000 GeV fm^{-3} [15]. It will study the structure of the QCD phase diagram in detail, and in particular the properties of the QGP phase. The role of chiral symmetry in the generation of mass will also be studied (see section 2.1.3).

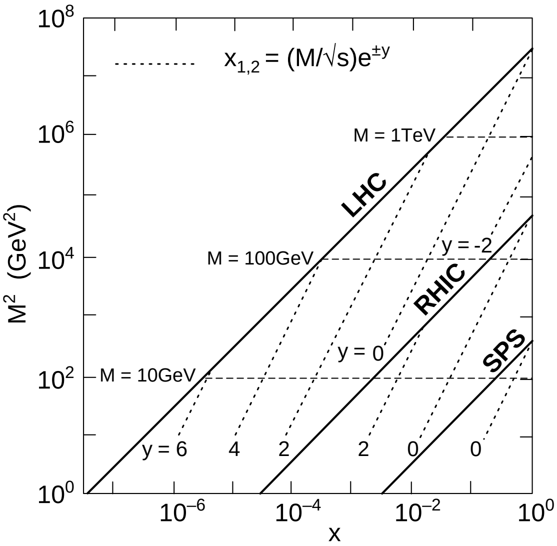

Figure 1.4: The range of Bjorken x and M^2 relevant for particle production in nucleus–nucleus collisions at the top SPS, RHIC, and LHC energies. Lines of constant rapidity are shown for LHC, RHIC and SPS.

The LHC physics programme will cover a novel range of Bjorken-x values as shown in figure 1.4, where the relevant x regions for the SPS, RHIC and LHC with heaviest nuclei are compared. In particular, ALICE will probe the x range as low as about 10^{-5}, this will contribute to a better understanding of high-density parton distributions in the determination of particle production [4]. Hard processes, which can be calculated using perturbative QCD, will be used to study the early stages of the collision; while weakly interacting probes such as direct photons will provide information about nuclear parton distributions at very high Q^2. Another novel aspect is that at the LHC the fireball expansion will be dominated by parton dynamics and the collective features of the hadronic final state, i.e. the ratio of the lifetime of the QGP state relative to the time for thermalisation is expected to be larger than at RHIC by an order of magnitude. Additionally, ALICE will study proton-proton physics at the LHC as a benchmark for the heavy-ion physics, though it is also important in its own right as, for example, ALICE will access considerably increased charged-particle densities that will give a better understanding of strangeness production, such as transverse momentum measurements owing to the unique low-transverse momentum cutoff that will be provided by the ALICE experiment. Studies of proton-nucleus physics will also be possible.

1.6 Outlines for the rest of this thesis

Up to this point, a very general look at the field of ultra-relativistic heavy-ion physics has been given. As mentioned, in Chapter 2 a detailed description of the theoretical framework behind these studies, along with some of the most recent experimental evidence for the discovery of the QGP are given. Chapter 3 provides a description of the ALICE detector apparatus, while chapter 4 introduces the ALICE trigger system. Chapter 5 describes the implementation used to synchronise trigger input signals in the ALICE experiment, this as a preable information needed for chapter 6, which presents the software developed carried out by the author for the LVDS transmission tester. Chapter 7 presents a feasibility study of the di-lepton exclusive process that can potentially be used as a luminosity monitor. Chapter 8 provide us with the motivation to study inclusive ϕ meson production both in heavy ion and pp collisions at the LHC. Finally, chapter 9 presents the prospects of measuring inclusive ϕ meson production at LHC energies, along with results from reconstructed ϕ resonance in pp collisions. Special attention is devoted to the prospects of ϕ production during the early physics programme of ALICE at the LHC startup. At the end of each chapter a general summary is given, while the conclusion sections intend to summarise the main contributions given in this thesis.

Chapter 2

The physics of ultra-relativistic heavy-ion collisions

This chapter contains a survey of the fundamental concepts that support the physics of strongly interacting matter at high energy densities. Firstly, a brief phenomenological introduction to some of the most fundamental principles of Quantum Chromo-Dynamics (QCD) is presented, followed by a description of QCD phase transitions and the Quark Gluon Plasma. Secondly, the main experimental results in the field are discussed. Finally, the physics motivations to study the QGP phase at LHC energies, with particular emphasis on the ALICE experiment, are reviewed.

2.1 Quantum Chromo-Dynamics (QCD)

Quarks and anti-quarks are *elementary* particles because they do not appear to have sub-structure [16]. Many hadrons decay into other particles (or resonances) via the strong interaction, and as far as the strong force is concerned, the total isospin is conserved. Approximate higher symmetries were discovery in the 1960s, which led to the formation of various multiplets (strangeness in the vertical axis, versus the isospin component I_z in the horizontal axis). A pattern observed in the baryon decuplet of states with spin-parity $\frac{3}{2}^+$ led to the prediction of the Ω^-, discovered in 1964 [17]. The acceptance of quarks as fundamental particles (building block of hadronic matter) came a little bit later with the studies of the structure of the nucleon through experiments of elastic and deep inelastic scattering, along with various studies based on e^+e^- annihilation [17].

The theory of strong interactions (QCD) emerged in the 1970s, and nowadays is one of the components that form the SU(3)×SU(2)×U(1) “standard model” (SM) of the field of high energy physics [18]. QCD is one of the quantum field theories (QFT) in the SM, the other being the electro-weak theory. In analogy to the photon in Quantum electrodynamics (QED), the gluon is the mediator of the strong interaction in QCD. In the next sections, three of the most interesting results of QCD will be described as they support most of the physics behind the theoretical tools to study the QGP.

2.1.1 Asymptotic freedom

The interaction between any two quarks can be modelled by:

$$V_s \sim -\frac{\alpha_s}{r} + kr, \tag{2.1}$$

which is known as the strong potential V_s, where α_s is the magnitude of the strong coupling constant between two quarks, k is the string tension and r gives the separation of the quarks. For small values of r, equation 2.1 is equivalent to the Coulomb potential experimented between two electric charges [19].

There are two remarkable features of QCD that are related to the fact that α_s is not a constant but a variable with a scale-dependence due to quantum effects ($\alpha_s \sim 1/\ln(r^{-1})$), which makes the quark's interaction weaker as r decreases. Thus, it can be established that at short distances (or large momentum transfer), the coupling constant is small and would tend to zero at high energies. This is one of the main features of QCD; known as the regime of "asymptotic freedom", which suggests that quarks may behave as free (or noninteracting) particles in the limit $r \to 0$.

Asymptotic freedom turns QCD into a quantitative calculational scheme for physical observables by using perturbation theory. Moreover, it is only in this regime where high-precision tests can be performed such as those developed for QED processes [20]. For example, a QCD cross-section can be described perturbatively as follows:

$$\sigma = C_1\alpha_s + C_2\alpha_s^2 + ..., \tag{2.2}$$

where the coefficients C_1 and C_2 can be calculated from Feynman rules. However, various divergences [18] arise when performing such calculations. In order to cope with these divergences, a renormalisation procedure is required [18]. These methods work by fixing certain parameters at a given energy scale μ. For the sake of comparison, the renormalisation group requires a common scale that is generally taken to be the mass of the Z boson. Other scales can be used from:

$$\log(\frac{\mu^2}{\mu_0^2}) = -\int_{\alpha_s(\mu_0)}^{\alpha_s(\mu)} \frac{d\alpha}{\beta(\alpha)}, \tag{2.3}$$

with μ_0=$\mathrm{M_Z}$. Additionally, or alternatively, the dimensional parameter Λ can be introduced to express the parameterisation of the scale-dependence of the α_s values; its definition is related to the β-functions that control the renormalisation scheme [18, 21]. These functions are composed of a group of equations that can be obtained by perturbatively expanding the solutions of:

$$\mu\frac{\partial\alpha_s}{\partial\mu} = 2\beta(\alpha_s). \tag{2.4}$$

The effective QCD coupling "constant" α_s can be written as a function of the scale μ and in terms of the parameter Λ:

$$\begin{aligned}\alpha_s(\mu) &= \frac{4\pi}{\beta_0\ln(\mu^2/\Lambda^2)}(1 - \frac{2\beta_1}{\beta_0^2}\frac{\ln[\ln(\mu^2/\Lambda^2)]}{\ln(\mu^2/\Lambda^2)} + \frac{4\beta_1^2}{\beta_0^4\ln^2(\mu^2/\Lambda^2)} \\ &\quad \times((\ln[\ln(\mu^2/\Lambda^2)] - \frac{1}{2})^2 + \frac{\beta_2\beta_0}{8\beta_1^2} - \frac{5}{4})] \text{ [20]}. \end{aligned} \tag{2.5}$$

From here it can be seen that $\alpha_s \to 0$ as $\mu \to \infty$, which corresponds to the asymptotic freedom regime. Calculations performed under the perturbative quantum chromodynamics (pQCD) method have been extensively tested [21]. For example, the production of hadronic jets with large transverse momentum in hadron-hadron collisions constitutes a direct probe of the scattering of quarks and gluons [20]. The data from such experiments have been used to determine the values for α_s. Figure 2.1 shows a summary of the values of $\alpha_s(\mu)$ for various high energy processes. However, the main theoretical motivation for this thesis will concentrate on QCD predictions that turn out to be in the non-perturbative domain.

2.1.2 Confinement

In contrast to the values obtained in the regime of asymptotic freedom, it turns out that at large distances (or small momentum transfer), the strong coupling constant α_s is large (at $\mu \sim \Lambda$). It is believed that in this regime the quarks are confined in colourless particles[1]. Confinement, as it is known, is expected to increase as the distance between two quarks becomes larger. This QCD phenomenon is responsible for the fact that hadrons have yet only been observed either as quark-antiquark pairs (known as mesons) or bound together in groups of three (known as baryons). However, QCD does not exclude the existence of other types of hadrons; such as

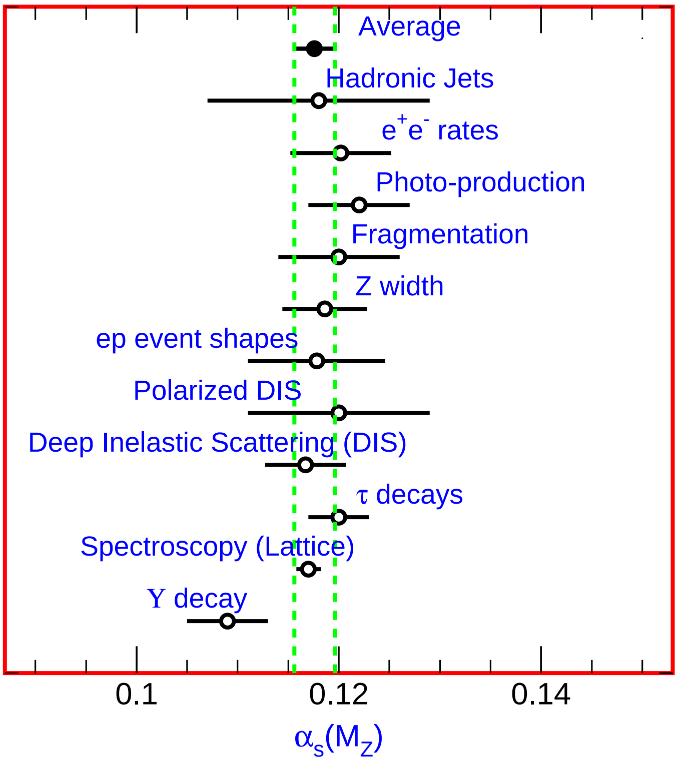

Figure 2.1: Compilation of the values of $\alpha_s(\mu)$ for various processes [20]. The measured value of α_s extrapolated to $\mu{=}M_z$ is shown for the different processes. The total error with the corresponding theoretical uncertainties is included.

pentaquarks (five-quark systems). From a theoretical point of view, the study of confinement is not a negligible task as hadron spectra (i.e. masses and particle widths) are governed by non-perturbative aspects of the strong interaction. At present, their description is based mainly on numerical methods inspired by QCD models [18].

2.1.3 Chiral symmetry breaking

Chiral Symmetry (CS) breaking [22, 23], which is purely related to QCD dynamics, provides with an explanation on the generation of mass of the lighter quarks (u, d and s).

For spin-$\frac{1}{2}$ particles, such as quarks, there are two helicity eigenstates that can be defined. It was found that in the absence of quark masses, when quarks travel at the speed of light, the left- and right-handed states of the QCD Lagrangian are chirally symmetric. In other words, both states of quarks can be seen to be independent from each other; their helicity is invariant. This can be achieved by neglecting the masses of the three lightest quarks which then will form the flavour symmetry group $\mathrm{SU(3)_L \times SU(3)_R}$.

In order to describe this QCD symmetry, let us remember that the vacuum in physics can be represented in term of quantum states composed of several condensates. Because the force between quarks is very strong, the ground state (or vacuum) in QCD is not stable compared to the constituent condensates.

Let us now consider a pair of charged particles in a singlet state, such that these pairs can pop-up from the vacuum due to quantum fluctuations. The separation in space (or r) is given by the uncertainty relation ($\mathrm{p} \cdot \mathrm{r} \geq 1$), where p is the relative momentum acquired by these two particles. By neglecting their masses, the minimal

---

[1] It is not possible to derive confinement from the QCD Lagrangian; the same applies to asymptotic freedom.

kinetic energy of the pair is equal to the relative momentum if they are separated by a distance r, i.e. $\mathrm{E_{kin}} \geq 1/r$. On the other hand the potential energy is $\mathrm{E_{pot}} = -\frac{q^2}{4\pi r}$, where q is the charge of the particles. Therefore, the total energy is [3, 24, 25]:

$$E_{\text{pair}} = \frac{1}{r} \cdot (1 - \frac{q^2}{4\pi}). \tag{2.6}$$

In QED the charge q is equal to the electric charge e, while in QCD the charge is the colour charge $\mathrm{g_s}$. In QED, equation 2.6 is valid for all distances r (above the Planck scale), but in QCD this expression is only valid for small distances of r.

Let us look at what will happen when charged pairs pop-up from the vacuum. In QED, the e^+e^- pairs that pop-up from the vacuum will be unstable because their energy is positive for all distances r (see figure 2.2); i.e. as the electromagnetic field is “weak”, the kinetic energy of these pairs will always overcome the energy stored in the field. In the case of QCD, the term 1 - $q^2/4\pi$ decreases with distance, and at $r \sim 1$ fm becomes negative. Such a configuration means that the colour pair that has popped-up from the vacuum will give rise to “real” particles, i.e. as the QCD field is “strong”, the energy stored in the field will overcome at some distance the kinetic energy of the pair.

At large distances the energy of the colour pair rises linearly and becomes positive again (see figure 2.2). Therefore, in QCD the total energy can be either positive or negative depending on the values of r. Moreover, the total energy $\mathrm{E_{pair}}$ has a minimum at r_0, about 1 fm, which is a negative value. Then the total energy of the pair is negative, and the QCD vacuum is spontaneously filled by gluon pairs and $q\bar{q}$ real particles [26].

In conclusion, at r_0 the QCD vacuum is spontaneously filled by colour charged pairs. This means that quarks propagating in such a vacuum do so as if they had a mass by spontaneously changing their helicity and therefore giving rise to the constituent mass; about 300 MeV for up and down quarks and 450 MeV for the strange quark. If Chiral Symmetry breaks spontaneously, the dynamically-

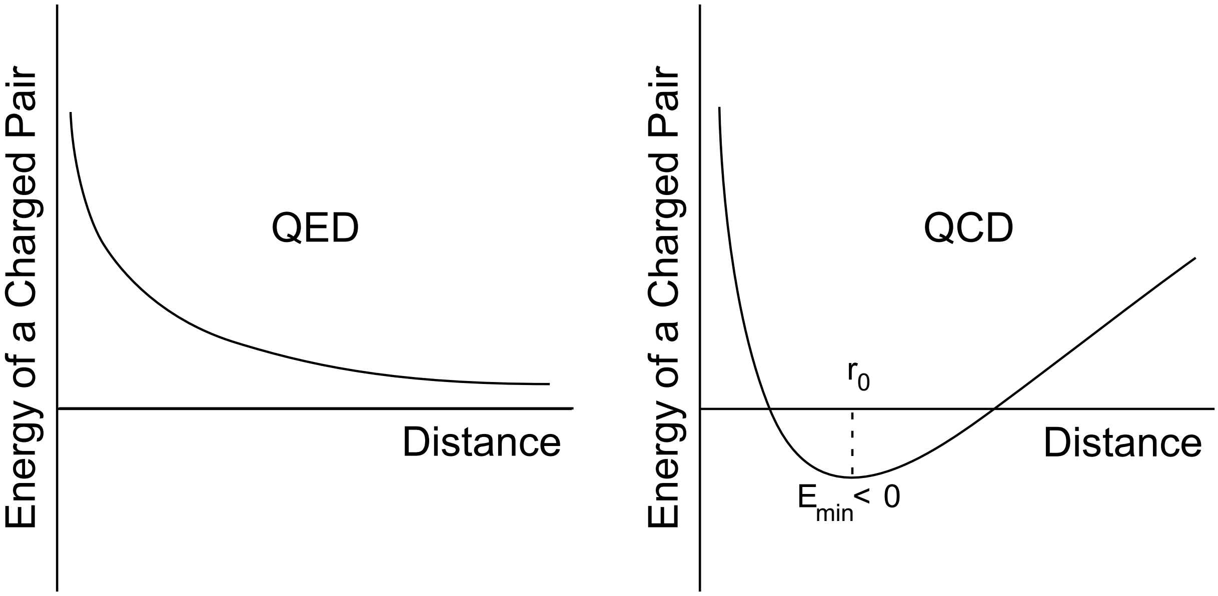

Figure 2.2: Qualitative energy dependence of the energy of a charge single pair (that has popped-up from the vacuum) as a function of the distance between the charges in the case of QED (left) and QCD (right).

generated mass may be much greater than the quark's intrinsic mass. Table 2.1 shows a summary of the quark masses.

Nonetheless, it is thought that the kinetic energy of the vacuum of colour pairs can be increased by *raising the temperature of the system* in such a way that the potential energy will no longer be able to overcome the kinetic term for any distance r [27]. Thus, it is believed that the chiral symmetry breaking can be restored, which would result in the quarks having their "bare" masses again [28, 29].

Notice that such a restoration can only be partial as the QCD Lagrangian is always explicitly broken [28] because of its finite mass term $-m_q\bar{q}q$. An understanding of the partial chiral symmetry restoration is expected to shed light on the origin of most of the hadronic mass in the Universe.

Table 2.1: Summary of the quark masses [19].

Quark flavour	Constituent mass (MeV/c^2)	Current mass (MeV/c^2)
down (d)	~ 350	~ 7
up (u)	~ 350	~ 3
strange (s)	~ 550	~ 140
charm (c)	~ 1800	~ 1800
bottom (b)	$\sim 4.2\times10^3$	$\sim 4.2\times10^3$
top (t)	$\sim 170\times10^3$	$\sim 170\times10^3$

2.2 Theoretical tools to study the QGP

2.2.1 Introduction

In the last section, asymptotic freedom, confinement, and chiral symmetry breaking were described. It was seen that changes on the temperature of the QCD vacuum have a very significant effect on its properties; in particular on the origin of most of the mass of the lighter quarks (u, d and s). In addition to these three interesting QCD predictions, there is another one that leads us to the discussion of most of the reminder of this thesis: the Quark Gluon Plasma (QGP).

As described in chapter 1, normal hadronic matter under extreme conditions of high energy densities or temperatures undergoes a phase transition into an asymptotically free gas (or liquid) of quarks and gluons; in other words, hadronic matter no longer exists in the familiar forms of mesons and baryons as described in the field of particles physics. As mentioned earlier, quarks and gluons are confined inside hadrons. However, in a very hot quark matter state, the average distance between particles will become smaller so that confinement disappears.

The complexity of the system created in heavy-ion collisions naturally lends itself to the methods of relativsitc statistical models. Predictions from the Bag Model method will be discussed in section 2.2.2. The theoretical evidence for a QGP phase is now even more striking as recent calculations of lattice QCD also predict a phase transition at similar values of temperature and energy density as the one given by statistical models.

The paradigm of QGP originates in the 1970s [30]. Its description within the framework of asymptotically free QCD was first discussed in 1974, shortly after the discovery of asymptotic freedom [31]. It was suggested that hadronic matter at very high densities such as those that occur in the core of neutron stars could be a "quark soup" rather than a system of quarks bounded in hadrons. In other words, at conditions of extreme energy densities a quark matter state ought to exist. Today's view of the formation of such a state due to a phase transition came some years later by making an analogy to a "boiling hadron gas state" [32, 33].

Different methods have been developed to make an estimation of the transition temperature of QCD matter into a QGP state. At present, both statistical and lattice QCD calculations predict that at about 170 MeV, corresponding to an energy density of $\epsilon_c \simeq 1\text{GeVfm}^{-3}$, hadronic matter undergoes such a phase transition to a deconfined state of quarks and gluons.

2.2.2 Statistical models: the bag model

The bag model [34, 35, 36] is a good example of a statistical model as it predicts the aforementioned phase transition, by attempting to describe both the asymptotic freedom and confinement. In this model, the hadrons are represented as "bags" inside a confined medium, and inside these bags quarks are treated as free particles. In order to take this into account, an energy density constant known as the bag constant (B), is introduced.

One can obtain the total energy of a hadron (at rest) in terms of the kinetic energy of the quarks inside the bag, and the potential energy of the volume of the bag. This will leads to thermodynamic quantities such as the energy density and pressure calculated as a function of temperature.

Let us consider two approximations that will provide an example to estimate the transition temperature at zero baryon density. Firstly, consider a "hadronic gas" composed of non-interacting massless pions, where the pressure is given by:

$$\mathrm{P}_{\mathrm{massless-pions}} = 3 \cdot \frac{\pi^2}{90} T^4. \tag{2.7}$$

Here the factor three comes from the three boson degrees of freedom, i.e. the three isospin pion state with no fermionic particles. In fact, this factor comes from the degeneracy factor which is different for boson ($\mathrm{n_b}$) and fermion ($\mathrm{n_f}$) degrees of freedom:

$$\mathrm{g} = \mathrm{n_b} + (1 - \frac{1}{2^3})\mathrm{n_f} \ [26]. \tag{2.8}$$

Secondly, for an ideal "QGP" gas composed of massless gluons and of two-flavour quarks, the pressure is:

$$\mathrm{P_{QGP-phase}} = 37 \cdot \frac{\pi^2}{90} T^4 - B, \tag{2.9}$$

where 37 counts for the degrees of freedom of the system in a QGP phase following equation 2.8. Notice that there are 8 × 2 degrees of freedom from the gluons (from their 8 colour states times two spin states), and the quark fermion degrees of freedom (2 flavours times 3 colours, times 2 spins, and times 2 for the quark-antiquark).

In addition, notice that the term B in equation 2.9 is a quantity brought from the Bag model that accounts for the chiral symmetry of the model (see section 2.1.3) [34, 35, 36]. The -B contribution on $\mathrm{P_{QGP-phase}}$ is due to the vacuum, it acts on the surface of the volume in order to reduce the size of the deconfined region [2]. This (negative) pressure term compensates the contribution due to the kinetic energy of the quarks in a way that in equilibrium the pressure vanishes.

Moreover, as a consequence of the Gibb criterion [26], the phase with the largest pressure is the stable one, and at the phase-transition both pressures are equal since the magnitude of the forces exerted by the two phases on each other at their surface of contact must be equal [37], i.e.

$$\mathrm{P_{QGP-phase}(T_c)} = \mathrm{P_{massless-pions}(T_c)} \tag{2.10}$$

where $\mathrm{T_c}$ is the critical temperature, given by:

$$\begin{aligned} T_c &= \left(\frac{45}{17\pi^2} B\right)^{1/4} \\ &\approx 0.72 B^{1/4}. \end{aligned} \tag{2.11}$$

Hence, in this case the transition is of first order, and taking $B^{1/4} \approx 200$ MeV [26], a critical temperature $T_c \approx 150$ MeV is predicted for the phase-transition. Similar results of this temperature can be obtained from lattice QCD calculations.

2.2.3 Lattice QCD results

Lattice gauge techniques have been developed to provide a first-principles approach to formulate and study QCD physics in a discrete manner, rather than in a continuous space-time way [38]. In other words, the functional integral of QFT is expressed in a finite dimensional way, that can be calculated making use of Monte Carlo techniques [39]. From this method, numerical simulations can be performed using four dimensional space-time lattices defined by their size and lattice spacing. Lattice QCD has described some properties of the strongly interacting matter under extreme conditions of temperature and density [40, 41].

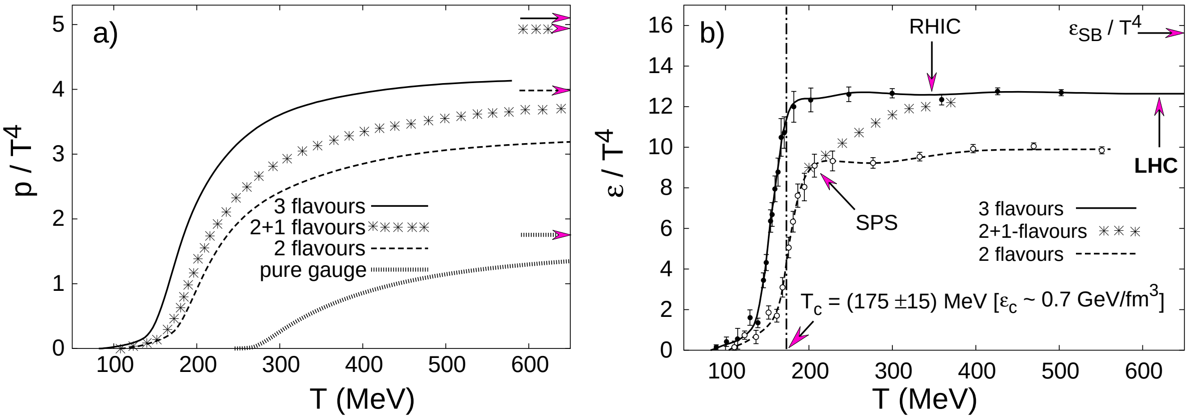

Figure 2.3: The pressure (a) and energy density (b), in lattice QCD with 0, 2 and 3 degenerate quark flavours along with two light quarks and a heavier (strange) quark. The arrows on the right-side horizontal axis show the limit for an ideal quark-gluon gas [41, 42]

The results of a recent lattice QCD calculation of pressure (p) and energy density (ε) of the system in the vicinity of the critical temperature (T_c) are shown in figure 2.3, for 2- and 3-flavour QCD with light quarks and for 2 light plus 1 heavier (strange) quark [41, 42]. The rapid increase in the number of degrees of freedom of the system can be seen as an indication that a transition from hadrons to the "quark soup" is foreseen. Lattice calculations suggest that the cross-over in energy density is rather rapid (see figure 2.3 (b)), taking place in a narrow temperature interval about $T_c \sim 170$ MeV [43]. However, the quite smooth rise of the QCD pressure with temperature (see figure 2.3 (a)) can be understood as an indication that it is not a strong first-order phase transition [44].

2.3 Physical observables of a QGP phase

As mentioned before, in order to assess whether or not deconfined matter has been created, suitable signatures must be sought. In the following subsections, QGP signatures related to strangeness particle production, charmonium suppression, jet quenching and elliptic flow are briefly examined, along with some of the most recent experimental results at SPS and RHIC energies.

2.3.1 Strangeness enhancement

Strangeness enhancement was one of the main pieces of evidence for CERN's claim to have produced deconfined matter [3, 45]. Essentially, if a QGP phase was formed in nucleus-nucleus collisions, the yields of strange particles produced, such as those that contain one or more strange quark or antiquark, are expected to increase compared to a non-QGP scenario. In other words, the density of strange quark pairs is predicted to be unusually high compared to that for a hadron gas phase [30].

The mechanism for strange quark-pair production can be described by thermal reactions in the plasma such as gluon fusion (gg$\rightarrow s\bar{s}$), which turns out to be the dominant process of $s\bar{s}$ pair production, as shown in figure 2.4. In the same figure (panel (b)), the Feynman diagrams for such reactions are illustrated.

One of the features of this signature is that if deconfinement occurs, the reactions that lead to strangeness production have to be partonic. At the partonic level, strange particles have lower thresholds and higher cross-sections. This is particularly so if the strange quark mass reduces owing to the associated partial restoration of chiral symmetry (see section 2.1.3). The bare mass of strange quark is about 150 MeV and with a plasma temperature of about 200 MeV it becomes energetically easy to produce large numbers of strange quark-antiquark pairs [3].

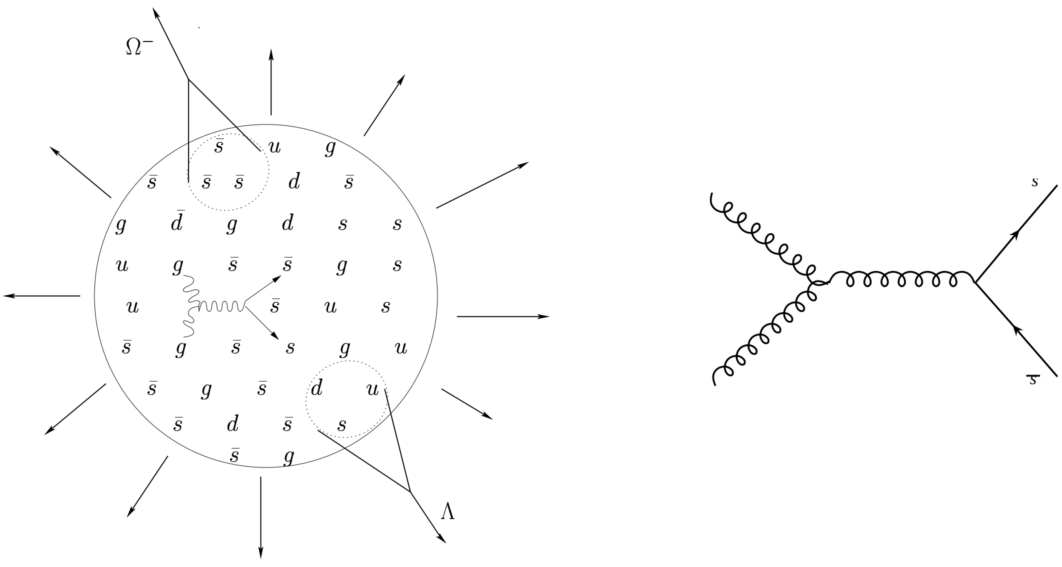

(a) (b)

Figure 2.4: Panel (a): Mechanism of strange hadron formation from the QGP: inserts show gluon fusion strangeness, followed by QGP recombinant hadronisation Panel (b): Feynman diagrams for thermal gluon fusion [30].

Multi-strange hadrons (i.e. hadrons with more than one strange quark) and their anti-particles will be particularly enhanced. Their single-step production in a hadron gas has a higher energy threshold. Strange antiparticles can only be produced after a sequence of many reactions (e.g. $\pi\bar{\Lambda} \rightarrow \mathrm{K}\bar{\Xi}$, $\pi\bar{\Xi} \rightarrow K\bar{\Omega}$). They are particularly difficult to produce in a baryon-rich environment (such as those observed at WA97 and NA57) since baryon number conservation indicates they can only be created with an accompanying baryon. For example, in the reaction $\pi\mathrm{p}\rightarrow \pi\bar{\mathrm{p}}\mathrm{pp}$ with the antiproton, the momentum threshold is 1.32 GeV/c. The parton level then has far lower thresholds. Table 2.2 shows the momentum threshold for different particle reactions. However at central rapidities at the LHC there should be equal numbers of baryons and antibaryons, since the valence numbers cannot shift enough in rapidity (see below).

As figure 2.5 shows, a clear experimental enhancement has indeed been observed by the WA97 and NA57 collaborations [46, 47]. The results are normalised to the pBe yields, and the corresponding enhancements calculated for pPb and different

Table 2.2: Momentum threshold for different particle reactions.

Reaction	Momentum threshold
$\pi\mathrm{p}\rightarrow\pi\bar{\mathrm{p}}\mathrm{pp}$	1.324
$\pi\bar{\mathrm{p}}\rightarrow\mathrm{K}\bar{\Lambda}$	0.517
$\pi\bar{\Lambda}\rightarrow\mathrm{K}\bar{\Xi}$	0.547
$\pi\bar{\Xi}\rightarrow\mathrm{K}\bar{\Omega}$	0.674
$\mathrm{gg}\rightarrow\mathrm{s}\bar{\mathrm{s}}$	0.150

centrality classes for Pb-Pb, separated as a function of the number of "wounded nucleons", i.e. the number of nucleons taking part in primary collisions. Enhancements are seen in Pb-Pb. These increase with centrality and reach a value of about 20 for Ωs in the most central collisions. Similar results from RHIC have recently been reported [48, 49]. Although strangeness production has been historically a relevant QGP signature, the role it would play at the LHC may be different from that at SPS energies. This is mainly because the lifetime of the fireball is much higher, which means that even in a hadron gas this enhancement effect might be seen. A discussion about strangeness enhancement at LHC can be found in [50, 51].

2.3.2 Particle production

In addition, most recently, an equilibrium statistical model has been applied to Au-Au collisions at RHIC energies [52]. Figure 2.6 shows that for most of the particles the experimental results are well described by the model within the experimental uncertainties. From the first ratios of the full-line fit presented in this figure, a chemical freeze-out at T=160.5±2 MeV and μ_β=20±4 MeV was obtained. However, when the ratios of $\bar{p}/\pi^-$ and ϕ/K^- from PHENIX data are included in this fit, the temperature decreases to T=155±2 MeV (with μ_β=26±5 MeV). Notice that this change comes from the $\bar{p}/\pi^-$ points as the predictions for ϕ/K^- are practically the

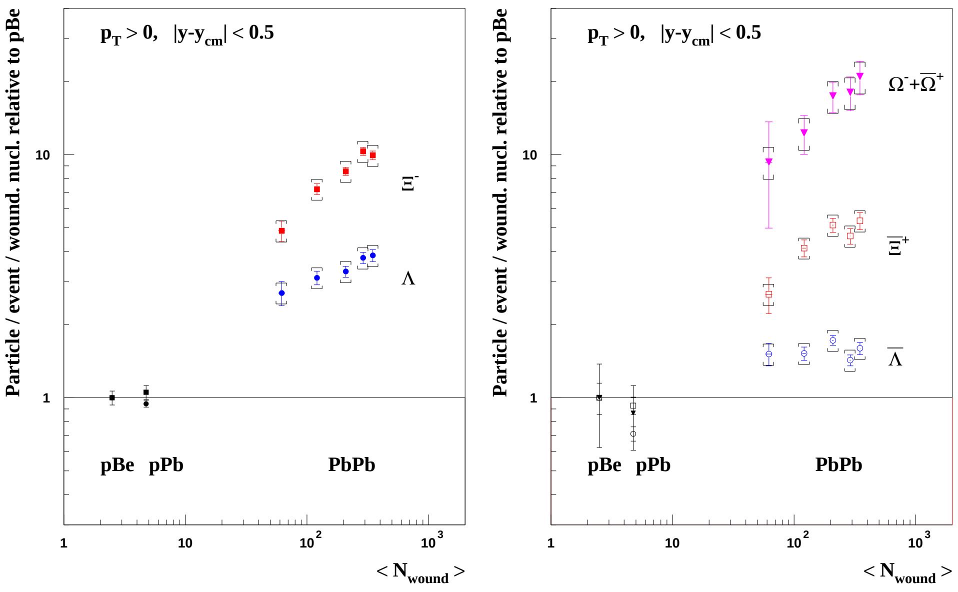

Figure 2.5: Enhancement factors measured by the NA57 collaboration in pPb and Pb-Pb interactions relative to pBe interactions. The data correspond to collisions at 158 *A*GeV/c [46, 47]. The particles in the left-hand panel have quarks in common with the initial state, while those in the right-hand panel do not.

same for the two temperatures (see [53, 54, 55]). These results are an indication that the baryo-chemical potential μ_B decreased from SPS to RHIC energies as might be expected because at high energy, less constituent quarks are deposited in the central region. Hence, the high density medium that would be created at the LHC is expected to have a low net-baryon density (see figure 1.1). The expected value within the thermal model of hadron yields in central Pb-Pb collisions at the LHC are T=161±4 MeV and $\mu_\beta=0.8^{+1.2}_{-0.6}$ MeV for the temperature and baryochemical potential respectively [56].

2.3.3 Charmonium suppression

It was predicted that the yields of the J/Ψ meson should be suppressed if a QGP state was formed at SPS energies [57, 58]. Because the mass of the charm quark is ten times greater than that of the strange quark, at SPS energies charm (and bottom)

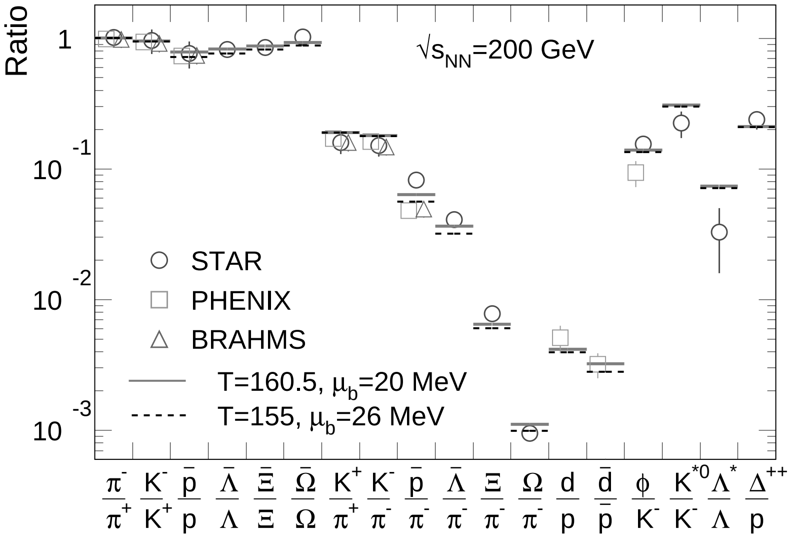

Figure 2.6: Two thermal model fits for different particles at $\sqrt{s}$=200 GeV. The first fit excludes the ratios of $\bar{p}/\pi^-$ and ϕ/K^- obtained at PHENIX [52].

quarks can be seen as particles exclusively produced during the early stages of the collision through high energy hard interactions.

The high abundances of quark-antiquark pairs and gluons produced in the deconfined state would screen the heavy quarks by the surrounding $q\bar{q}$ pairs, which leads to a suppression of their production yields. Thus, the strong potential given in equation 2.1 can be replaced by:

$$V_{QGP} \approx -\frac{\alpha_s}{r} e^{-r/\lambda_D}; \tag{2.12}$$

λ_D is the QCD analogue of the Debye screening length, and is inversely proportional to the temperature of the system; and r is the radius of the meson. Suppression takes place when λ_D <<r. The disassociated quarks can easily produce open charm particles. Similar models can be extended to the ψ' and χ_c charmonium states and even to the Υ particle that is composed of bottom quark-antiquark pairs.

J/Ψ suppression was found at SPS energies by the NA38/NA50 collaboration [59] with good agreement with the theoretical predictions. PHENIX has recently presented similar results [60].

2.3.4 Jet quenching

The RHIC experiments have confirmed that information about the QGP can be revealed by studying the regime of high transverse momentum particles [61, 62, 63, 64]. Jets of hadrons are formed from the initial hard scattered partons, which are thought to be modified when they are produced in the QGP phase [65]. The highest p_t particle can be chosen to define the jet direction (i.e. the leading particle). One then plots the azimuthal angle ϕ in the pseudo-rapidity range coverage given by the detector design. Normally, such plots show two back to back peaks (at 0° and 180°) corresponding to jet particles with large p_t (trigger particle side) and an associated reacting jet ("away-side jet"). However, RHIC has found that this structure is only observed in pp and p-Au data [61]. Figure 2.7 shows that in central Au-Au collisions there is no away-side jet, suggesting that high p_t particles have been absorbed by the medium. Because the jet energies are reduced, this observation is generically referred as a *jet quenching* effect. ALICE will allow, for the first time in heavy ion physics, to reconstruct jets fully.

2.3.5 High p_t particle suppression

It is thought that during the early stages of a heavy-ion collision, high momentum partons ($Q^2 \sim p_t^2$) can produce a parton shower by radiating other partons, which may change their direction relative to that of the initial parton. RHIC has found strong evidence that particle production yields at high transverse momentum are suppressed in the most central heavy ion collisions [61]. This effect can be seen by comparing the normalised transverse momentum spectrum of the AA collisions to the one given by a (pA or pp) collision system where the high energy density medium is not expected to occur. This effect can be parameterised in terms of a nuclear modification factor. STAR has defined this ratio as:

$$R_{AA} = \frac{d^2N^{AA}/dp_T d\eta}{T_{AA} d^2\sigma^{NN}/dp_T d\eta}, \tag{2.13}$$

where $T_{AA} = < N_{bin} > /\sigma_{inel}^{NN}$ scales the distribution by the number of binary nucleon-nucleon collisions. This number is taken into account in R_{AA} because hard particles are produced on short time scales ($\sim 1/p_t$). Thus, in the absence of nuclear effects, the nuclear modification factor is expected to scale with the number of binary collisions for hard processes, making R_{AA} equal to one. Despite this, R_{AA} values below one were reported for different high p_t hadrons [66]. For example, figure 2.8 shows the predictions, based on perturbative QCD calculations of the R_{AA} ratio in order to study heavy quark energy loss through electrons from semileptonic decays of D and B mesons in central Au-Au collisions along with the STAR data. Most of the calculations predict lower values for R_{AA} than those observed. However, the transverse momentum distribution is well reproduced and a clear suppression effect can be seen for all predictions. In addition, this confirms that heavy quarks may provide, in future, additional constraints to the energy loss mechanics presented at the partonic level [67].

2.3.6 Elliptic flow (v_2)

In the early stages of the collision, gradients of pressure can be produced leading to the expansion of the system [69]. It was found that for non-central heavy-ion collisions, an overlapping area was observed in the reaction region (see figure 2.9). It turns out that such overlapping areas have an elliptic shape; the re-scattering processes among particles are thought to be responsible for transferring this spatial deformation onto the observed anisotropic transverse momentum distribution of the measured hadrons. Elliptic flow is denoted as v_2; it is defined to be the second Fourier coefficient of the azimuthal distribution expansion of anisotropic flow. The

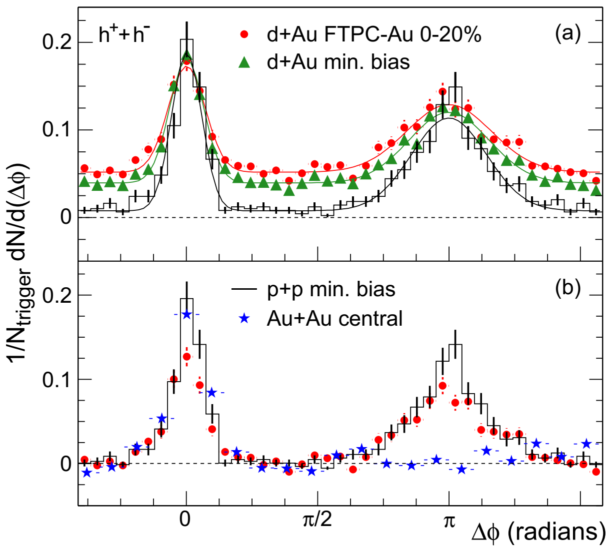

Figure 2.7: STAR experimental results about the angular correlations observed between pairs of high-p_t charged particles, referred to a selected (trigger) particle, for (a) p-p (solid line) and d-Au central (dots) and minimum bias (triangles) interactions and (b) central Au-Au (stars) collisions. The away-side jet is not observed for central Au-Au collisions. Both results were obtained from collisions at $\sqrt{s}_{NN}$=200 GeV [61].

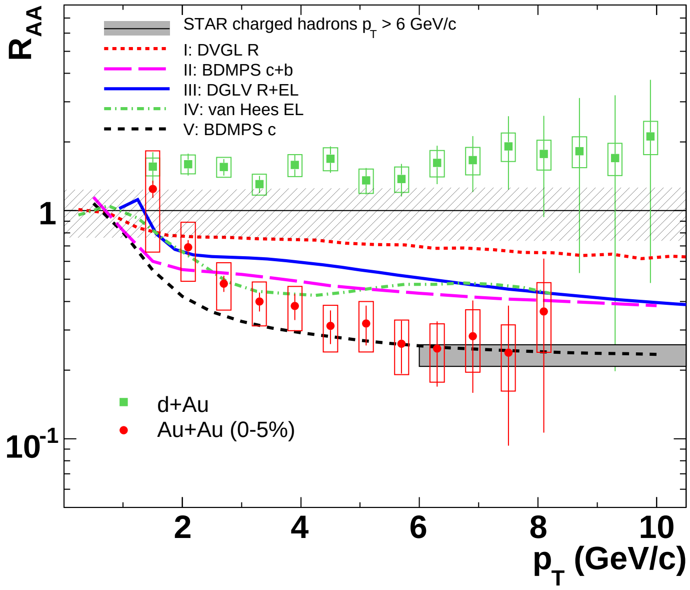

Figure 2.8: Nuclear modification factor R_{AA} for d-Au (deuterium-gold) and Au-Au collisions at $\sqrt{s_{NN}}$=200GeV. STAR data is compared with recent pQCD calculations [68].

first coefficient is known as directed flow. The harmonic numbers can be defined as:

$$\frac{dN}{d\varphi} = \frac{v_0}{2\pi} + \frac{v_2}{\pi}\cos 2\varphi + \frac{v_4}{\pi}\cos 4\varphi + ... \tag{2.14}$$

The odd coefficients (sine terms) do not contribute to the "anisotropic terms" as reflection symmetry with respect to the reaction plane makes them go to zero. Thus, the elliptic flow coefficient can be calculated as:

$$v_2 = \langle \cos(2(\phi - \Psi_R)\rangle \tag{2.15}$$

where ϕ - Ψ_R is the azimuthal angle around the beam measured relative to the impact parameter (see figure 2.10); the brackets indicate an average over the single particle distribution (dN/dp_tdϕ). The study of "elliptic flow" has been developed considerably at RHIC energies [70]. Flow can be described using various models based on relativistic hydrodynamics. They attempt to study the evolution of the system assuming a continuous flow of particles from the produced high energy collisions. This is so at high energy densities where the mean free path of the particles is much smaller that the size of the system. The elliptic flow of various particles has been measured at RHIC. Calculations based on hydrodynamical model have been compared to the data. Two different behaviours are observed for the low and high transverse momentum region. For particles with $p_t < 2$ GeV/c, the elliptic flow can be modelled by hydrodynamics [71], whereas for high p_t particles, a significant deviation was observed relative to such calculations. In addition, it was found that there is a mass dependence that was unexpected at high transverse momentum before the RHIC results. What this suggests is that hydrodynamic calculations cannot provide a complete description of this phenomenon [72].

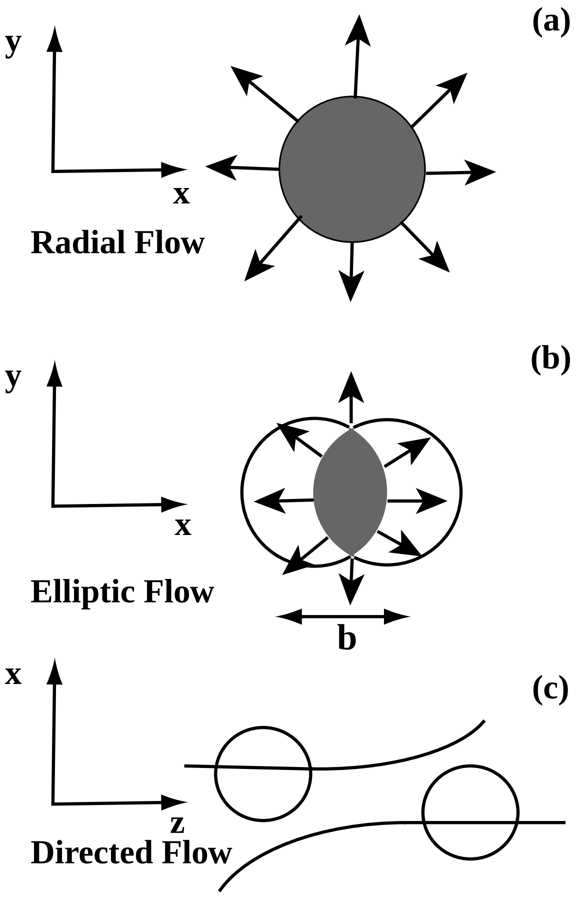

Figure 2.9: Illustration of the three most common flow phenomena.

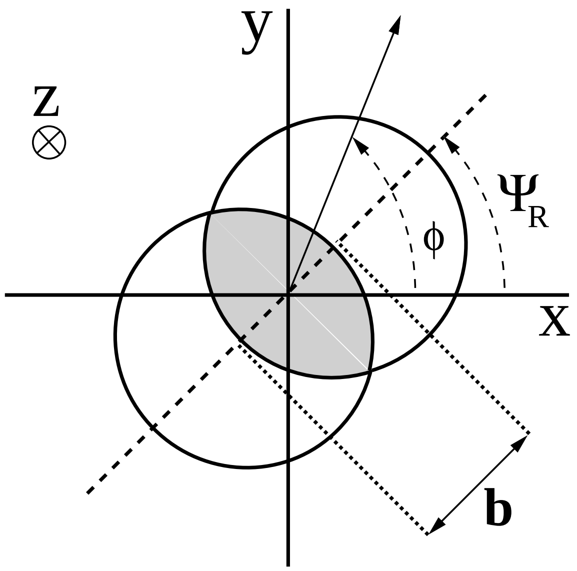

Figure 2.10: Definition of the coordinate system.

2.4 Physics at the ALICE experiment

In chapter 1, a general introduction to the physics role of ALICE in the LHC physics programme was given. In this section the main physical observables that will be addressed by ALICE are briefly mentioned. ALICE will allow the measurement of particle ratios and momentum spectra in the low-, intermediate and high region of transverse momentum. Stable charged hadrons (pions, kaons, and protons) will be identified and measured from the very low momentum (hundreds of MeV) up to at least 50 GeV; charged and neutral kaons, and hyperons up to, and beyond 10 GeV. Resonance production will also be studied (see chapter 8 and chapter 9).

For the first time in heavy-ion physics, the LHC will produce heavy quarks abundantly. Both in pp and nucleus-nucleus collisions, heavy-flavour production can be studied down to almost zero transverse momentum that will allow a sensitive comparison with QCD predictions. Beauty production in central Pb-Pb collisions can be measured via semi-leptonic decays. The complete spectrum of heavy quarkonia states can be accessed. Additionally, direct prompt photons at high values of transverse momentum will allow the studies of the dense medium without any final interaction; while in the low transverse momentum region, thermal photons can reveal the early phases of the fireball [4].

ALICE will allow the study of event-by-event physics, where fluctuations of thermodynamic quantities are studied in order to shed light on the QGP phase transition. The study of flow will be possible, and momentum correlation studies of the two-particle intensity interferometry. The study of jets will be possible; in Pb-Pb collisions the LHC jet rates are 2.6×10^6 per year for $\mathrm{E_t} > 100$ GeV in the ALICE acceptance. This allows us to distinguish jets from the background in the underlying events, permitting us not only to analyse jets from leading particles, but for the first time in heavy-ion physics to reconstruct jets fully. A more detailed description of the ALICE physics programme can be found in [4, 15].

2.5 Summary

In this chapter, a general introduction to the field of heavy ion physics was presented. In particular, the phase diagram of QCD matter and its phase transitions were described. The conclusions obtained from statistical models and recent lattice QCD were discussed. The main experimental facilities in the field were mentioned, and its main experimental results were described in terms of the experimental signatures for a QGP phase. In the following chapter a description of the ALICE detectors and their performance studies will be presented.

Chapter 3

The ALICE experiment at the Large Hadron Collider

Particle accelerators have led to the discovery of new particles, the measurement of their properties and the understanding of the forces that act upon them. Due to switch on in 2008, the Large Hadron Collider (LHC) at CERN (the European Centre for Particle Physics, in Geneva, Switzerland) will collide proton beams at a centre of mass energy of $\sqrt{s} = 14$ TeV and lead beams at $\sqrt{s_{NN}} = 5.5$ TeV. The LHC experiments are presently at the commissioning stage and a detailed physics programme has been prepared for the first physics run. In this chapter a brief overview of the LHC is presented both for the proton-proton and heavy-ion operational mode. The key design features of the main ALICE sub-detectors are also described.

3.1 The Large Hadron Collider (LHC)

A schematic diagram of the LHC machine is shown in figure 3.1. The LHC accelerator complex will take advantage of the tunnel and some pre-existing particle accelerator facilities that formerly housed the Large Electron Positron collider (LEP). The significant increase in energy from LEP to the LHC has been an important challenge. The synchrotron radiation effect in circular accelerators is not negligible; particles radiate as they are bent around the ring. The energy loss per revolution is inversely proportional to the radius of the machine and proportional to γ^4 (relativistic factor). Protons are 2,000 times heavier than the electron which leads to a significant reduction in synchrotron radiation losses. Thus, by using protons rather than electrons and positrons, and with the use of stronger magnets, the LHC can achieve its goal as the newest and highest energy hadron collider.

The machine is installed in a 27 km circular tunnel where two counter-rotating proton beams, each with an energy of 7 TeV, will be transported. At four different intersection points, associated to the experiments, both beams will collide. The first accelerator system in the chain is the Linac2 that will accelerate protons to 50 MeV. The last injection point is located at the Super Proton Synchrotron (SPS) situated near the LHC point 1. In order to accelerate the proton beams from the 450 GeV SPS injection energy to 7 TeV, the LHC uses 8.3 T superconducting dipole magnets. The proton beams come bunched together so that the interactions take place at 24.95 nanoseconds intervals which corresponds to a 40.08 MHz bunch crossing frequency. Some machine parameters of the LHC are shown in table 3.1.

Currently, there are six experiments involved in the LHC project:

- A Large Ion Collider Experiment (ALICE); [4]
- A Toroidal LHC ApparatuS (ATLAS); [74]
- Compact Muon Solenoid (CMS); [75]

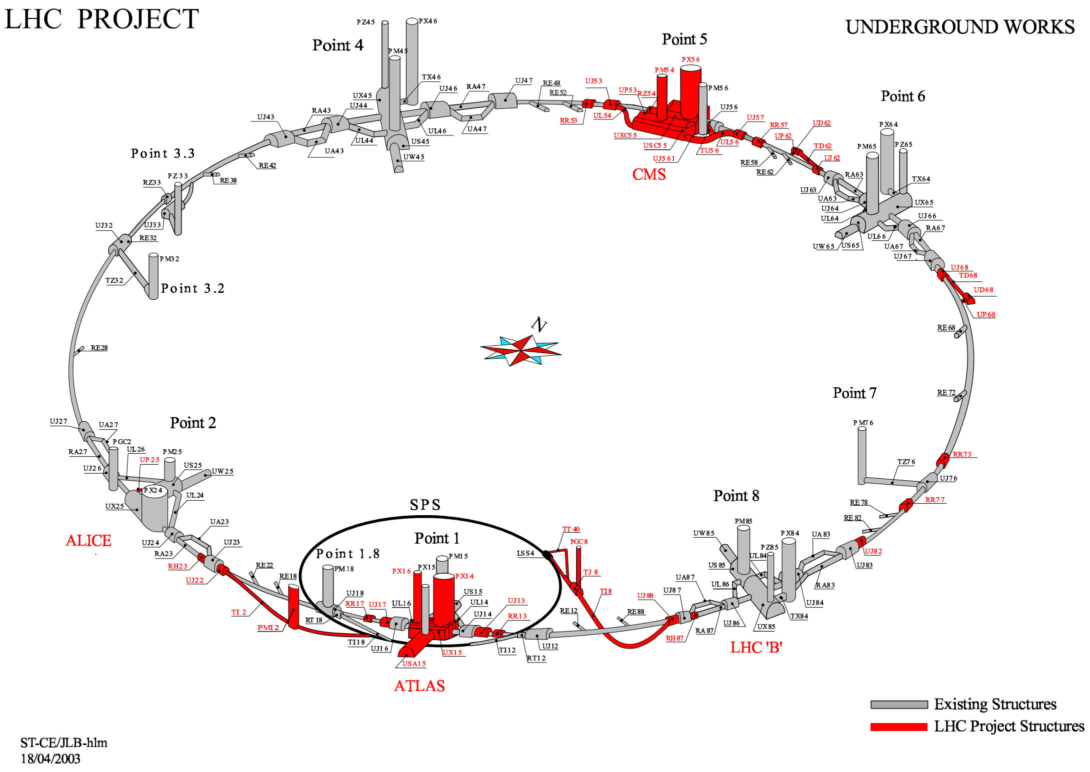

Figure 3.1: The CERN Large Hadron Collider schematic layout.

Table 3.1: Some of the LHC beam parameters [73].

Beam energy	7.0 TeV
Time between collisions	24.95 ns
Initial luminosity (Low)	2 x 10^{33} cm^{-2} s^{-1}
Nominal luminosity (High)	10^{34} cm^{-2} s^{-1}
Particles per bunch	10^{11}
Bunch length (σ_z)	7.5 cm
Bunch width (σ_x)	15.9 μm
Bunches per beam	2835
Beam current	0.53 A
Magnetic field strength	8.33 T
Dipole magnetic temperature	1.9 K

- LHC Beauty experiment (LHCb); [76]
- LHC forward (LHCf); [77] and
- Total Cross Section, Elastic Scattering and Diffraction Dissociation experiment (TOTEM) [78]

The LHC was designed for an envisaged luminosity of 10^{33} $\mathrm{cm}^2\mathrm{s}^{-1}$ for its pp operational run. Luminosity is a measure of the machine that is described in appendix A. The LHC is expected to provide energy ranges and luminosity values greater than any hadron-hadron collider. A comparison of the expected LHC start-up energy and luminosity with those of previous proton (anti-)proton facilities is shown in figure 3.2. The main features of the LHC as a heavy ion accelerating facility can be found in [79].

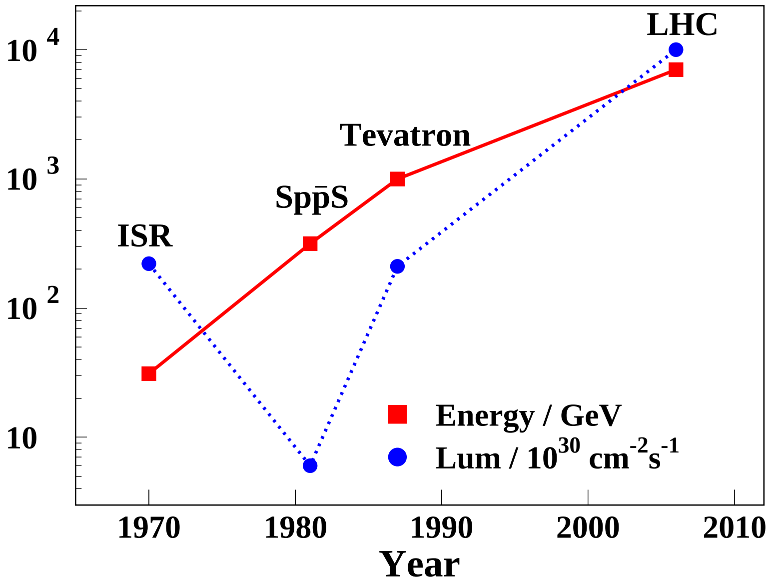

Figure 3.2: Energy (solid lines) and luminosity (dotted lines) of various proton (anti-)proton experiments plotted against their start-up year [73].

3.2 ALICE detector

ALICE is a general-purpose heavy-ion experiment whose detectors will measure and identify mid-rapidity hadrons, leptons and photons produced in the interactions. A unique design, with a very different optimisation from those chosen by the dedicated proton-proton experiments at LHC, has been adopted for ALICE. The ALICE detector was designed for charged-particle densities up to $dN_{ch}/d\eta$=4,000. The ALICE tracking and particle identification performance is checked up to $dN_{ch}/d\eta$=8,000, while the physical observables has been studied up to $dN_{ch}/d\eta$=6,000 with the HIJING event generator [80] to simulate the Pb-Pb collisions. The Heavy-Ion Jet INteraction Generator (HIJING) is a Monte Carlo generator that combines a QCD-inspired model of jet production with the Lund Model for jet fragmentation. The particle densities to be explored by ALICE range from pp values $dN_{ch}/d\eta \leq 10$ at the commissioning stage, through pA values (few times higher), up to Pb-Pb collisions [4]. The overall dimensions of ALICE are 16 × 26 m with a total weight of approximately 10,000 t.

3.2.1 Running conditions

Four different running modes are envisaged for the ALICE detector: Pb-Pb; Ar-Ar (high rate); Ar-Ar (low rate); proton-proton. Other modes, such as pA collisions are going to take place further in the future. The principal features of the four currently considered running modes are given in table 3.2.

3.2.2 Sub-detector layout

The ALICE experiment, as shown in figure 3.3, consists of a central detector system, covering mid-rapidity ($|\eta| \leq 0.9$) over the full azimuth, and several forward systems such as a forward muon arm. Figure 3.4 shows a two dimensional cut view of the

Table 3.2: Characteristics for different running modes in ALICE.

	Pb-Pb	Ar-Ar (high rate)	Ar-Ar (low rate)	pp
Luminosity ($\mathrm{cm}^{-2}\mathrm{s}^{-1}$)	10^{27}	10^{29}	2.8×10^{27}	10^{31}
Multiplicity density	6,000	1,200	1,200	6.5
Interaction rate (Hz)	8,000	2.7×10^{5}	8,000	10^{5}
L0 trigger rate (Hz)	5,000	≤1,000	5,000	30,000

ALICE detector along the rz direction (upper part) and along the xy direction (lower part).

The central system is installed inside a large solenoidal magnet which generates a magnetic field of up to 0.5 T. The central barrel system includes, from the interaction vertex to the outside, six layers of high-resolution silicon detectors (Inner Tracking System – ITS), the main tracking system of the experiment (Time-Projection Chamber – TPC), a transition radiation detector for electron identification (Transition-Radiation Detector – TRD), and a particle identification array (Time-Of-Flight – TOF). The central system is complemented by two small-area detectors: an array of ring-imaging Cherenkov detectors ($|\eta| \leq 0.6$, 57.6° azimuthal coverage) for the identification of high-momentum particles (High-Momentum Particle Identification Detector–HMPID), and an electromagnetic calorimeter ($|\eta| \leq 0.12$, 100° azimuthal coverage) consisting of arrays of high-density crystals (PHOton Spectrometer – PHOS). The central barrel detectors measure hadrons, electrons and photons (see section 3.3).

Table 3.3 shows a summary of the acceptance and location of the central barrel detectors (ITS, TPC, TRD, TOF and HMPID)[1]. Notice that the ALICE coordinate axis system is a right-handed orthogonal Cartesian system with the point of origin at the beam interaction point. The axes are defined as follows: x-axis is perpendicular to the mean beam direction, aligned with the local horizontal and pointing to the accelerator centre; y axis is perpendicular to the x-axis and to the mean beam direction, pointing upward; z-axis is parallel to the mean beam direction. Hence, the positive z-axis is pointing in the direction opposite to the muon spectrometer.

Table 3.3: Summary of the ALICE detector subsystems ITS, TPC, TRD, TOF and HMPID.

Detector	Acceptance (η, ϕ)	Position (m)	Dimension (m^2)	Channels
ITS layer 1,2 (SPD)	± 2, ± 1.4	0.039, 0.076	0.21	9.8 M
ITS layer 3,4 (SDD)	± 0.9, ± 0.9	0.150, 0.239	1.31	133 000
ITS layer 5,6 (SSD)	± 0.97, ± 0.97	0.380, 0.430	5.0	2.6 M
TPC	± 0.9 at r=2.8 m	0.848, 2.466	readout 32.5 m^2	557 568
	± 1.5 at r=1.4 m		Vol. 90 m^3	
TRD	± 0.84	2.90, 3.68	716	1.2 M
TOF	± 0.9	3.78	141	157 248
HMPID	± 0.6, $1.2^\circ < \phi < 58.8^\circ$	5.0	10	161 280

The forward rapidity systems include a muon spectrometer ($-4.0 \leq \eta \leq -2.5$, on the RB26 side of the solenoid), a photon counting detector (Photon Multiplicity Detector – PMD, on the opposite side), and an ensemble of multiplicity detectors (Forward Multiplicity Detector – FMD) covering the large rapidity region (up to $\eta = 5.1$). A system of scintillators and quartz counters (T0 and V0) will provide fast trigger signals, and two sets of neutron and hadron calorimeters, located about 115 m away from the interaction vertex, will measure the centrality (Zero-Degree Calorimeter – ZDC). An absorber positioned very close to the vertex shields the muon spectrometer. The spectrometer consists of a dipole magnet, five tracking stations, an iron wall (muon filter) to absorb remaining hadrons, and two trigger stations behind the muon filter [4].

A description of the ALICE Trigger System is given in Chapter 4. A description of the Data Acquisition (DAQ) and High Level Trigger (HLT) systems can be found in [81]. The High-Level Trigger (HTL) is a farm of up to 1,000 multiprocessors personal computers (PCs) which will deal with the complete events that are subject to an on-line analysis; it can either select or reject events in order to reduce the event size (region of interest), and also can compress the complete event information. On the other hand, the DAQ system was designed to cope with the relatively short LHC heavy-ion runs in a way that it can collect a sufficient number of events in the high charged-particle multiplicity environment; a recording rate of 1.25 GB/s to permanent storage has been required in Pb-Pb collisions.

---

[1] The acceptance in η is calculated from the nominal interaction point and is 360° in azimuth, unless noted otherwise. The position is the approximate distance from the interaction point to the face of the detector and corresponds to the radius for barrel detectors (inner and outer radius for the TPC and TRD) or the position along the beam (z coordinate) for the others. The dimension corresponds to the total area covered by active detector elements. 'Channels' is the total number of independent electronic readout channels. In case a detector is subdivided, the numbers refer to the individual components (e.g. pixel layers 1 and 2, muon tracking stations 1–5).

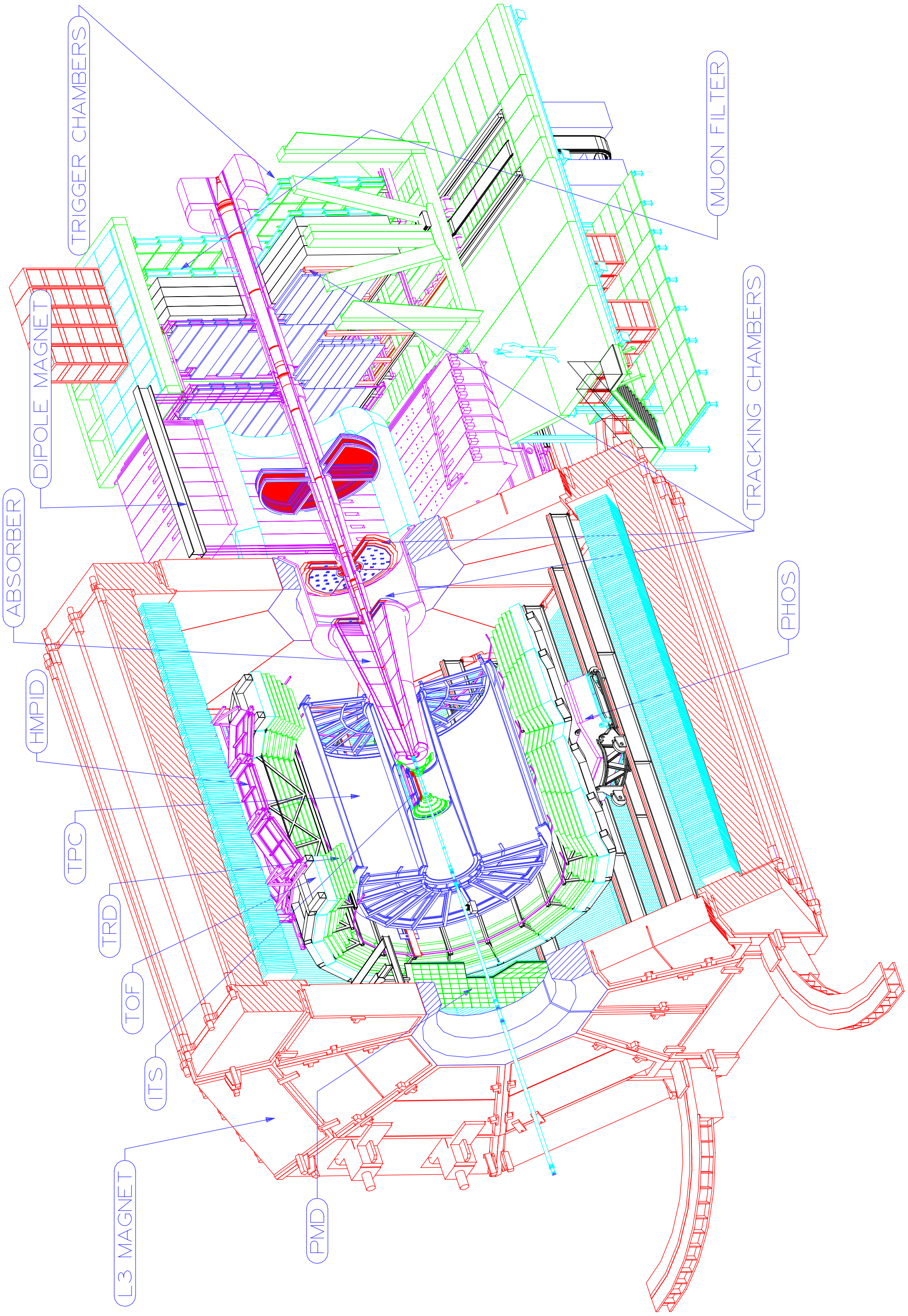

Figure 3.3: The ALICE detector schematic layout. The acronyms on this figure are described in section 3.2.2

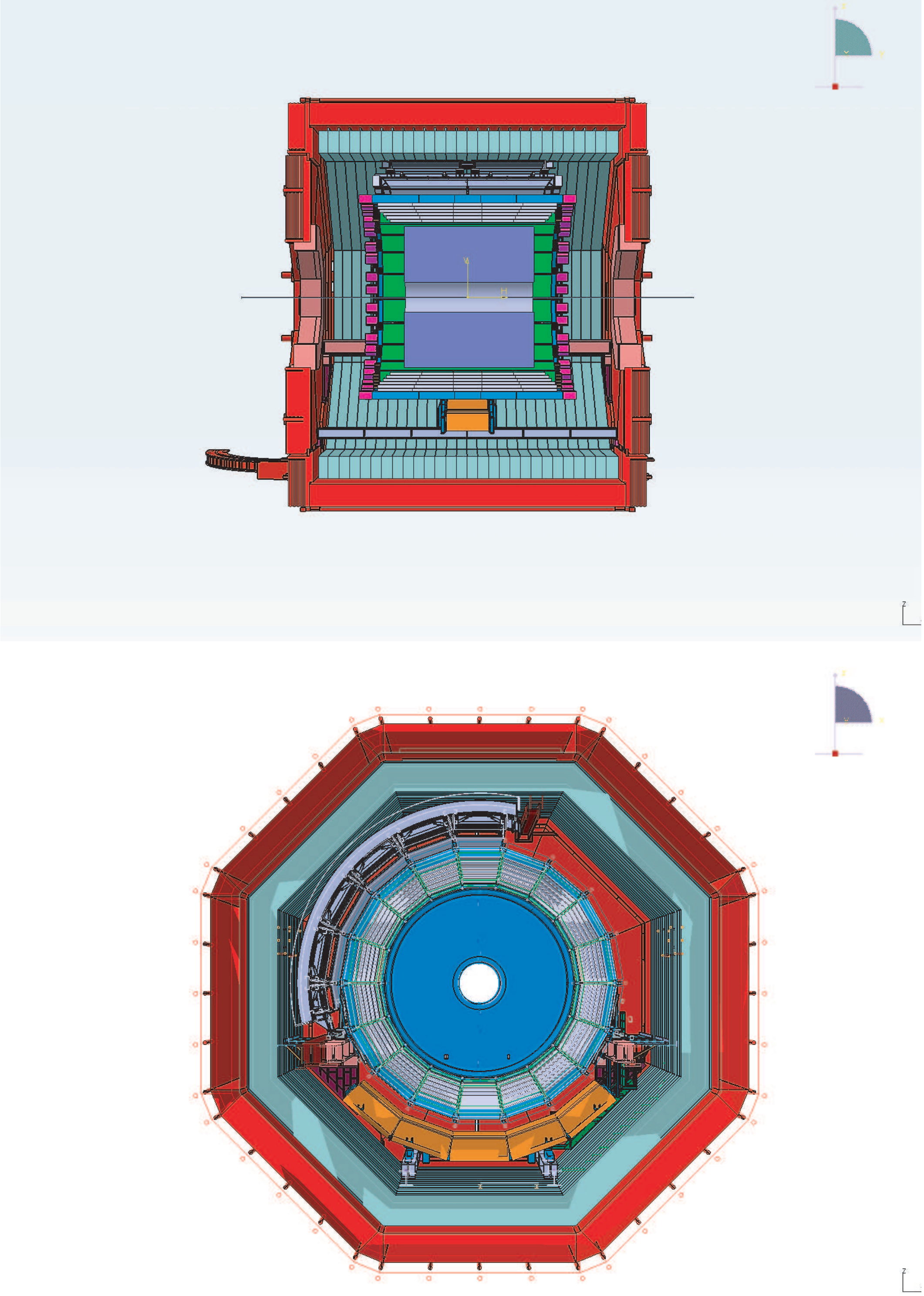

Figure 3.4: ALICE 2D cut views along the rz direction (upper part) and along the xy direction (lower part). The L3 experiment magnet is 12.1 m long and 5.75 m in radius

3.2.3 Inner Tracking System (ITS)

The Inner Tracking System (ITS) consists of six cylindrical layers of silicon detectors, of three types of collection of detectors (see below). A complete description was given in the ITS Technical Design Report [82]. This detector aims to measure the position of the primary vertex and of the first points on the tracks. In order to do that, the ITS was designed to have an angular resolution as good as possible. It will provide accurate measurements of track impact parameters that will enable the identification of secondary tracks of mesons with open charm and beauty, as well as the identification of hyperons. Figure 3.5 shows the ITS layout. The innermost radius in the ITS is only limited by the beam pipe radius of 3 cm. Similarly, the outermost radius of 44 cm is determined by the matching of the Time Projection Chamber (TPC), which forms the next layer in the detector.

The innermost layers are provided by silicon-pattern detectors known as Silicon Pixel Detectors (SPS) and Silicon Drift Detectors (SDD). This was required as the granularity of the detectors needs to be kept at a high level to be able to cope with the envisaged high multiplicity environment. The outermost radius uses double-sided Silicon Strip Detectors (SSD) technology. Performance studies have confirmed that by combining the three ITS technologies (2 layers of pixels, 2 layers of drifts and 2 layers of strips), the track impact parameter resolution is kept to a good level to cope with the physics requirements. Table 3.4 shows some parameters of the three detector types.

The ITS can localise the primary vertex with a resolution better than 100 μm in Z and much better in X and Y, and can be used on the reconstruction and identification of particles with low momentum $p <$ 100-200 MeV/c. By using dE/dx measurements, the ITS can also provide information about particle ID in the four outermost layers. The thickness of those layers is about 300 μm, as the material budget was designed to be as small as possible.

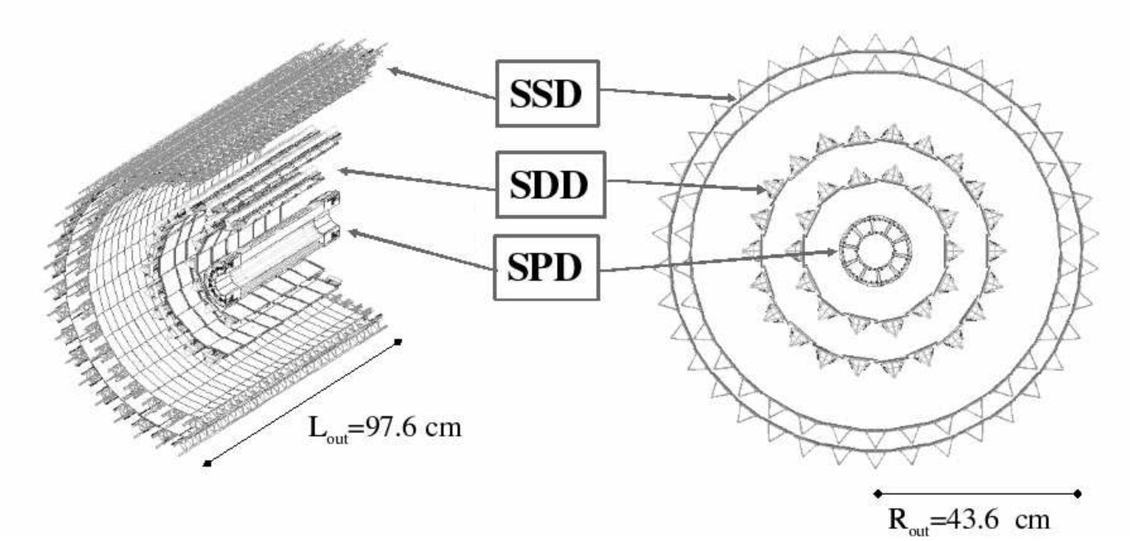

Figure 3.5: The Inner Tracking System (ITS) layout.

3.2.4 Time Projection Chamber (TPC)

The TPC is the main tracking detector of the ALICE central barrel, and together with the other central barrel detectors, has to provide charged-particle momentum measurements with good two-track separation, particle identification information (from dE/dx measurement), and secondary vertex determination.

Design considerations

The Time Projection Chamber was invented in the late 1970s, and is a device in which ionisation is produced by charged-particles in a large gas-filled volume. The presence of a uniform electric field drifts the charge towards the anode detectors (pads). ALICE is designed to work with very high multiplicity events and yet maintain a good signal-to-noise ratio.

The TPC is cylindrical in shape and has an inner radius of about 44 cm, an outer radius of about 250 cm, and an overall length along the beam direction of 500 cm. The detector is made of a large cylindrical field cage, filled with 88 m^3 of

Table 3.4: Inner Tracking System parameters. The occupancy was calculated assuming particle density of dN_{ch}/dy=8,000 for Pb-Pb collisions.

Parameter	Silicon pixel	Silicon drift	Silicon strip
Radius (inner layer) [cm]	4	14	39
Radius (outer layer) [cm]	7	24	44
Cell size (rϕ×z) [μm^2]	50×425	150×300	95×40,000
Spatial precision (rϕ×z) [μm^2]	12×120	38×28	20×830
Readout channels [k]	9,835	133	2,719
Av. occup. (inner layer) [%]	2.1	2.5	4
Av. occup. (outer layer) [%]	0.6	1.0	3.3
Thickness per layer [% of X_0]	1.24	0.95	0.90

$Ne/CO_2/N_2$ (90: 10: 5) which is needed to transport the primary electrons over a distance of up to 2.5 m on either side of the central electrode to the end-plates.

The TPC is the main detector for the study of hadronic observables in both heavy-ion and proton-proton collisions. Hadronic measurements give information on the flavour composition of the particle-emitting source via the spectroscopy of strange hadrons, on its space-time evolution and extent at freeze-out via single and two-particle spectra correlations, and on event-by-event fluctuations. On the other hand, electrons identified by the central barrel tracking detectors whose impact parameters are determined using the ITS can be used to measure charm and beauty-particle production.

3.2.5 Transition-Radiation Detector (TRD)

The Transition Radiation Detector (TRD) is composed of modules placed outside the TPC, covering the same rapidity region and used for tracking and particle identification. The TRD was designed to provide electron identification in the central barrel

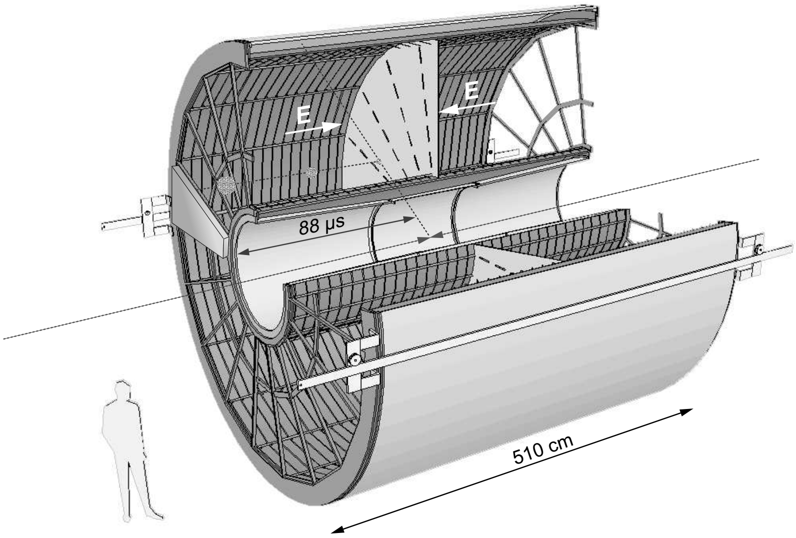

Figure 3.6: The Time Projection Chamber (TPC) layout.

for momenta greater than 1 GeV/c, where the pion rejection capability through energy loss measurement in the TPC is no longer sufficient. The TRD will provide, along with data from the TPC and ITS, good enough electron identification to measure the production of light and heavy vector meson resonances and the dilepton continuum spectrum both in Pb-Pb and pp collisions. In addition, the TRD will supply tracking information, which can be combined with information from the ITS and TPC to obtain a better tracking resolution.

3.2.6 Particle identification detectors

The ITS and TPC detectors provide particle identification (PID) by using specific ionisation energy loss, dE/dx. Moreover, in fact, it can be stated that ALICE employs all known PID techniques as it makes use of time-of-flight, transition and Cherenkov radiation, electromagnetic calorimetry, muon filters and topological decay reconstruction. Some of these PID techniques are used in the analysis of ϕ mesons described in chapter 9.

Charged hadrons can be identified using the information of a single detector or by combining information from various detectors (ITS, TPC, TRD, TOF and HMPID); in the case of electrons the identification is performed using the TPC and TRD detectors, and by using the EMCal the purity of the electron sample can be improved for high transverse momentum particles. As its name suggests, the PHOS detector identifies photons (as does the EMCal detector); below and up to 20 GeV/c the direct-photon yields are obtained from invariant mass analysis by subtracting the background from π^0, η and ω particles, and up to about 100 GeV their identification is carried out on an event-by-event basis. In the forward pseudo-rapidity range, the PMD detector can provide photon multiplicity. Muons can be identified in the pseudo-rapidity region $-4.0 < \eta < -2.5$ using the forward muon spectrometer.

Beyond the TRD, a Time of Flight (TOF) barrel measures the transit time of individual particles coming from the TPC. This system is complemented by a proximity-focusing RICH detector (High Momentum Particle IDentification system – HMPID) with a more limited solid angle coverage. This system allows particle identification for a sample of particles over a large momentum range. For example, protons can be identified in the HMPID system up to around 5.3 GeV/c.

The TOF barrel is part of the particle ID system for charged particles at intermediate momentum range. It covers an area delimited by an internal radius of 370 cm and an external one of 490 cm, having an overall longitudinal length of 7.45 m. TOF works by using the principle of charged particle ionisation. The "time of flight" is usually defined as the interval between the production of particles and their detection on the detector. The principle is that the velocity of particles of a given momentum depends on their mass. By knowing the time of flight, the momentum and the distance travelled by the particles, their masses can be obtained. When two particles have the same momentum p, the difference of time of flight is given by

$$\Delta t = \frac{\mathrm{L}c}{2p^2}(m_1^2 - m_2^2), \tag{3.1}$$

where m_1 and m_2 correspond to the particle masses and L is the associated track length. The time resolution of the TOF (between 60 to 80 ps) can allow the separation of pions from kaons and kaons from protons in the energy range of 2.5 to 4 GeV/c.

3.2.7 Forward and trigger detectors

The forward detectors were designed for different purposes. They will be used to extend the measurement of charged particles (FMD) and photons (PMD) at large values of rapidity, and to characterise the event in terms of the collision centrality or trigger interaction (T0, V0, and ZDC). Figure 3.5 presents a summary of the acceptance in pseudo-rapidity and azimuthal angle as well as their location. Because the V0 triggers are used in chapter 7 and to some extend on chapter 9, this section focuses mainly on the V0 forward detector [83].

The V0 is a small angle detector located on either side of the ALICE interaction point. The V0 detector is composed of two arrays of scintillator counters, known as the V0A and V0C detectors (2.5 and 2.0 cm in thickness of the BC404 scintillating material for V0A and V0C respectively) [84]. V0A is located 340 cm from the vertex on the side opposite to the muon spectrometer, while the V0C array is found 90 cm from the vertex, next to the front face of the hadronic absorber. V0 covers the pseudo-rapidity range $2.8 < \eta < 5.1$ (V0A) and $-3.7 < \eta < -1.7$ (V0C). Figure 3.7 shows the segmented parts of the array which is composed of counters arranged in four rings. Table 3.6 shows the pseudo-rapidity ranges and angular acceptances for each of the rings.

The V0 detector provides several functions both in pp and nucleus-nucleus collisions. It detects forward and backward particles at small angles to the beam, and it can estimate the position of the interaction point by comparing the very small time differences between the signals arriving at the forward and backward detectors. It

Table 3.5: Summary of the ALICE detector forward subsystems (ZDC, PMD, FMD, V0 and T0).

Detector	Acceptance (η, ϕ)	Position (m)	Dimension (m^2)	Channels
ZDC:ZN	$\lvert\eta\rvert < 8.8$	±116	2×0.0049	10
ZDC:ZP	$6.5 < \lvert\eta\rvert < 7.5$ $-9.7° < \phi < 9.7°$	±116	2×0.027	10
ZDC:ZEM	$4.8 < \eta < 5.7$, $-16° < \phi < 16°$ and $164° < \phi < 196°$	7.25	2×0.0049	2
PMD	$2.3 < \eta < 3.7$	3.64	2.59	2 221 184
FMD disc 1	$3.62 < \eta < 5.03$	inner: 3.2	0.266	51 200
FMD disc 2	$1.7 < \eta < 3.68$	inner: 0.834 outer: 0.752		
FMD disc 3	$-3.4 < \eta < -1.7$	inner:−0.628 outer:−0752		
V0A	$2.8 < \eta < 5.1$	3.4	0.548	32
V0C	$-1.7 < \eta < -3.7$	−0.897	0.315	32
T0A	$4.61 < \eta < 4.92$	3.75	0.0038	12
T0C	$-3.28 < \eta < -2.97$	−0.727	0.0038	12

can also count the multiplicity of forward and background particles in a given interaction and hence it can not only trigger on an interaction taking place but it can also provide information on the centrality of the collision.

The V0 minimum-bias triggers are given by particles coming from the initial collision or from secondary interactions in the vacuum chamber elements. The V0 detector will be used to provide an indication of the centrality of the collision via the multiplicity recorded in the event. Rough centrality triggers (known as multiplicity, semi-central and central triggers) can be obtained for example by selecting

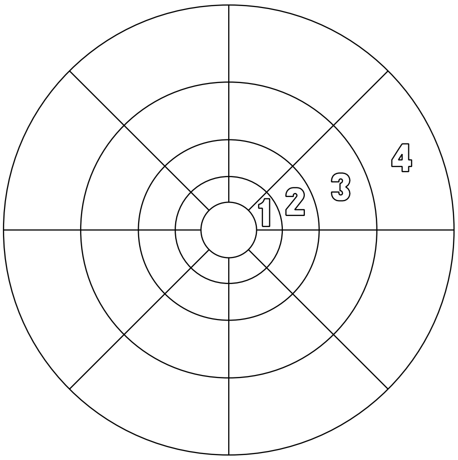

Figure 3.7: Segmentation of the V0A/V0C arrays.

the number of fired counters in the array.

During normal running operations, it is expected that both arrays will be required, i.e. AND mode, to provide triggers currently known as Minimum Bias trigger (MB), Multiplicity trigger (MT), semi-Central Trigger (CT1) and Central Trigger (CT2); an OR mode can also be used.

3.2.8 Electromagnetic calorimeters and cosmic ray detector

There are two electromagnetic calorimeters in ALICE (see table 3.7): PHOS [85] and EMCal [86]. The Photon Spectrometer (PHOS) was designed to detect electromagnetic particles with high efficiency for photon identification and some neutral mesons via their decay channel to photons from low to moderate transverse momentum. Its coverage in pseudo-rapidity is $-0.12 \leq \eta \leq 0.12$ and an azimuthal angle of $\Delta\phi = 100^\circ$. It is composed of a scintillator material of 20 X_0 thickness made of lead-tungstate crystal ($PbWO_4$). In addition, another electromagnetic calorimeter (EMCAL) of coverage in phase space of $-0.7 \leq \eta \leq 0.7$ and $\Delta\phi = 110^\circ$ aims to have an acceptance as large as possible providing in some cases back-to-back coverage within the PHOS calorimeter. It is a shashlik-type Pb-scintillator calorimeter

Table 3.6: V0A and V0C arrays. Pseudo-rapidity and angular acceptances (deg.) of the rings.

Ring	V0A		V0C	
	η_{max}/η_{min}	$\theta_{min}/\theta_{max}$	η_{min}/η_{max}	$\theta_{max}/\theta_{min}$
1	5.1 / 4.5	0.7 / 1.3	−3.7 / −3.2	177.0 / 175.3
2	4.5 / 3.9	1.3 / 2.3	−3.2 / −2.7	175.3 / 172.4
3	3.9 / 3.4	2.3 / 3.8	−2.7 / −2.2	172.4 / 167.5
4	3.4 / 2.8	3.8 / 6.9	−2.2 / −1.7	167.5 / 159.8

with cylindrical geometry, located adjacent to the ALICE magnet coil. Both detectors were designed to study the regime of hard physics.

Table 3.7: Summary of the ALICE detector subsystems of the electromagnetic calorimeters (PHOS and EMCal) and cosmic ray detector (ACORDE).

Detector	Acceptance (η, ϕ)	Position (m)	Dimension (m^2)	Channels
PHOS	± 0.12, $220° < \phi < 320°$	4.6	8.6	17 920
EMCal	± 0.7, $80° < \phi < 187°$	4.36	44	12 672
ACORDE	± 1.3, $-60° < \phi < 60°$	8.5	43	120

A detector, ACORDE, placed on the upper faces of the magnet was designed to provide cosmic ray triggers at the L0 level that can be used for calibration and alignment purposes of the main tracking detectors. Its pseudo-rapidity coverage is $-1.3 \leq \eta \leq 1.3$ and azimuthal coverage $3/4\pi$, and is composed of an array of plastic scintillator counters (see table 3.7). It can also trigger on atmospheric high energy cosmic rays; a study that is expected to cover the energy region above the "knee" in the cosmic ray spectrum ($\simeq 3{\times}10^{15}$eV) [4].

3.2.9 Muon spectrometer

In heavy-ion operation, the Muon Spectrometer can identify muons with momentum above 4 GeV/c allowing the study of heavy-quark vector mesons and the $\phi \rightarrow \mu^+\mu^-$ meson. It can also provide electron-muon coincidences at $-2.5 \leq \eta \leq -1.0$ where the electrons identification is given by the TRD. Its coverage is $-4.0 \leq \eta \leq -2.5$ with azimuthal angle of 2π and $2^\circ \leq \theta \leq 9^\circ$ for polar coverage. Its tracking chambers were designed for a spatial resolution of about 100 μm in order to cope with an invariant mass resolution of the order of 100 MeV/c^2 (Υ mass).

3.3 ALICE performance

Track finding is one of the most challenging tasks ahead in ALICE as the particle densities are unprecedented in magnitude. The first part consists in carrying out the reconstruction of the primary vertex using the correlation of the hit positions in the two innermost pixel detectors, leading to the position of the primary vertex which is used as a constraint to start the tracking of primary particles in the TPC and for the subsequent follow up of the track finding. Secondary particles are found after a further tracking pass, and the task is completed with the secondary vertices reconstruction. In addition, kink topologies can also be used.

The primary vertex determination, track reconstruction and impact parameter calculation in the central part of ALICE is described, as well as the particle identification (PID) for charged-hadrons, in the following sections. Details on the muon track reconstruction, on-line tracking, event filtering and neutral PID can be found in different documents [4, 15].

3.3.1 Primary vertex determination

The information provided by the two innermost layers of the ITS (Silicon Pixel Detector - SPD) is used to carry out the reconstruction of the primary vertex position. Pairs coming from the reconstructed point of these two layers are selected as they have a close azimuthal angle in the transverse plane. By using a linear extrapolation of the z-position of the primary vertex, the pair's z-coordinate is estimated, and by following a similar procedure the transverse plane is also estimated. Although such a linear extrapolation might be considered to be a crude estimation due to the bending in the magnetic field, the short distances of the pairs to the interaction point makes the transverse coordinates of the primary vertex good enough to be used as a constraint for a first pass of the tracking procedure. In normal operation, when the beam position is stable, the transverse position can be obtained by averaging over many events.

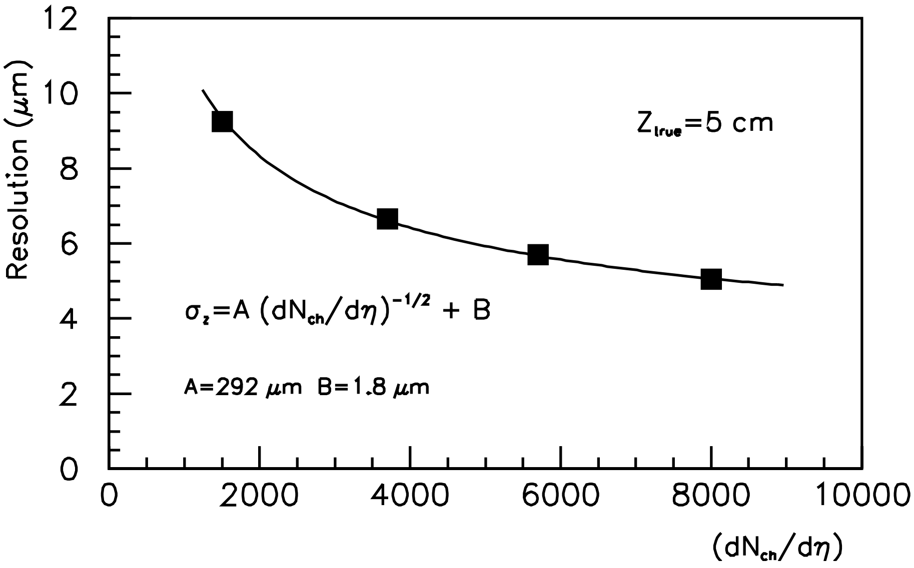

Figure 3.8: Resolution of the reconstructed vertex position as a function of the charged-particle density. The solid line is the result of a fit using the parametrisation given by equation 3.2.

The track multiplicity, i.e. the charged-particle density, has been taking into account in the resolution of the primary vertex position. Figure 3.8 shows this resolution in the z-coordinate (known as σ_z), at z=5cm, in terms of the track multiplicity. This expression is given by:

$$\sigma_z = \frac{A}{\sqrt{\mathrm{d}N_{\mathrm{ch}}/\mathrm{d}\eta}} + B, \tag{3.2}$$

where A is typically 290 μm and B is a constant of a few microns that depends on the residual misalignment of the silicon pixel layers. A vertex-position resolution of less than 10 μm has been obtained for heavy-ion charged-particle densities, while a resolution of 150 μm is obtained for the average proton-proton event where the charged-particle density is between 6 and 7. After the track reconstruction is performed, the final position of the primary vertex is determined by recalculating the measured track parameters.

The expected final resolutions in the z- and the transverse coordinates are shown

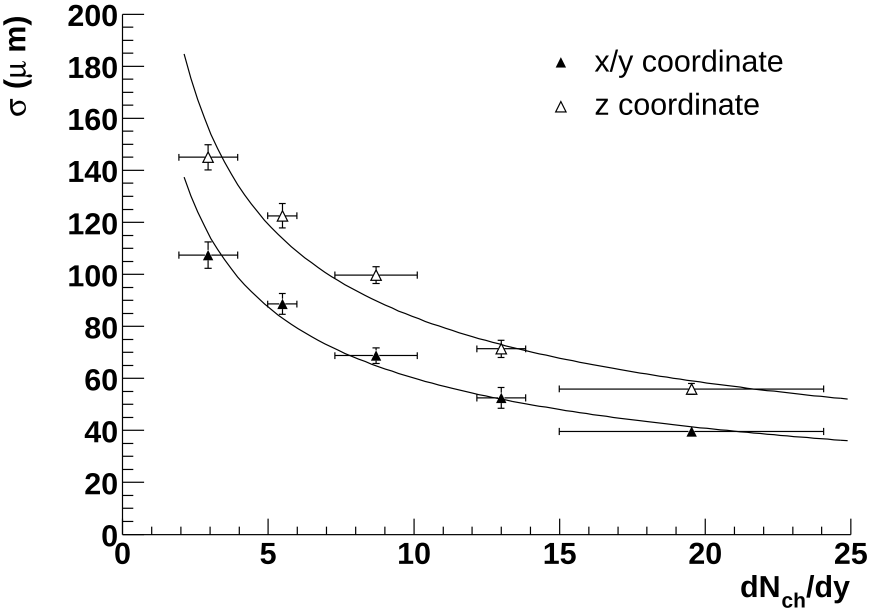

Figure 3.9: Resolution on the primary-vertex position as determined using reconstructed tracks, as a function of the charged-particle density for pp events.

in figure 3.9 for proton-proton collisions as a function of the track multiplicity. After performing the fit to equation 3.2, the value of A is found to be 270 μm for the z-coordinate and 210 μm for the x- and y-coordinates; and by averaging the pp multiplicity, a precision on the primary vertex position, after the tracking step, of 110 μm and 70 μm is obtained for the z-coordinate and transverse coordinates respectively.

3.3.2 Track reconstruction

The offline tracking in ALICE is carried out using a parallel Kalman filter approach [87, 88]. The Kalman filter is used for track finding and fitting, which depends on the determination of a set of initial seed values for the track parameters and their covariant matrix for each track. The current implementation starts in the outer part of the TPC, finding the overlapped clusters during tracking, followed by merging tracks to ITS. At this moment it is possible to obtain the tracks that are likely to be primary. The process continues by refitting tracks outwards by merging to the TRD and the outer detectors. In this second propagation, the track parameters and their covariance matrix are obtained. Several passes are considered with or without vertex constraints. For realistic particle densities ($dN_{ch}/d\eta$=2,000-4,000) the combined efficiency from all detectors is above 95% and the fake track probability below 5%.

In figure 3.10 the expected track-finding efficiency for primary tracks and the relative frequency of fake tracks as a function of transverse momentum for different charged-particle densities are shown. Fake tracks are defined here as those tracks that have more than one space point incorrectly assigned. Figure 3.11 shows the expected quality of the TPC-ITS track finding for different definitions of the tracks properly found and of the fake tracks.

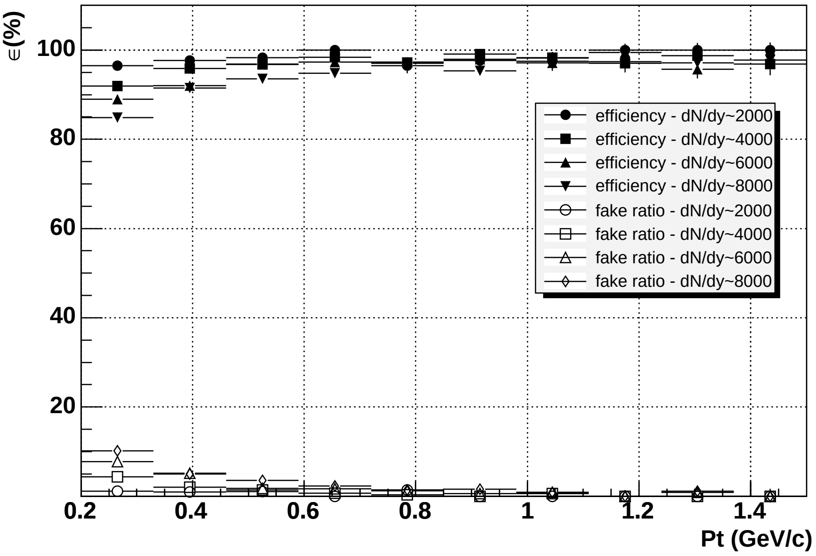

Figure 3.10: TPC and ITS track-finding efficiency and fraction of fake tracks as a function of transverse momentum for different track multiplicities.

The physical efficiency was also considered and defined as the efficiency normalised to the number of generated particles at the primary vertex within the central acceptance. The tracking momentum resolution at low momentum is dominated by

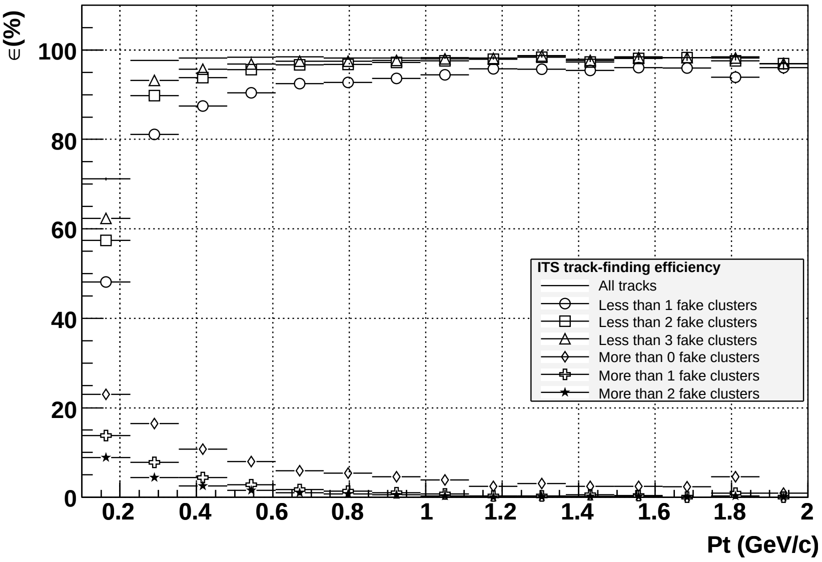

Figure 3.11: TPC and ITS track-finding efficiency and fraction of fake tracks for different amounts of wrongly associated ITS clusters ($dNd\eta = 6,000$).

ionisation-loss fluctuations and by multiple scattering. At high momentum it is determined by point measurement precision, and the alignment and calibration that, for the results presented here, were assumed to be ideal. Figure 3.12 shows the physical track-finding efficiencies for different combinations of the ITS, TPC and TRD detectors, as function of transverse momentum both for pp and Pb-Pb ($\mathrm{d}N_{ch}/d\eta =$ 6,000) collisions; this physical efficiency takes also into account decays and insensitive areas in the detectors. It can be seen from these figures that the combined TPC-ITS track finding efficiency is up to 90% at very high momentum, which is due to the size of the TPC dead zones that cover about 10% of the azimuthal angle. With the inclusion of the TRD a large drop is observed because of the additional decays that can take place in this region as well as additional dead zones, this is the reason why the TRD is only included as an optional option in the tracking procedure, i.e. it is only included when the precision in the physical efficiency is improved.

3.3.3 Impact parameter

In order to carry out analyses of short-lived particle decays, such as charm and beauty decays, the track parameters obtained both with and without the primary vertex constraint are stored for all tracks. The main performance parameter used for such studies is the resolution in the impact parameter, which is defined as the distance between the primary vertex and the track prolongation to the point of closest approach to the primary vertex. The resolution of the impact parameter depends both on the precision determination of the primary vertex position and the track parameters.

In figure. 3.13 the impact-parameter resolution in the transverse and longitudinal directions is shown for different particle species as a function of p_{t} in central Pb–Pb collisions. Additionally, figure 3.14 shows the impact-parameter resolution expected for two values of the charged-particle multiplicity in pp collisions. The quantity that is relevant for heavy-flavour studies is the impact-parameter resolution in the transverse direction, which as seen here it is significantly better than about 70 μm at $p_{\mathrm{t}} \sim 1$ GeV/c, and better than 40 μm at $p_{\mathrm{t}} \sim 2$ GeV/c in Pb-Pb collisions. The impact parameter resolution is similar for pp interactions. Since the $c\tau$ for D^0 meson is 123 μm, the ALICE impact parameter resolution will allow us to investigate heavy-flavour production.

3.3.4 Particle identification

Charged-hadron identification

A key feature of the ALICE experiment is its very good capability to identify charged and some neutral particles using a variety of detector techniques, which can resolve the different particle ambiguities presented at different momentum ranges. ALICE can combine the PID information from single detectors to cover the different kinematic limits, i.e. each detector that provides particle identification information has a different momentum-dependent performance. As mentioned in section 3.2.6, the ITS, TPC, TRD, TOF and HMPID detectors take part in the charged-particle identification (PID) system.

The information from each detector is used to assign to every track a set of probabilities, one for each particle type; the sum of these probabilities is normalised to one. The information from each detector is then combined in the second PID step that take into account the "a priori" probabilities using an iterative (Bayesian) procedure [4]; these probabilities indicate the populations of different particle species after the analysis cuts have been applied for each analysis.

The ITS can provide PID in the low-momentum range by measuring the ionisation energy loss dE/dx, in particular four layers of the ITS (two silicon-drift and two silicon-strip detector layers) are used to provide signal-amplitude information (see figure 3.15). The resolution of this measurement is about 11%, which means that a good separation of the π/K ratio of up to 450 MeV/c and p/K up to about 1 GeV/c can be achieved. The energy loss measurements in the TPC are carried out in a similar way, with an estimated resolution of 5.5% for pp interactions to 6.5% for central Pb-Pb collisions. The TRD detector also provides dE/dx measurements to contribute in the same momentum range as in the case of the TPC, its precision is estimated to 18-20%. The TRD can also provide electron identification information at the trigger level; it is expected to reject pions down to a level of 10^{-2} or better, for 90% electron detection efficiency. Charged-particle identification based on energy-loss measurements means that there is a momentum range around the minimum of the ionisation losses where the identification cannot be performed, this range is between 0.9 and 3 GeV/c and corresponds to the range of the TOF detector PID capability. The TOF detector allows one to extend the K/π separation out to 2.5-3 GeV/c and the p/K separation out to 3.5-4 GeV/c on a track-by-track basis.

For example, table 3.8 shows the momentum range over which kaons can be

Table 3.8: Momentum range over which kaons can be identified using the specified detector and technique. The mid-rapidity range (-0.9< η <0.9) was considered.

Range (GeV/c)	PID technique/sub-detector
0.1-0.5	dE/dx (ITS+TPC)
0.35-2.5	Time of Flight
1-3	HMPID
5-50	Relativistic rise (ITS+TPC)
0.3-13	Secondary vertex reconstruction

identified using a specified detector and technique. In particular, the ITS (see figure 3.16) and TPC (see figure 3.17), which give dE/dx measurements, cover the full central region and can be used to identify charged particles below 1 GeV/c. The TOF detector (see figure 3.18) is used for hadron identification by Time of Flight as mentioned earlier.

The ALICE efficiency and contamination for kaon PID (in ITS, TPC and TOF) as a function of momentum is shown in figure 3.19. The high momentum particle identification (HMPID) system was not included in this figure but can be used in the identification of kaons in the medium range of momentum, albeit with limited solid angle coverage. In addition, dE/dx measurements can be used again to identify kaons at high values of momentum using the relativistic rise phenomenon [15].

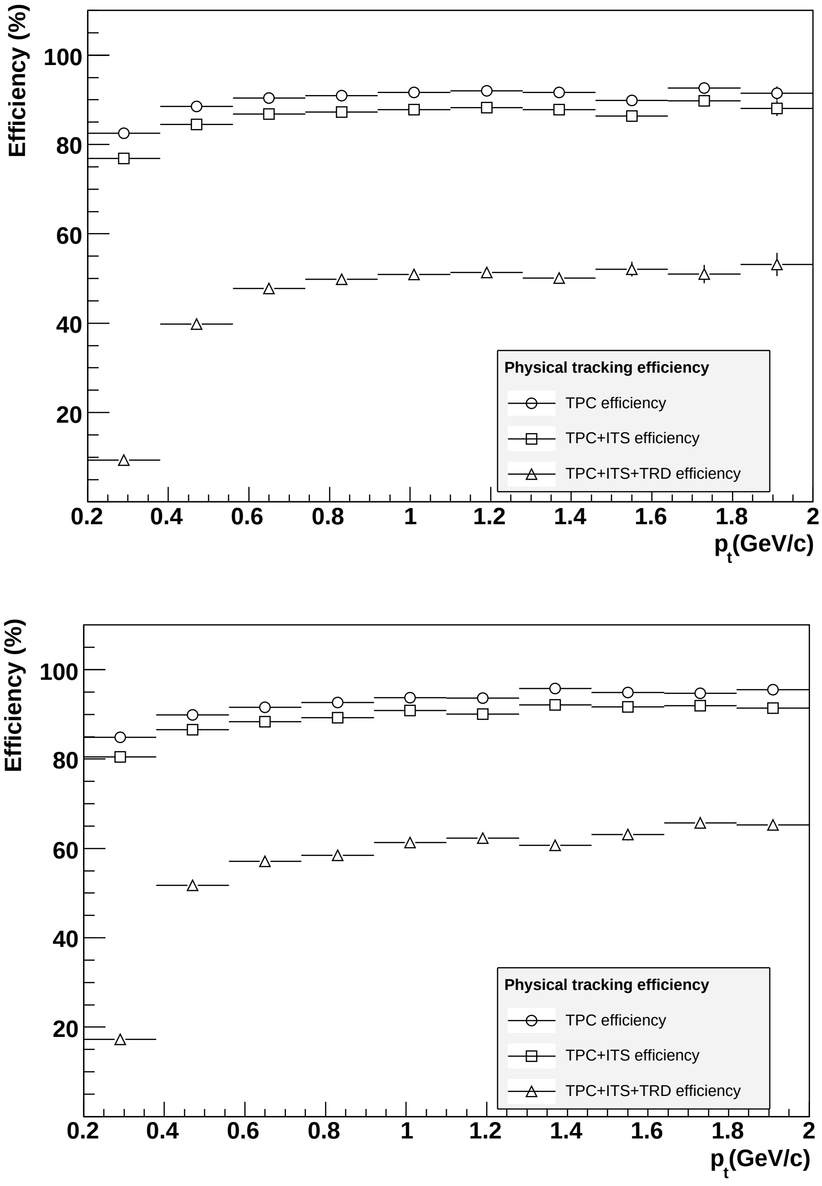

Figure 3.12: Physical track-finding efficiency, including acceptance effects for different combinations of the tracking detectors. Top: central Pb-Pb collisions ($dNd\eta = 6,000$). Bottom: pp collisions.

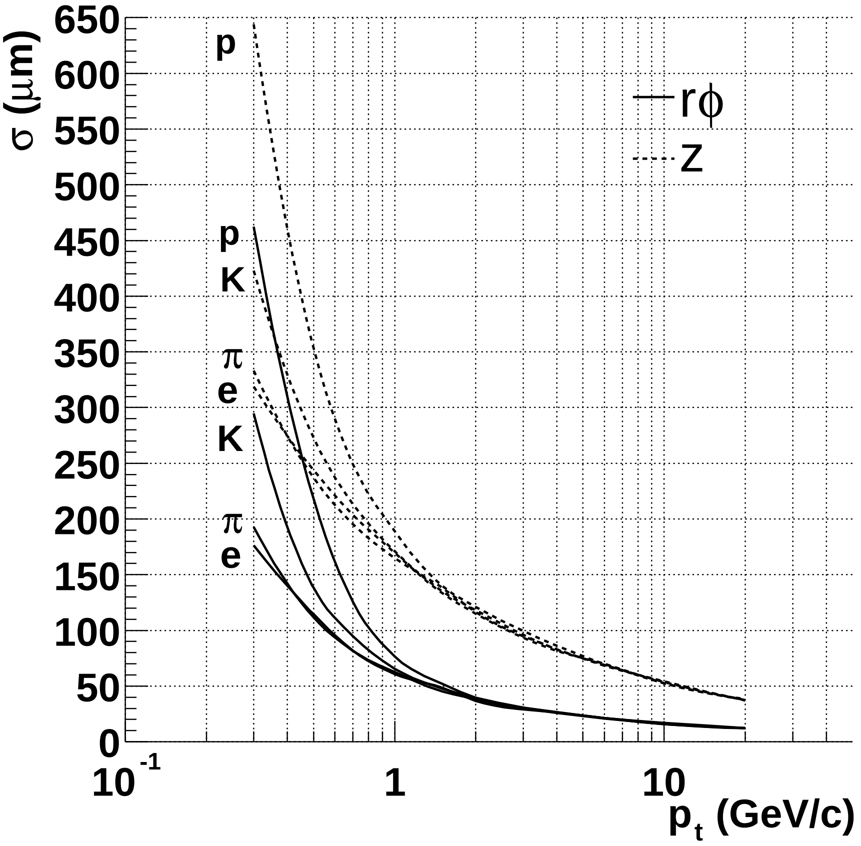

Figure 3.13: Impact parameter resolutions in central Pb–Pb collisions for electrons, pions, kaons and protons as a function of the transverse momentum. An assigned cluster in each one of the six ITS layers is required.

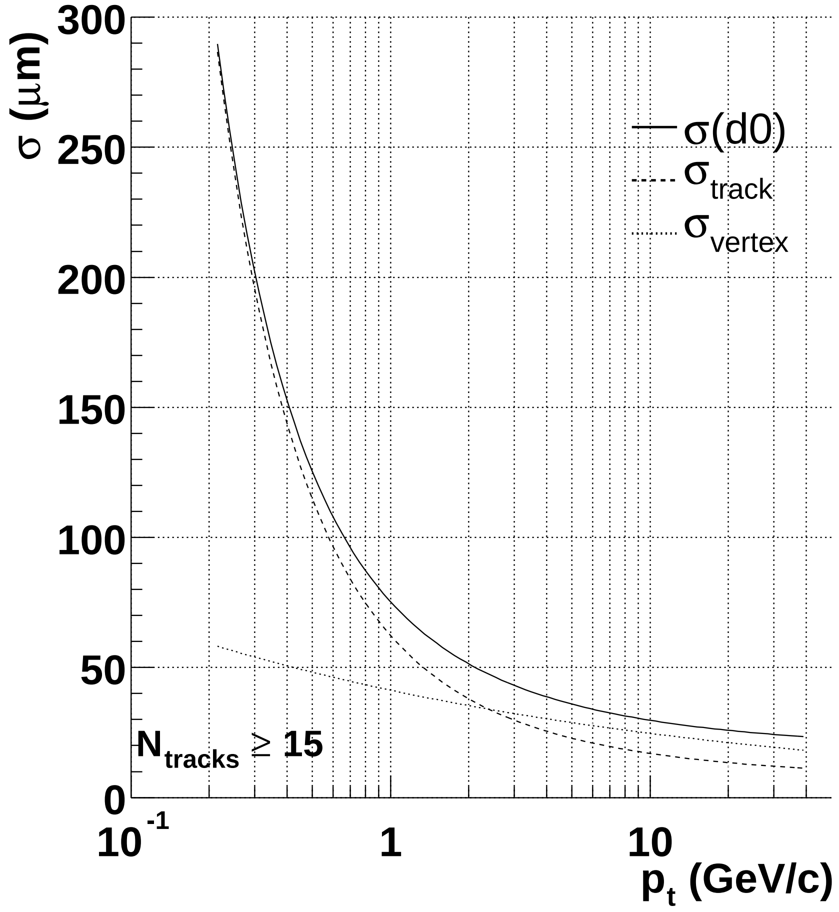

Figure 3.14: Impact-parameter resolution in the transverse plane as a function of the transverse momentum in pp collisions.

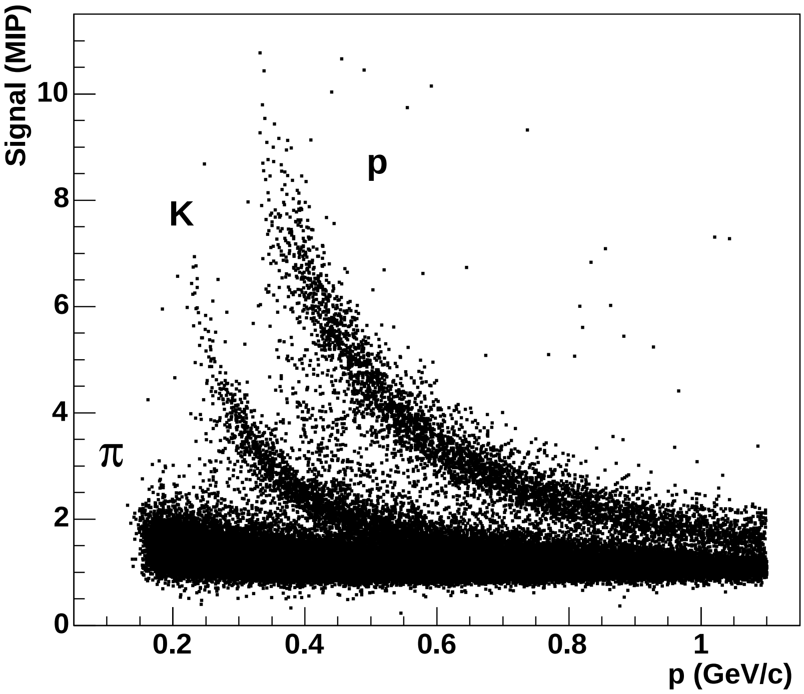

Figure 3.15: Plot of the correlation between the specific SDD/SSD signals (MIP units) calculated by the truncated mean method and the particle's momentum obtained from the TPC and ITS tracking for different particle species.

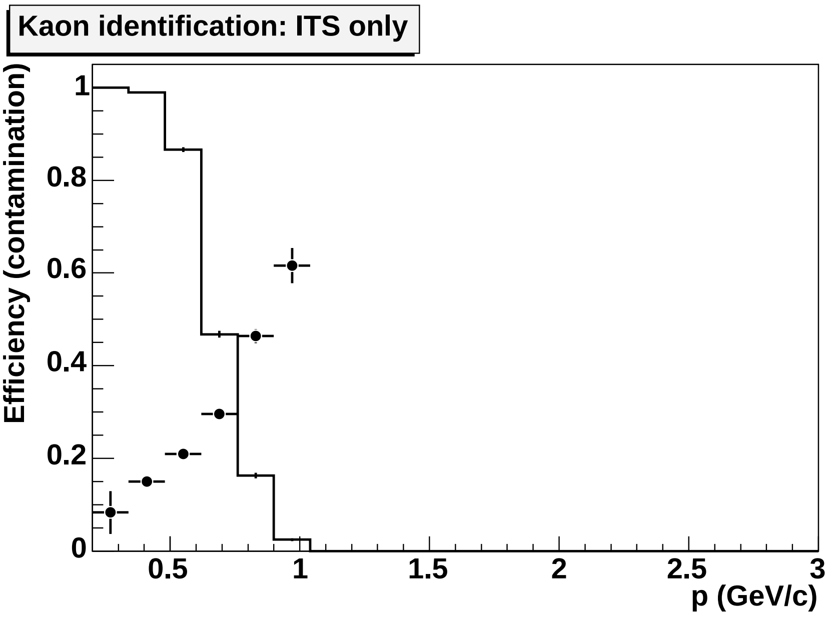

Figure 3.16: Single-detector efficiencies (solid line) and contaminations (points with error bars) for charged-kaon identification with the ITS stand-alone.

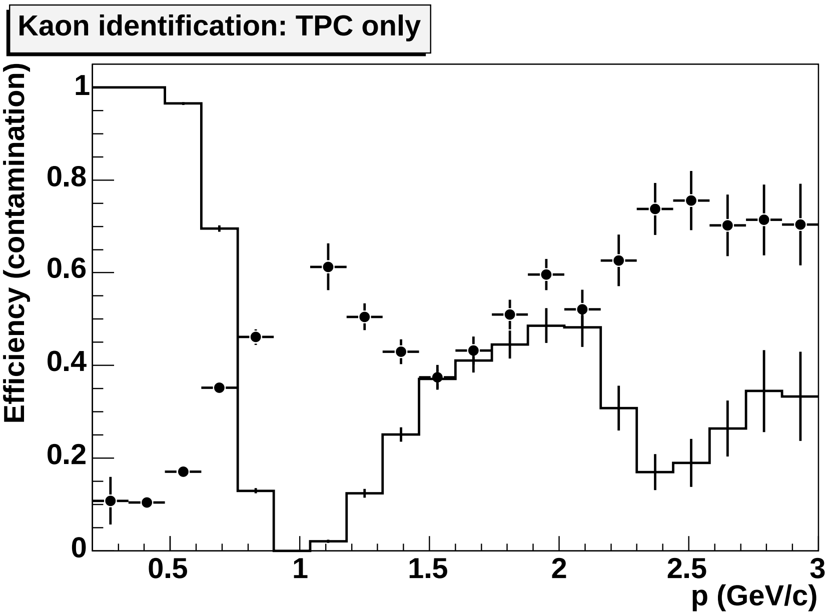

Figure 3.17: Single-detector efficiencies (solid line) and contaminations (points with error bars) for charged-kaon identification with the TPC stand-alone.

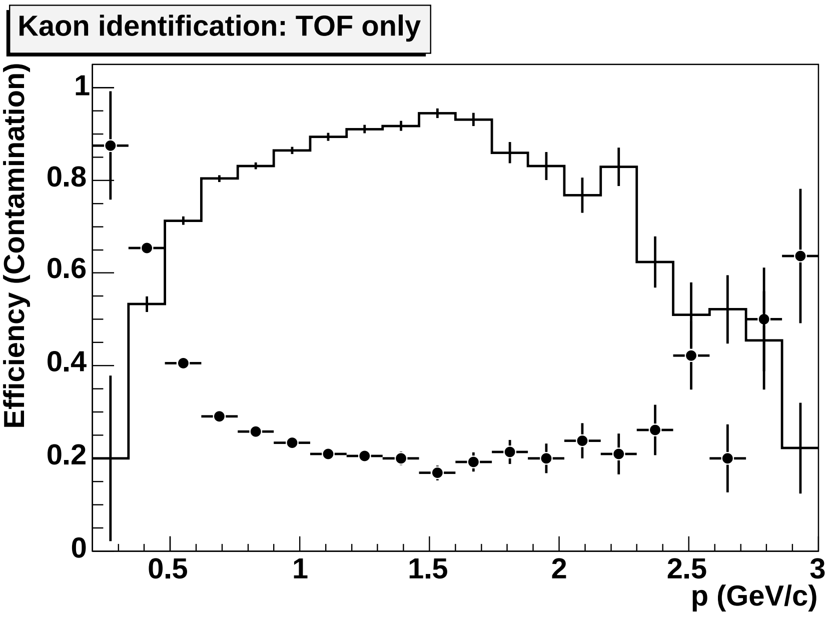

Figure 3.18: Single-detector efficiencies (solid line) and contaminations (points with error bars) for charged-kaon identification with the TOF stand-alone and combined.

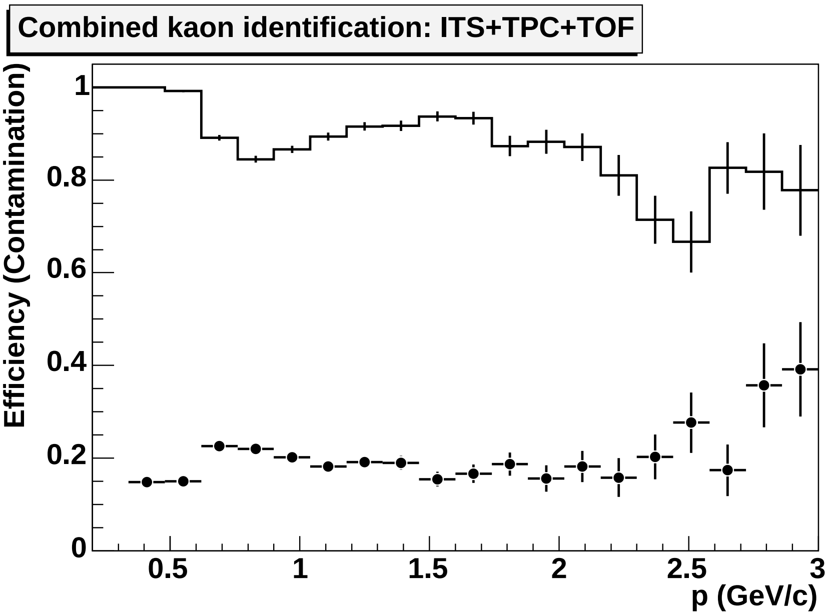

Figure 3.19: Single-detector efficiencies (solid line) and contaminations (points with error bars) for charged-kaon identification with the ITS, TPC and TOF stand-alone and combined.

3.4 Summary

In this chapter, an introductory guide to the LHC experimental facility was given. Particular attention was devoted to the ALICE sub-detectors that are relevant for the analysis that will be presented in chapter 7 and chapter 9. These are the central barrel detectors (ITS, TPC, TRD and TOF) and the V0 forward detector. An overview of the results obtained for detector performance both in pp and Pb-Pb collisions was also presented. The impact of detector performance on measurements of ϕ mesons will be discussed in chapter 9.

Chapter 4

The ALICE trigger system

In chapter 3 a description of the ALICE sub-detectors was given. In this chapter, the general operation of the ALICE trigger system is given; it includes its trigger levels and some of its most important features such as the past-future protection. In particular, the motivation for the current implementation of the ALICE trigger system will be discussed, and it will be compared to other trigger systems at the LHC.

4.1 The role of a trigger system

Before describing the ALICE trigger system, it is worthwhile introducing the general ideas behind any trigger system in the field of high energy physics (HEP). The aim of a trigger system is to select events as efficiently as possible; normally those events are rare in nature in the sense that they do not occur very often in particle collisions. Additionally, at the same time, the trigger system has to suppress those events that are not rate in nature but less interested from the physics point of view (background events).

In order to illustrate the issues behind such selection (and suppression) of events, let us assume that one has to find British tourists among the 18 000 000 inhabitants of Mexico City[1]. The problem of finding these people in that sample can be considered as the problem of finding a rare event in a big data sample, which in this case means that the trigger "sensitivity" is about 1 to 10^7. It can be seen from this example that the act of finding them will be easier and faster, or ultimately only possible to perform if further information about them is known. At the LHC, it is expected that a Standard Model Higgs particle with a mass of 120 GeV decaying to two photons will have a sensitivity of 1 to 10^{13} [89].

In a trigger system, further information is usually obtained through the introduction of various "trigger levels" which are aimed to reduce the number of choices available. Different trigger levels arise when the information is not all available at the same time. If two different pieces of information are available at the same time, we apply them together.

In practise, the acquisition of further information that improves the selection process is limited by different factors that produce, for example, "dead-time" periods which illustrate that there are times when no data can be taken. In the example, if it turned out that they can be found at an area of archaeological interest, one will

---

[1] This is an adaption of the example given in reference [90].

avoid the hours when that place is shut. Hence, a trigger system must be provided with relatively sophisticated methods and algorithms to not only select or find rare events but also to increase the number of “good events” per time unit. Special care must be taken with the events that are rejected in HEP experiments, because in contrast to the offline processing of events, the events rejected at the trigger level are lost forever.

Therefore, a trigger system in high energy physics experiments is responsible of making an on-line selection of the particle collisions in a way that the events selected contain interesting physics processes. Moreover, the efficiency of these selections should be high in order to avoid spurious events that will bias the physics. Additionally, the rejection of unwanted processes has to be taken into account, which in most cases come from physics processes that are not interesting and that often have a higher rate than the wanted events.

The time between when a collision occurs and when a piece of information is delivered to the trigger system (called the trigger latency) can differ significantly from one detector to another. For this reason, *trigger signals* with similar latencies are grouped together in trigger “levels”, which allow events not satisfying all the trigger conditions to be rejected as early as possible, thus reducing the system dead time.

4.2 Introduction to the ALICE trigger system

4.2.1 Key features

As in the other ALICE sub-detectors and systems, the ALICE trigger system has been designed based on the unprecedented charged-particle density that are expected in nucleus-nucleus collisions at the LHC. In particular, central Pb-Pb collisions[2]have an overall interaction rate of about 8,000 Hz for a luminosity of 10^{27} $\mathrm{cm}^{-2}\mathrm{s}^{-1}$. This is a relatively low rate compared to proton-proton interactions where the inelastic rate is about 10^5 Hz at the ALICE interaction point.

The low inelastic rate for Pb-Pb interactions and the fact that the tracking performance was studied up to $dN/d\eta \sim 8{,}000$ (which means a very large amount of data produced per event), are the two main reasons why ALICE has chosen a TPC as its main tracking detector. However, the TPC has a long drift time, which means that in order to ensure a good tracking efficiency, the ALICE trigger system has to take care of the overlapping of tracks from events that occur at times close to the triggered event. The following three points are the most important features that define the current design of this system:

- In other trigger systems is possible to make a correlation at trigger level, for example to match solid angles in different detectors. The ALICE trigger system does not provide with these "local" trigger selections, instead *trigger signals* are taken as a global characterisation of the events; only by using *trigger conditions* (based on Boolean combinations) the trigger selections are restricted. Hence, the ALICE trigger system performs only **global trigger selections** (see section 4.3.2).
- The ALICE trigger system is able to make a continuous check of the time separation of events; i.e. it is able to take into account all the interactions

---

[2] Where central refers to events with the highest charged-particle multiplicity, see chapter 1.

occurring in the detector, and it can put a veto on events that occur close in time with other interactions. This is achieved by introducing the ALICE trigger feature called **past-future protection** which ensures that tracks who do not have an adequate time separation are avoided (see section 4.3.4).

- Another factor that was taken into account in the design of the ALICE trigger system was that, although the TPC has a relatively low maximum event rate, there are some other detectors in the experiment that can record at much higher rates. There is an obvious interest to make use of these other detectors as fully as possible in order to improve the statistics for physics analysis; therefore the ALICE trigger system has implemented a feature called detector **clusters** (see section 4.3.2). A cluster is a group of detectors that read out together. This allows data to be taken in suitable detectors at higher event rates, and thus makes the acquisition of data samples for physics more efficient.

4.2.2 Comparison with other LHC experiments

The differences between the trigger system designed for ALICE and those of the ATLAS and CMS experiments arise from the different requirements that have to be handled in the ALICE experiment, the two most important of them are the need of a *trigger priority* and of the *past-future protection* feature.

- In ALICE there are some triggers that are extremely frequent and in most cases will require downscaling, however there are some other triggers that are about 10^5 times less frequent, such as high momentum muon pair triggers in proton-proton collisions. Because these events are relatively rare an “enhancement procedure” needs to be implemented. What the ALICE trigger system does is to impose a **trigger priority** to decide how to handle a given interaction. If the interaction is of the “rare” type, it will always succeed provided all the detectors required to record it are not busy. If the interaction is of the "not-rate" type, it will be inhibited if data storage becomes scarce.

- The past-future protection mentioned earlier, which is different for each detector system, is a key feature in the ALICE experiment (see section 4.3.4). Let us describe how the ATLAS and CMS experiments cope without it. First, notice that although there is a difference on luminosity between ALICE and those experiments; the detectors themselves are based on completely different technologies. In ALICE, the TPC and ITS SDD are active for long periods of time. This is the case because they are drift detectors. In ATLAS and CMS, however, the detectors are active for very short periods of time compared to the ALICE detectors because for them interactions occur every 25 ns (BC period). Therefore, the "protection" that is carried out in ATLAS and CMS is achieved through the selection of detectors. However, the choice of detectors in these experiments leads to a considerably higher material budget than in ALICE.

4.3 The Central Trigger Processor (CTP)

In section 4.2 an introduction to the key features of the ALICE trigger system was given, and it was seen that the trigger system has to deal with a very complicated set of requirements both in pp and nucleus-nucleus collisions (see table 3.2 for the characteristics for different running modes in ALICE). Now a description about the Central Trigger Processor (CTP) will be presented, along with a brief presentation of the Local Trigger Unit (LTU). A more technical description of this system can be found in references [91, 92].

A subset of triggering detectors sends signals (called trigger input signals) to the CTP. For these signals the CTP has to issue output trigger signals to all the sub-detectors in order to control the detector readout. The basic features of the CTP are shown in figure 4.1. As stated in section 4.2, all the trigger signals are "global" in the sense that it is not possible in ALICE to make correlations between various sectors of the sub-detectors with the same solid angle.

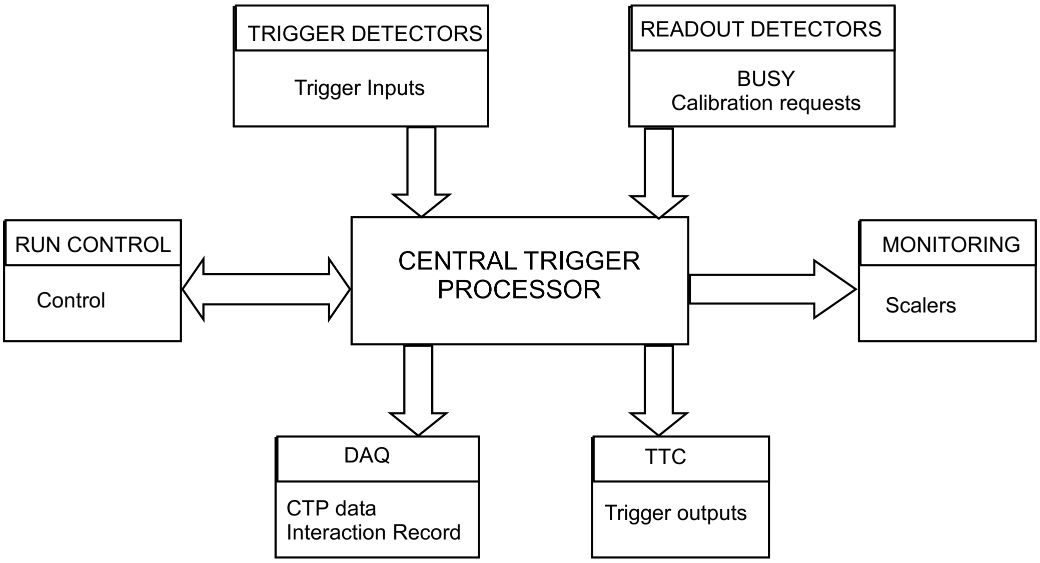

Figure 4.1: Context diagram of the ALICE Central Trigger Processor (CTP).

The very high charged-particle multiplicity in Pb-Pb interactions has governed the choice of the ALICE detectors, which significantly constrains the design of the ALICE trigger system. In particular, this means that the ALICE CTP has to cope with detector components that are busy for widely different periods following a valid trigger, and in addition it has to be optimised for several different running modes. In section 4.2 was stated that the key features in ALICE are given in terms of the use of *detector clusters* (i.e. trigger logic) and in the *past-future protection* feature. Before describing them in detail, a presentation of the trigger levels will be given.

4.3.1 Trigger levels

The ALICE system groups trigger inputs into three levels. The maximum number of trigger inputs is 60 (24 L0 inputs, 24 L1 inputs, 12 L2 inputs). Each level has a different associated latency. All detectors in ALICE receive the same sequence of triggers. The typical functions of the three trigger levels are described below.

L0 level

The L0 inputs all arrive within 800 ns of the interaction, in order to allow the L0 trigger decision to be sent to the detectors by within 1.2 μs. In contrast to the ATLAS trigger system, the ALICE experiment has separated its fast first-level trigger into two levels (L0 and L1) due to the use of non-pipelined "track and hold" electronics that requires an early strobe of 1.2 μs. The CTP itself must make a L0 decision in less than 100 ns, with the rest of the latency taken on by the generation time for the trigger input signals and by the cable delays.

The L0 level has a short latency since it initiates BUSY for all detectors in an affected detector cluster. This early strobe is sent to fast electronic detectors. In the case of Pb-Pb collision, the L0 trigger inputs are currently given by the following detectors (as described in chapter 3): Dimuon, T0, PHOS, ZDC, EMCal, ACORDE, V0, and TRD. In the case of pp collisions, the L0 trigger inputs are currently given by the Dimuon, T0, PHOS, EMCal, ACORDE, TOF, V0, TRD and SPD detectors.

L1 level

The L1 level is also a "fast" level trigger that picks up all the remaining fast inputs. The trigger signal L1 arrives at the detector 6.5 μs after the interaction takes place. Because this level allows all the existing trigger inputs to be available, a large rate reduction can be made. L1 inputs all arrive before 6.1 μs, so as to allow a trigger decision to reach the detectors by 6.5 μs.

The current list of L1 trigger inputs for Pb-Pb and pp collisions is given by the PHOS, TOF, TRD, ZDC and EMCal detectors. These fast triggers, both the L0 and L1 levels, have a direct impact on the physics outcomes of the data produced by the experiment since in these levels the first stages of physics selections are carried out.

L2 level

L2 inputs, if present, would be required to arrive by 88.7 μs, in order to allow a trigger decision to reach sub-detectors by 88 μs. This level is the final level of the trigger and it waits for the end of the past-future protection interval (88 μs, due to the TPC sensitive period from the time of an interaction) to verify that the event can be taken, i.e. the level 2 determines whether the event should be rejected because of pile-up issues after the outcome from the past-future protection is known (though the past-future protection is also checked at every level).

4.3.2 Trigger inputs

Trigger inputs are pulses provided by the trigger detectors, which are synchronised to the LHC clock cycle (TTC system) [93]. The TTC partition transmits the LHC bunch crossing clock and sends trigger signals and trigger messages to sub-detectors. Trigger inputs are sent as LVDS signals, and are aligned in time by delays in the CTP input circuit. In other words, because trigger inputs are generated in time with the LHC clock, then the CTP can treat aligned signals at the rate of one per bunch crossing (BC).

There is a uniform interface between the CTP and the detectors, i.e. each detector, when triggered, receives exactly the same set of signals. These are:

- **L0 pulse**: sent by LVDS, or, optionally, by TTC. This signal is sent 900 ns after the interaction, so as to arrive at the latest 1.2 μs after the interaction. It acts as a fast strobe, and is used to prompt detectors to send their BUSY status.
- **L1 pulse**: set by the TTC system. This signal is sent 6.5 μs after the interaction, and a fixed number of bunch-crossing (BC) after L0. If it fails to appear in the precise BC in which it is expected, the detector interprets this as "no L1". Further trigger conditions are applied, so in general there is a rate reduction between L0 and L1.
- **L1 message**: The TTC system is also capable of transmitting data after each L1 trigger words of data are transferred to the detectors. The L1 message can be suppressed.
- **L2a message**: After approximately 88 μs, i.e. the expiry of the past-future protection period (see below), the L2a message is sent to the detector. It serves a dual role in indicating that the the trigger sequence has been completed and in transmitting a certain number of words of data. These contain

  - orbit number and bunch crossing number
  - final list of active trigger classes.

- **L2r word**: If the L2 trigger is unsuccessful, a specific message must be sent. This is because, owing to the priority structure in the TTC, the timing of the L2 message cannot be guaranteed. A higher priority message, such as L1 trigger or orbit reset, might displace and delay it. For this reason the absence of a L2a message at the expected time does not signal an L2 failure; an L2r word, carrying no additional information, indicates that an L2 trigger has been unsuccessful.

From the considerations just described, the valid trigger sequences are:

L0 ;
L0 L1 L1m L2r ; L0 L1 L2r
L0 L1 L1m L2a ; L0 L1 L2a

4.3.3 Trigger classes and clusters

There are up to 50 different trigger conditions that can be demanded at any one time. Each trigger condition is specified by demanding a particular logical condition between a set of trigger inputs. A trigger condition may include trigger inputs from all different levels. Each detector in ALICE is addressed independently by the CTP, so each detector may receive a different set of triggers. In practise, different detectors are grouped together in clusters, these being a set of detectors which read out together. Therefore, for each trigger condition an associated cluster is defined. The combination of trigger condition and trigger cluster, plus a number of other parameters (choice of past-future protection and rare trigger handling [81]) together define a trigger class, i.e. the set of conditions to be specified to register a trigger for the CTP. More than one trigger class may be selected for a given event.

The requirements for a class to be activated are based on the satisfaction of input demands in a given bunch crossing and, in addition, that none of the detectors in the allocated cluster should be BUSY. Each trigger class can be associated with one of the four past-future protection circuits. In the following subsection a description of the past-future protection feature is given. A description of the rare and non-rare trigger handling can be found in [81]. Table 4.1 gives the current list of trigger classes for pp interactions at LHC startup.

4.3.4 Past-future protection (p/f)

Motivation

As mentioned above, the ALICE trigger system can put a veto on events that occur close in time with other interactions. This is achieved by its past-future protection feature, in order to avoid pile-up in detecting events selected for readout; that is carried out taking into account the sensitive periods for each detector and the expected event multiplicity and rates.

Two different uses of the past-future protection circuit are envisaged. In Pb-Pb interactions the interaction rate (about 8 kHz) is such that the probability of more than one interaction in the sensitive period of the TPC ($\pm$ 88 μs) is sizable but not close to 1. With this interaction rate, protecting the TPC is viable. Both central (high multiplicity) and peripheral (low multiplicity) are controlled independently. Thus, for example, the p/f circuit can be set to veto more than five peripheral interactions, but only one additional central interaction.

In proton-proton collisions the interaction rate is between 100 kHz and 200 kHz. At this rate the probability of more than one interaction in the TPC is essentially

Table 4.1: List of trigger classes with trigger conditions. The symbols $\oplus$ and $\odot$ indicate OR and AND respectively.

Number	Description	Condition
1	MB1	$\mathrm{V0or} \oplus \mathrm{PIXELor} \odot \overline{\mathrm{BEAMGASor}}$
2	MB2	$\mathrm{V0or} \odot \mathrm{PIXELor} \odot \overline{\mathrm{BEAMGASor}}$
3	MB3	$\mathrm{V0and} \odot \mathrm{PIXELor} \odot \overline{\mathrm{BEAMGASor}}$
4	BG	BEAMGASor
5	BGDM	BEAMGASc
6	DMsingle	DMsingle
7	DMBeamgas	BGc $\odot$ DMsingle
8	DML	DMLikeLow
9	DMU	DMUnlikeLow
10	DMMBSingle	MB1 $\odot$ DMSingle
11	DMMBLike	MB1 $\odot$ DMLikeLow
12	DMMBUnlike	MB1 $\odot$ DMUnlikeLow
13	Photon1	MB1 $\odot$ L0PHOSMB
14	Photon2	MB1 $\odot$ L0PHOSLE
15	Photon3	MB1 $\odot$ L0PHOSHE
16	Photon4	MB1 $\odot$ L1PHOSIP

one, so there is no point in protecting against pile-up. In contrast, the probability of pile-up in the ITS (with a window of ± 10 μs) is comparable to that of pile-up in the TPC in Pb-Pb interactions. In addition, in pp interactions it is not necessary to classify events according to multiplicity, as the multiplicities are three orders of magnitude smaller than in single central Pb-Pb events. For this reason, the use of the past-future protection circuit is to check for a high pile-up threshold (say $\mathrm{N_{int}} < 40$) in the TPC time window (± 88 μs), and a low pile-up threshold (say $\mathrm{N_{int}} < 3$) in the ITS time window (± 10 μs).

Implementation

The p/f feature keeps a tally (dynamic count) of the number of triggers of up to two different types that have occurred in a moving window of variable width centred on the current event. Triggers can be tested if the tally of either of these trigger types in the moving window exceeds its present threshold. This is the basis of the past-future protection implementation. In more detail, when the L0 trigger is produced, the past-future protection is able to check the full "past" history to the end of the past-future protection window. At L1 a somewhat broader window can be checked, and at L2 the full interval can be checked (stretching from -Δt/2 to Δt/2, where Δt is the width of the past-future protection interval).

Figure 4.2 and figure 4.3 show schematically how the p/f works. In this example, we set past-future protection with a span Δt of 3 BC and a threshold of 1 plus the interaction being considered. The first interaction is OK and the second one appears also to be OK, but when another event appears shortly afterwards it is vetoed immediately, setting a past-future protection signal lasting 3 BC to prevent further interactions from being triggered (see figure 4.2). First interaction would also be vetoed, in this case with a "second look" Δ on the past-future protection after the interaction, i.e. this is looking at the previous 2Δt, where it would be again found that the past-future protection threshold has been exceeded (see figure 4.3).

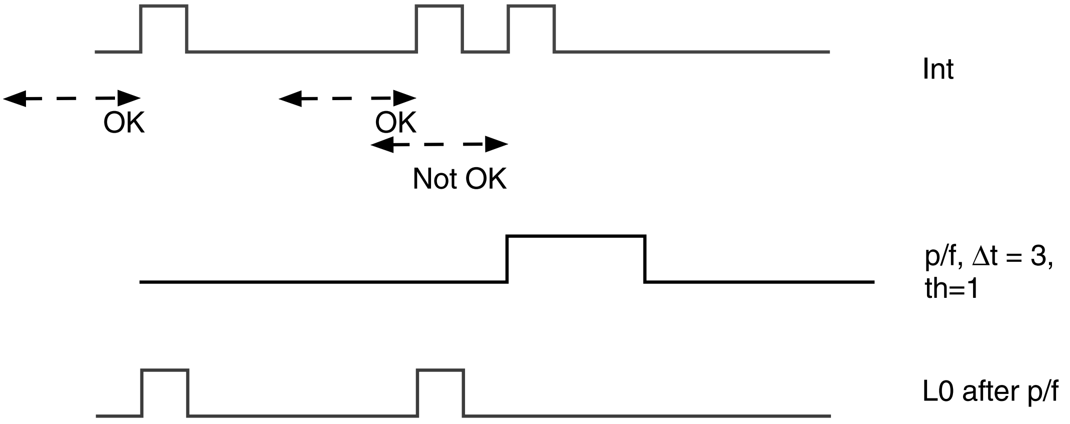

Figure 4.2: Past-future protection. Three L0 events are generated (first line), after the p/f operation (with a span of 3 BC and a threshold of 1), the last one is vetoed. Notice that the second event will also be vetoed after the next p/f interval (see figure 4.3). The first check of the past-future protection interval looks at the past at the time when the interaction happens. It can veto current events and save resources. It cannot remove events which were OK when their check occurred. Hence, a second check is at end of the past-future protection (p/f) interval, and looks back for intervals 2Δ. It can reject first event if a subsequent event renders it invalid.

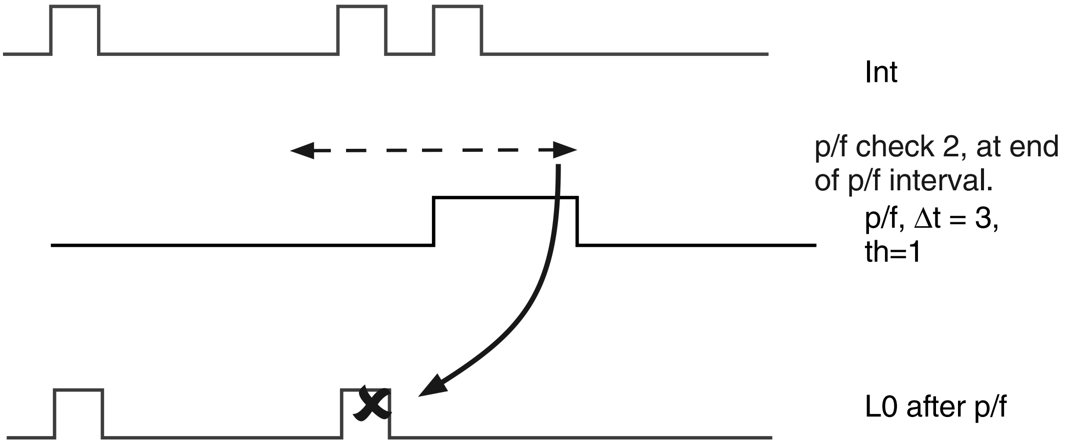

Figure 4.3: The past-future protection checks the previous $2\Delta t$ of the example given in figure 4.2, and by comparing the p/f threshold the second event is vetoed.

4.4 Local Trigger Unit (LTU)

The interface of the ALICE sub-detectors to the CTP is achieved via a VME card known as the Local Trigger Unit (LTU). The LTU serves as the interface between CTP and detectors, i.e. it produces detector specific signals (LVDS and TTC controls) which are then sent to detectors.

The LTU can also emulate all the functions provided by the CTP so as to produce a full ALICE-like environment, this including the emulation of different trigger sequences with intentional errors; and it accepts external input for use during a test beam. It can produce signals using a variety of different formats (LVDS, ECL, NIM) and is controlled by an FPGA whose contents can be changed by writing to a flash memory. In this way, different applications can be implemented simply by changing the FPGA code. The LVDS tester (see chapter 6) is an example of a non-standard configuration of the LTU board. There are 53 LTUs built, some for ALICE and some for detector groups for development work. A detailed description about the LTU in ALICE can be found in [81, 94].

Chapter 5

Synchronisation of trigger inputs in the ALICE trigger system

5.1 Synchronisation of trigger inputs

As described in chapter 4, the ALICE trigger system has 60 trigger inputs to the ALICE Central Trigger Processor (CTP). These inputs are generated at many locations and they are connected via individual cables. Their correct synchronisation with the CTP's BC clock is carried out automatically and the trigger input phase (explained below) is monitored. Although the synchronisation of trigger inputs is a topic on its own right, its description provide us with the preamble information needed to describe the results presented in chapter 6.

In ALICE CTP terms, synchronisation is a process whereby trigger input signals are adjusted (i.e. delayed) in respect to the CTP's BC clock in order to fulfil the requirements of the set-up and hold-time intervals [95], i.e. the transmitted data must be stable some time prior to the rising edge of the clock (set-up time) and some time after (hold time) to ensure its continued recognition as it propagates through the involved circuits.

The trigger inputs are “sampled” with either positive or negative edge of the CTP’s BC clock, and the synchronisation delays are within one bunch crossing (0 to 25 ns).

5.1.1 Edge flag

The synchronised trigger input circuit is shown in figure 5.1. The hardware implementation uses two D flip-flop (DFF) circuits[1]and a flag selector for the edge of the BC clock; the positive edge has a flag equal to 0, and the negative edge has a flag equal to 1. Depending on the status of such a software-controlled edge, the trigger input signal is either clocked with the BC positive edge, or it is first clocked with the negative edge and then re-clocked with the positive edge. The correct setting of the programmable edge flag is obtained from the measurement of the delay (or phase) of the trigger input in respect to the BC clock.

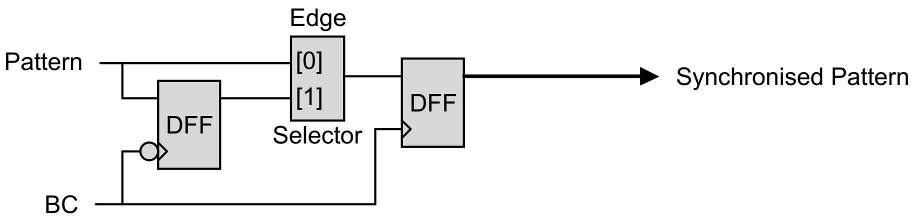

Figure 5.1: Synchronised trigger input signal (called synchronised pattern in this figure). The small triangle preceding the wedge on the D flip-flop (DFF) indicates that the default output changes take place on the positive-going clock transition. An edge flag equal to 1 will sample the trigger input with the negative edge and then re-clocked with the active positive edge.

---

[1] Remember that a D flip-flops is a sequential circuit that is insensitive to any changes in the level of the control inputs at times other than the state-changing transition of the clock signal, i.e output changes only occur on the “tick” of the clock.

5.1.2 Measurement of the trigger input phase

During the measurement of the trigger input phase, the edge flag described above is cleared, i.e. the trigger input is sampled with the positive edge. Additionally, the output of the trigger-generated sub-detectors is set to “toggle” mode, i.e. a state-changing transition of 25 ns *on* and 25 ns *off* states.

The CTP’s BC clock can be delayed in 32 steps of 1 ns each. Every time the BC clock is delayed a *delay* occurs between the trigger input and the positive-going edge of the BC clock transitions. This delay is referred to as a phase, and it is called *trigger input phase.*

Figure 5.2 shows the delay (or phase) measurement by “sampling” the trigger input (on “toggle” mode) with the positive-going BC clock transitions. L_x refers to the trigger levels sampled by the BC clock, where x can be 0,1 or 2 (i.e. L0, L1 and L2 trigger levels).

The trigger input phase is exactly the value seen by the synchronised hardware, not being affected by any other transmission delay inside the field-programmable gate array (FPGA). In order to measure such a phase, the ALICE trigger system uses an analog-to-digital converter (ADC), along with the overlap between these two signals called ΔT.

The input that is given to the ADC measurement is called *ADC input*, and it is generated by an AND function between the trigger input and the negative (or complement) value of the L_x output (see figure 5.2). As an example, the waveform shown in the bottom of figure 5.2 presents a typical *ADC input* pattern. The ADC input can be nothing, or it can be either a big or small value depending on how much overlap occurs between these two signals, as schematically shown in figure 5.3. The BC clock is also shown in this figure. Notice that the case of “perfect” coincidence and “anti-coincidence” occur when the rising edge of the BC clock coincides with

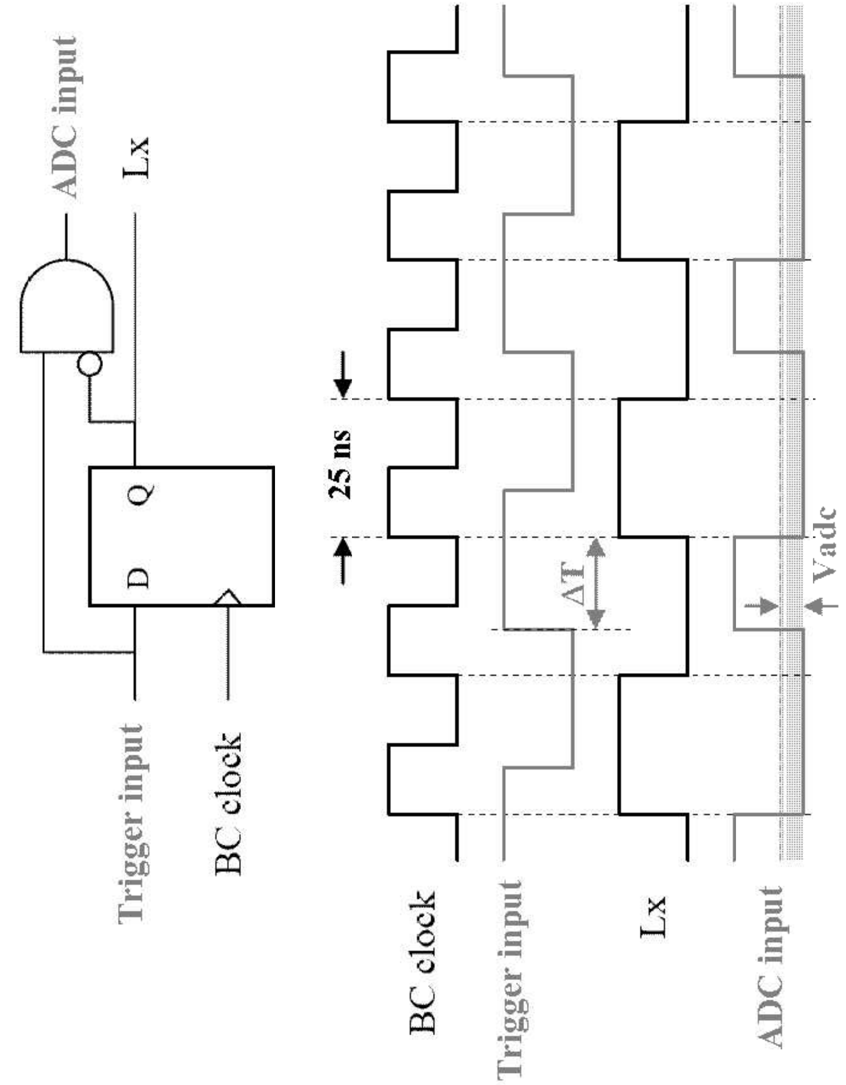

Figure 5.2: Implementation to measure the trigger input phase.

the edge of the trigger input.

What the ADC measurement provides as an output is the corresponding amplitude (V_{adc}) of the direct current (DC) voltage after a low-pass resistor-capacitor (RC) filter, as shown in figure 5.4. The corresponding DC level at the output of the filter is digitised and read by the control processor (VME). The DC level varies between the maximum value in the case of a perfect coincidence of both signals, and the minimum value when the signals do not overlap at all (anti-coincidence). Notice that because finding the overlap of the signals that are sent as a *ADC input* is what is relevant for the measurement of the *trigger input phase*, the ADC output has arbitrary units and its exact value is irrelevant. Let us now describe how the *trigger input phase* is monitored.

5.1.3 Monitoring of the trigger input phase

The monitoring of the trigger input phase can be achieved by delaying the BC clock in respect of all its possible settings (steps of 1 ns from 0 to 31 ns), while the trigger input remains “stationary”. By doing so, L_x will change in accordance with the delays of the BC clock, and consequently the *ADC input* will change too. In brief, the phase difference ΔT will change every time the BC clock is delayed. Figure 5.5 shows schematically the different ADC output readings shown in figure 5.3.

Figure 5.6 shows a typical plot of the trigger input phase measurement. This plot shows the ADC output (arbitrary units) versus the BC clock delay in nano-seconds and for the entire BC delay line. In this example of a typical measurement, it can be seen that ADC output grows linearly from zero up to 2 ns when an abrupt change occurs in the ADC reading. This abrupt change occurs when the phase shift (ΔT) goes to zero. After this transition, the ADC output grows linearly again.

(a) Perfect coincidence

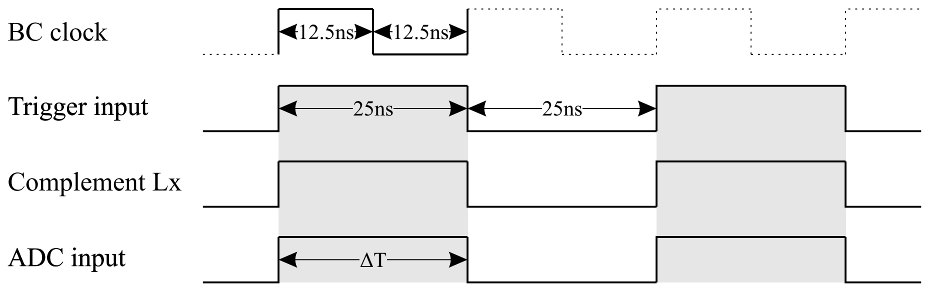

(b) Slight coincidence

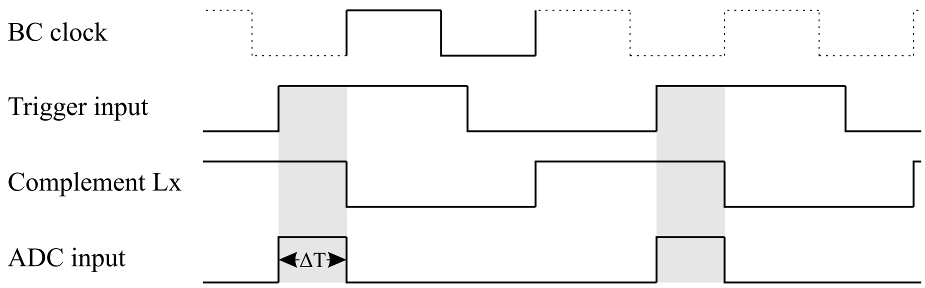

(c) Anti-coincidence

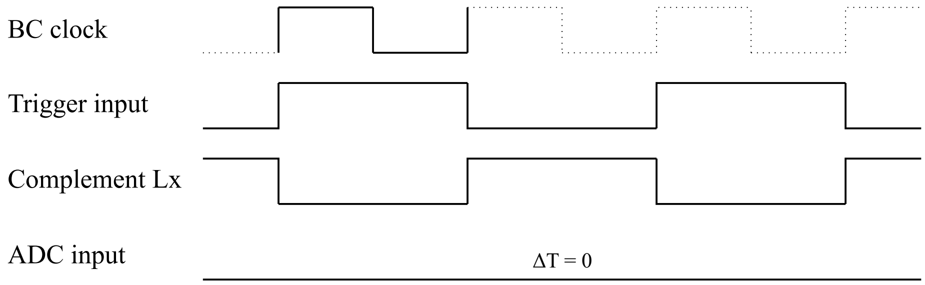

Figure 5.3: Three examples of how the *ADC input* is prepared in terms of an AND function of the trigger input and the complement value of L_x. The BC clock is also shown. One of this example (a) is when the *ADC input* is non-zero, i.e. when an overlap between these two signals is observed, called phase width ΔT. The slight coincidence case is shown in (b). The last case (c) corresponds when the anti-coincidence of these two signals occurs, leading to a zero *ADC input.* Notice that both case (a) and (c) occur when the rising edge of the BC clock “hits” the trigger input edge (see text).

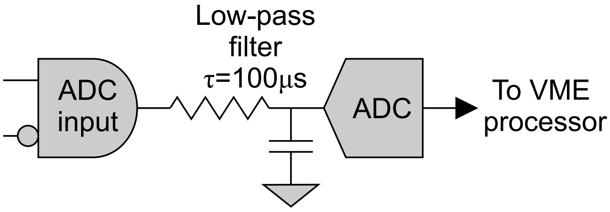

Figure 5.4: Implementation of the ADC output measurement. The ADC input (see figure 5.2) is sent to a low-pass resistor-capacitor circuit.

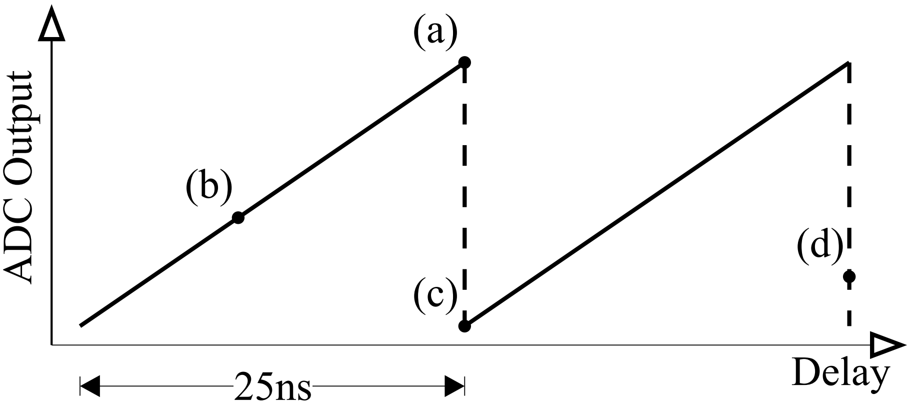

Figure 5.5: The measurement of the trigger input phase is monitored, i.e. the ADC output is studied as a function of the delay of the BC clock in ns. The (a), (b), and (c) cases described in figure 5.3 are shown. In case (a) and (c), the rising edge of the BC clock "hits" the trigger input edge leading to and ADC output reading that can be unpredictable. This means that the ADC output can also be somewhere in between (a) and (c), as shown in case (d). The case (d) is called "two phase transition".

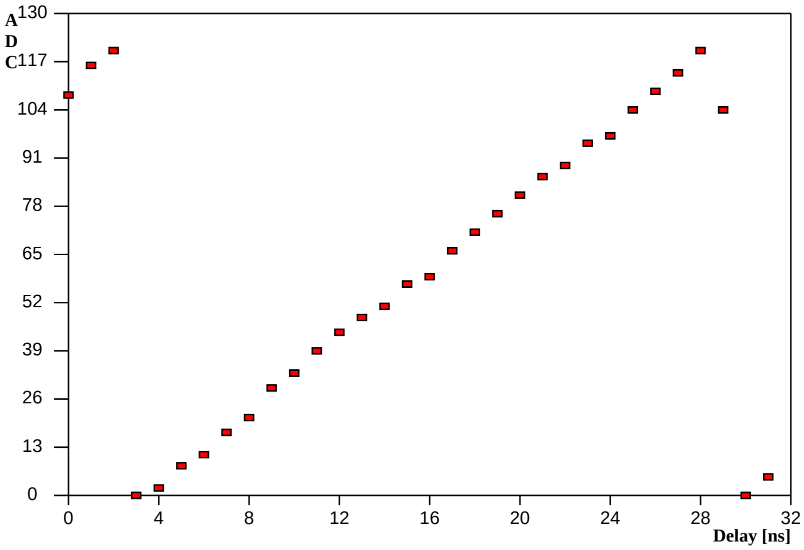

Figure 5.6: Measurement of the phase of the trigger input. The ADC measurement has arbitrary units and the phase is plotted for the entire BC clock delay line of 1 ns steps from 0 to 31 ns.

Basis of the "edge rule"

Around the region $\Delta T = 0$, the ADC reading can violate the set-up and hold-time rules as it is when the positive-edge of the BC clock transition coincides with the trigger input transition. Hence, this region must be avoided in the final setting of the BC clock delay. From here it can be seen that the ideal setting will be that "far away" from the abrupt change. The so-called "edge rule" that will be used in chapter 6, makes the ideal setting to be 12 ns away from the abrupt change. The setting can be ± 12 ns depending on the shape of the plot obtained from the phase monitoring (12 ns corresponds to about half of the 25 ns period).

5.1.4 Edge flag selection

After the BC delay is set, a correct state of the edge flag for each trigger input is obtained from the corresponding phase measurement. Figure 5.7 shows the hardware implementation for the synchronisation of trigger input signals. It includes the synchronised trigger input (called pattern in this figure) shown in figure 5.1, and the preparation to the ADC measurement shown in figure 5.2.

The final BC delay setting for the trigger input phase measurement shown in figure 5.6 can be 15 ns (12 + 3), as it is a BC delay *far* from 3 ns (or 29 ns) when the abrupt change occurs. In this case, the edge selection will be positive and the trigger input will be sampled with the positive-going (rising) edge of the CTP's BC clock.

The procedure presented here to obtain the synchronisation-settings of trigger input signals is carried out automatically by the trigger system, and it only takes a couple of seconds to be performed. Such a synchronisation-settings for the BC delay need to be repeated only after cabling changes or hardware modifications to the FPGA.

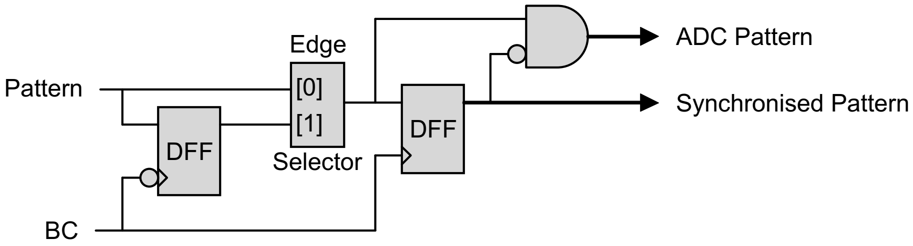

Figure 5.7: Implementation for the synchronisation of the trigger input signals (called pattern signal in this figure).

5.2 Summary

In the ALICE trigger system, trigger input signals are synchronised in respect to the CTP's BC clock so that the set-up and hold time intervals are not violated. Trigger inputs are sampled with either the positive or negative edge of the BC clock. The selection of the edge is achieved by measuring the trigger input phase, where trigger inputs are set to "toggle" mode and its overlap with the BC clock is measured via an ADC after a low-pass RC filter (integrator). The trigger input phase is also monitored as abrupt changes occurs when the positive-going (rising) edge of the BC clock transition coincides with the trigger input transitions. This value and the values around it, must be avoided in the final setting of the BC delay as it is when the set-up and hold-time intervals can be violated. After the BC delay is set, a correct state of the edge flag (either positive or negative) for each trigger input is obtained. If the edge is negative, the trigger input is sampled with the negative edge of the BC clock and then re-clocked with the positive edge. The synchronisation procedure is carried out automatically and its BC delay settings only change after cabling changes or hardware modification to the FPGA.

Chapter 6

LVDS tester: a systematic test of cable signal transmission in the ALICE experiment

Let us now present the trigger project to which the author of this thesis has contributed, particularly on the software development side. This chapter presents a systematic test of cable signal transmission based on the LVDS format. The synchronisation procedure in the ALICE trigger system is used here but its description can be found in the chapter 5. The reader might be also interested in reading the appendix B where the definitions of the timing parameters used by the ALICE Central Trigger Processor are given.

6.1 Motivation

In the ALICE experiment, the LVDS format (Low-Voltage Differential Signalling, LVDS [96]) is used for the transmission of trigger inputs from the detectors to the Central Trigger Processor (CTP), the L0 trigger outputs from Local Trigger Unit (LTU) boards back to the detectors and the BUSY inputs from the sub-detectors to the CTP. The LVDS format was chosen because it provides fast data transfers (using copper interconnect cables), with significant advantages in terms of its speed, low power and noise control relative to other formats [97].

The standard LVDS sets the cable length at a value of 10 metres, while most of the ALICE trigger connections are in the range of 40 to 60 metres. This could lead to distortions due to the longer cable length. Fortunately, it has been demonstrated that for a typical LHC transmission rate of 40 Mbit/s, transmission distortions can be successfully compensated with passive filters known as impedance equalisers [97]. It was found that signal transmission based on LVDS formats provides a low error transmission rate over distances of 100 metres and above, using passive filters [98, 99, 100]. However, despite these promising results found both in ALICE and in other experiments, a more systematic test still needs to be carried out to verify the quality of signal transmission.

These tests are normally carried out by measuring the bit-error rate (BER). For this purpose, ALICE has designed a developed set-up, called the LVDS transmission tester, that aims to measure various transmission quality parameters for long period runs in an automatic way.

In order to make the best use of such an instrument, software has been implemented in the already existing software framework of the ALICE trigger system [81, 92]. Such a software development has been carried out solely by the author of this thesis. In this chapter, the features of the LVDS tester are described, and some of the conclusions obtained from measurements are presented.

6.2 Implementation

The implementation of the LVDS tester was carried out by "converting" the standard ALICE Local Trigger Unit (LTU, see section 4.4) using a different Field-Programmable Gate Array (FPGA) firmware configuration. It turned out that the ALICE LTU contains all the required elements needed to perform transmission bit-error rate measurements. Hence, the LVDS tester configuration re-uses several applications of the LTU such as control and monitoring functions. Some of the capabilities of this board are the following:

- The LVDS board contains drivers and receivers that can be connected to the front panel connectors;
- There is a 40 MHz bunch crossing clock, and a programmable clock delay line with 31 steps of 1 ns each;
- An 8-bit analog-to-digital converter (ADC) that can measure the *input signal phase* with respect to the bunch-crossing (BC) clock (see chapter 5);
- A fast FPGA with high capacity for the implementation of the logic of the instrument.
- The VME interface enables a processor to control and monitor the measurement procedure described in section 6.3.

The LVDS tester generates data patterns which then propagates through the measured cable loop. The pattern output is simultaneously connected to three L0 connectors (as used for the LTU front panel) and each of them is driven by a differential driver. The instrument provides two identical channels that can be connected at the same time. A cable with no transmission problems can be connected in one of the channels to provide a measurement reference for another cable where errors in the signal transmission are expected to occur. The cables are connected to the front panel BUSY1/BUSY2 connectors, which are shown in the figure 6.1.

The principle of this device is depicted on the block diagram shown in figure 6.2. The description of this diagram will be given for one channel only, say *cable 1* input, as the other channel works in the same way. The first block shown in this figure corresponds to the *pattern generator*, which can generate the following output patterns:

- A sequence of a 24-bit programmable data stream transmitted repeatedly at a programmable rate;
- A random signal of programmable rate. The pulse distribution is pseudo-random as the pattern repeats itself approximately every 53 s ($2^{31} - 1$ bunch crossing); and
- A toggling output (the bunch-crossing clock divided by two) that is required for phase measurements. The toggling is, as described in chapter 5, a waveform of 25 ns on and 25 ns off.

In order to activate the *pattern generator* block, the 40 MHz bunch-crossing clock (*IN_BC*) is used. The LVDS tester delays the *IN_BC* signal by changing the *BC_DELAY_ADD* "word" as shown in figure 6.2. This delayed signal is called BC delay.

In chapter 5, the synchronisation of trigger inputs in the ALICE trigger system is described [1]. The LVDS transmission tester also borrows all the elements used for the synchronisation of trigger inputs in order to synchronise the pattern output that it generates relative to its BC clock.

---

[1] The synchronisation of trigger input signals is a topic on its own right, but it can be considered as the preamble information for the remainder of this chapter.

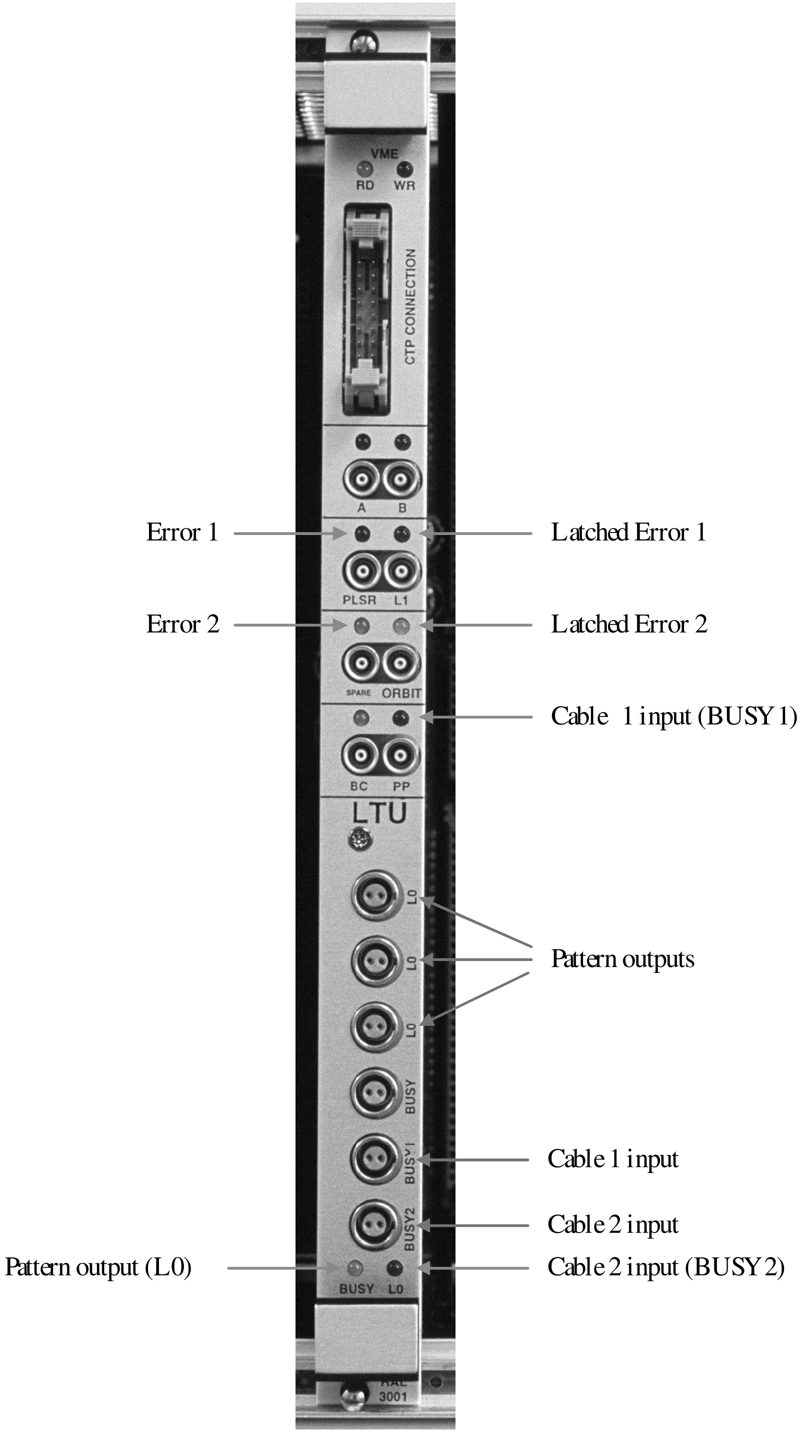

Figure 6.1: The LTU front panel, used as a LVDS tester front panel, with its LEDs and the cable connections.

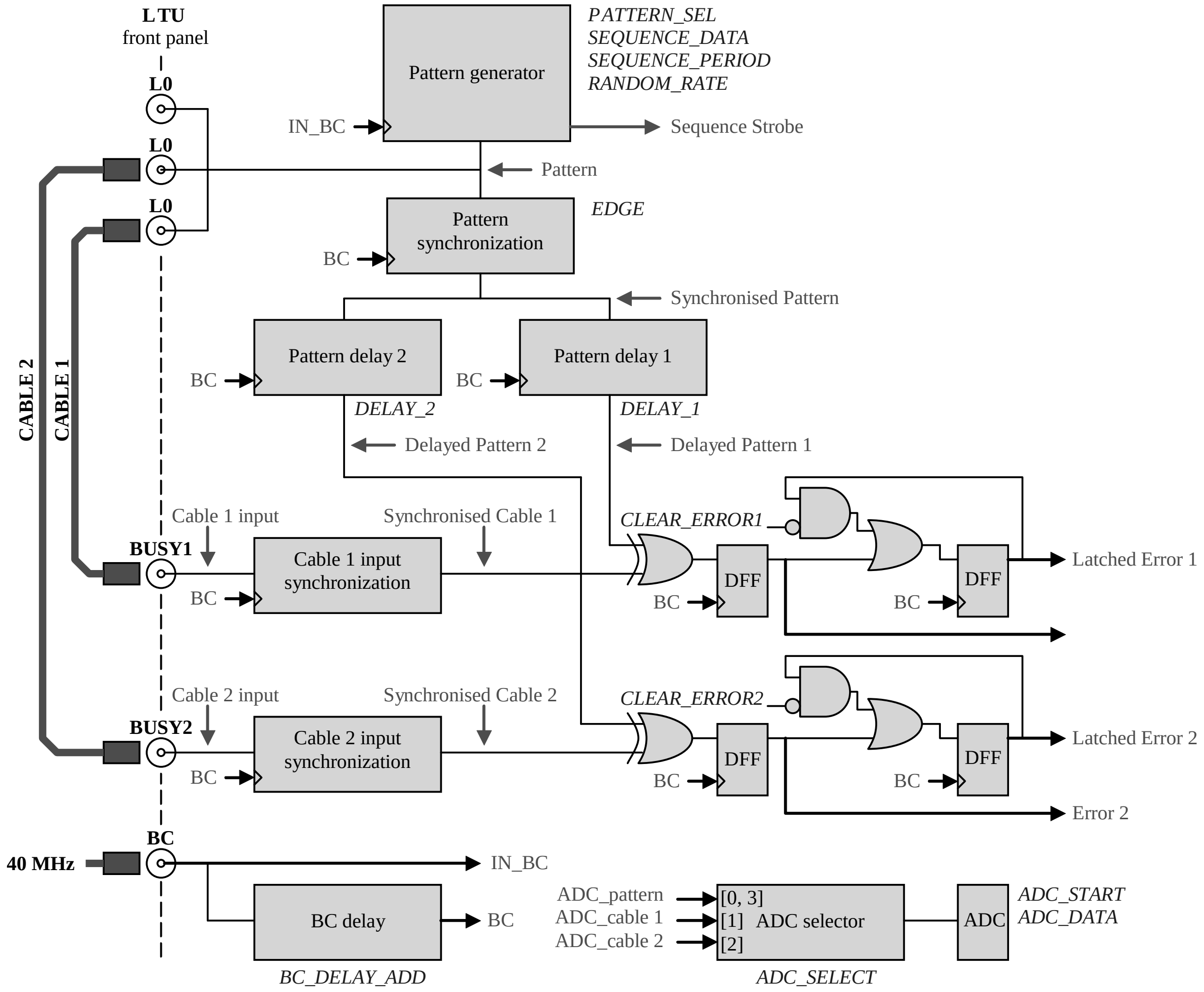

Figure 6.2: Block diagram of the LVDS tester.

In order to evaluate the quality of the pattern transmission, the *synchronised pattern* signal needs to be aligned in time with the *synchronised cable* input. Such an "alignment" procedure is achieved by delaying the *synchronised pattern* by a number of BC intervals (25 ns), as shown in figure 6.2.

In each BC clock interval, the transmitted *delayed pattern 1* is compared with the received pattern signal called *synchronised cable 1*. If their states are not the same, the corresponding error signal is asserted as shown in figure 6.2. Figure 6.3 schematically summaries the described implementation. A description of a typical measurement is given in the following section.

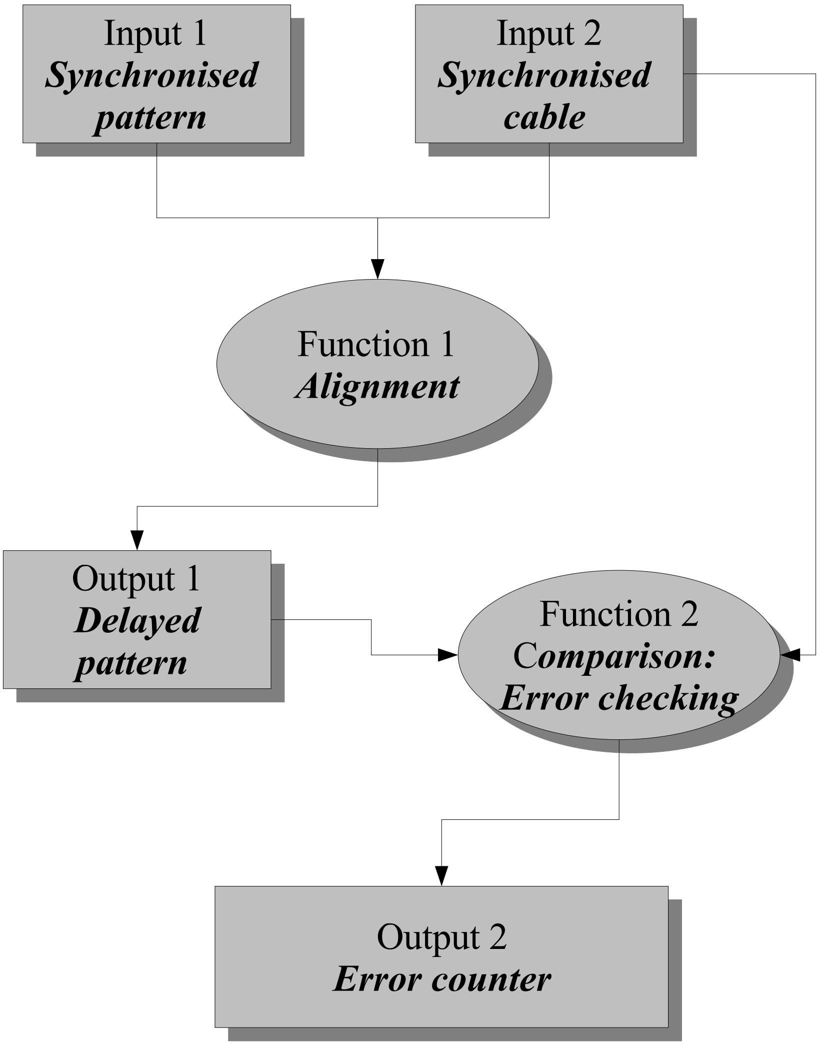

Figure 6.3: Flow chart of the implementation used by the LVDS transmission tester to align the *synchronised pattern* with the *synchronised cable* input. In each BC clock, the *delayed pattern* is compared with the *synchronised cable* (see figure 6.1 for more details).

6.3 Measurement procedure

6.3.1 Synchronisation between the generated pattern and the BC clock

The synchronisation between the generated pattern and the BC clock of the LVDS tester is carried out in exactly the same way as described in chapter 5. This measurement provide us with the BC delay value at which the transition of the *synchronised pattern* signal occurs, i.e. it determines the BC delay intervals that should be avoided due to the set-up and hold time requirements. Figure 6.4 shows, as described in chapter 5, the *pattern input phase* measurement for the entire BC delay line of 31 steps of 1 ns each. This figure shows that an abrupt change in the ADC scan (arbitrary units) occurs at 17 ns in the BC delay. This value depends only on the internal FPGA delays, and remains the same for all the boards with the same version of the LVDS tester firmware.

6.3.2 Synchronisation between the cable input and BC clock

A similar synchronisation procedure to the previous measurement is implemented between the *cable input* and the BC clock. In contrast the synchronisation between the *cable input* signal and the BC clock depends on the cable length. In other words, the BC delay interval that should be avoided in the final BC delay setting changes according to its length. Figure 6.5 shows the measurement of the *cable signal phase* for a LVDS cable of 25 metres, showing an abrupt change on the ADC reading at 11 ns in the BC delay line.

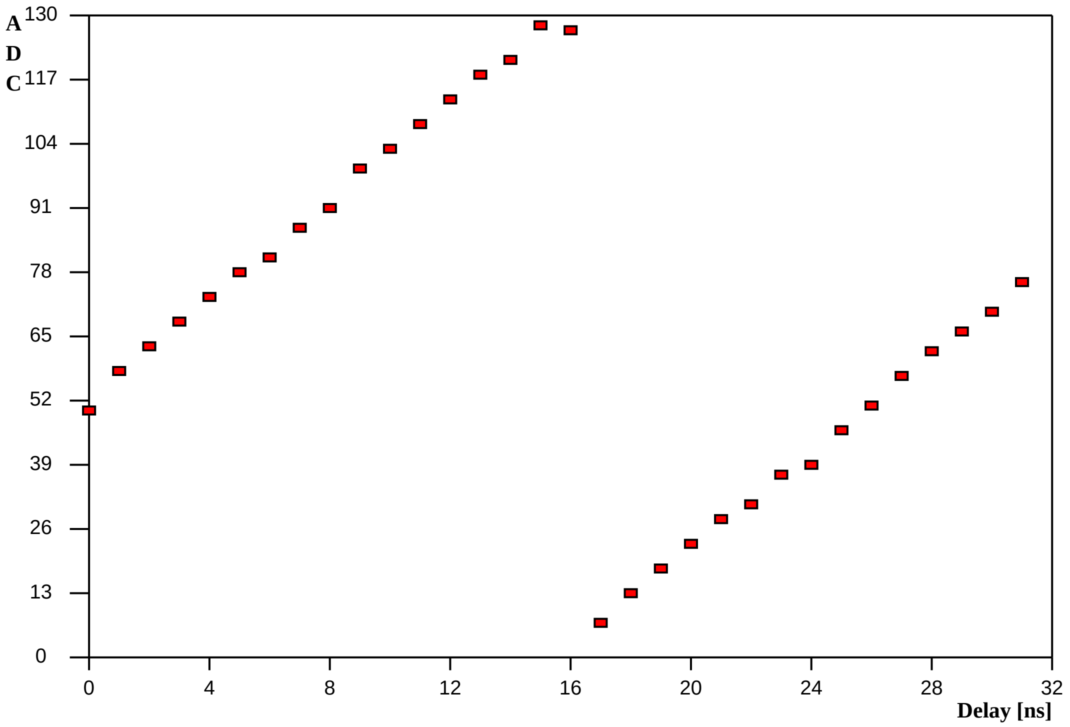

Figure 6.4: Measurement obtained from the synchronisation between the generated pattern signal and the BC clock. The measured values (ADC output in arbitrary units versus BC delay) change only after modifications on the FPGA of the LVDS tester. A more detailed explanation of this measurement is found in chapter 5

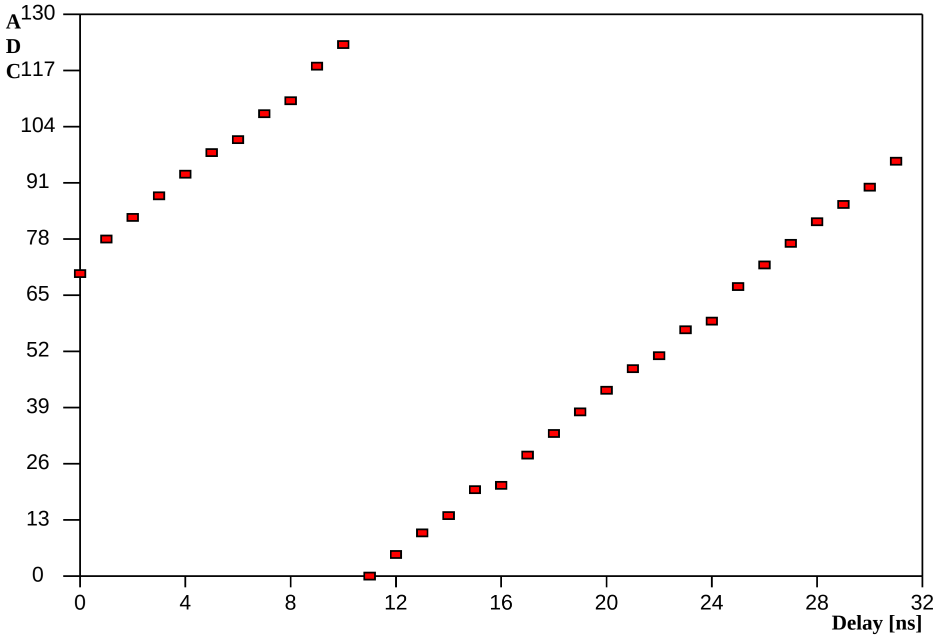

Figure 6.5: Measurement obtained from the synchronisation between the cable input signal and the BC clock for a LVDS cable of 25 metres.

6.3.3 Alignment between the synchronised pattern and the synchronised cable input

The "alignment" that is carried out between the *synchronised pattern* and the *synchronised cable* input ensures that the pattern and the version received via the cable coincide in time at the point where the data verification is performed, as shown in figure 6.1. The delay obtained in this measurement is dependant upon the length of the used cable.

In figure 6.5, the ideal setting for the BC delay, i.e. the setting value that is likely to return the least number of errors, should be *far away* from 11 ns (the abrupt change). In fact, the ideal setting will be at 23 ns, i.e. 11+12 ns (12 corresponds to about half of the 25 ns period). This means that the LVDS tester software sets the BC delay (*BC_DELAY_ADD* word) to 23 ns for this particular cable.

In addition, this ideal delay setting of 23 ns needs to be compared to the BC delay settings of the *synchronised pattern.* As described in chapter 5, the "edge selection" needs to be taken into account. The convention is that BC delay settings that are inside the BC delays interval of 17 ± 3 ns [97] (i.e. around the abrupt change) are first "sampled" with the negative edge of the BC clock. In the case of a LVDS cable of 25 metre, a BC delay at 23 ns will be sampled with the positive edge of the BC clock.

The next step consists on delaying the *synchronised pattern* for the entire pattern delay range based on bunch-crossing steps, i.e. the *DELAY_1* word shown in figure 6.1 is delayed from 0 to 31 BC in steps of 1 BC (25 ns) each. For each delay the number of errors is counted over a large number of sequences, using the error checking logic depicted in figure 6.1. The LVDS tester software normalises the number of errors on a "per sequence basis" for each pattern delay. Figure 6.6 shows the normalised number of errors versus the pattern delay (0 to 31 BC) for a cable of 60 metres. It shows that for a *delayed pattern* at 11 BC in the *DELAY_1* word, the number of errors is zero. A summary of these three measurements is given in the following section.

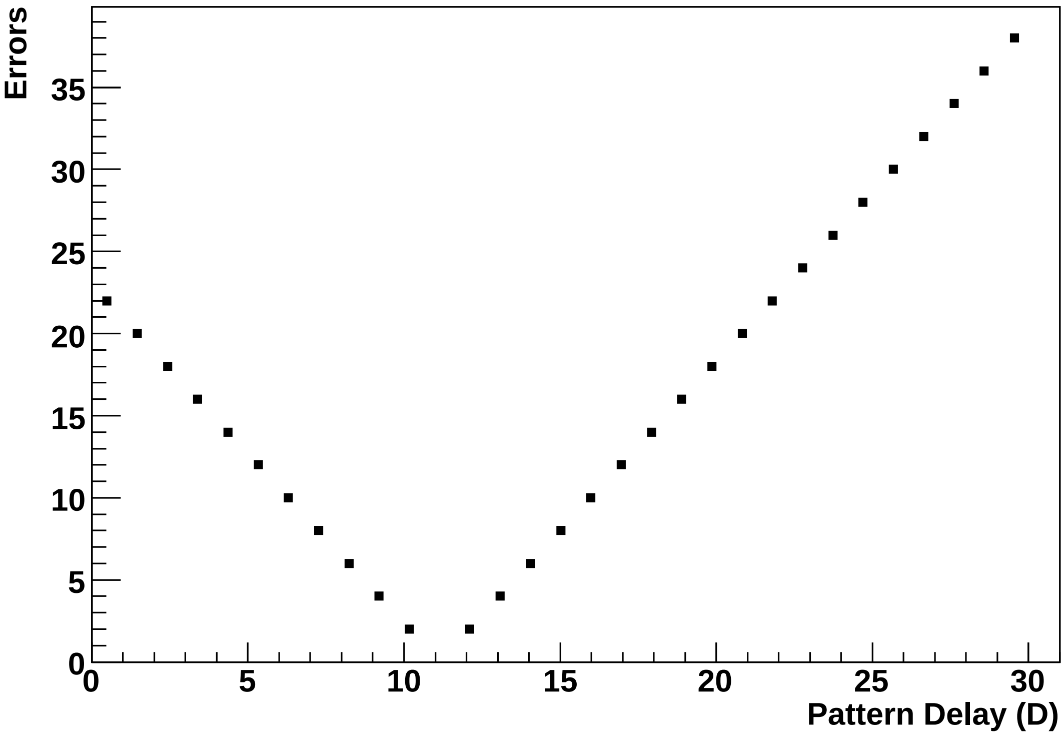

Figure 6.6: Normalised number of errors versus the *pattern delay* (BC intervals) for a LVDS cable 60 m long.

6.3.4 Preparations for measurement

The standard measurement carried out by the LVDS tester can be divided into three steps.

- *Step 1:* The synchronisation between the generated pattern and the BC clock is performed. It determines the BC delay at which the transition of the *synchronised pattern* occurs in the ADC measurement (arbitrary units) versus the

BC delay. The value obtained from this measurement is called T_p and is used for the determination of the BC edge in step 3. The delay region given by $T_p \pm$ 3 ns must be avoided in the final settings as in this region the set-up and hold time requirements can be violated.

- *Step 2:* The synchronisation between the *cable input* signal and the BC clock is performed. It determines the BC delay at which the transition of the *synchronised cable* signal occurs. The parameter obtained from this measurement depends upon the length of the used cable, and it is called T_c. The value that is likely to return the least number of errors is called T_s and it is given by $T_p = T_c \pm$ 12 ns, where the sign depends upon the shape of the phase measurement obtained from this measurement (see section 5.1.3).

- *Step 3:* The "alignment" between the *synchronised pattern* and the *synchronised cable* input is performed. The value T_s is set to be the BC delay (*BC_DELAY_ADD* word), and the edge of the BC clock is also taking into account. If T_s is inside the $T_p \pm$ 3 ns interval, the *delayed pattern* is first sampled with the negative edge of the BC clock, otherwise it is sampled with the positive one; this is called the *edge rule.* The number of errors for the entire pattern delay (*DELAY_1*) of 0 to 31 BC is obtained. For each BC delay, the *edge rule* is applied. The value obtained from this measurement is called D, and it is the only delay of the *delayed pattern* at which the number of errors is zero. Although, there might not be a delay that returns no errors, so the point with the smallest number of errors is selected by the LVDS tester software.

6.4 Bit-error rate (BER) measurements

Table 6.1 shows "transmission quality parameters" ($\mathrm{T_c}$,$\mathrm{T_s}$, and D) obtained by the LVDS tester for 10 different cable length (5 to 60 metres). The $\mathrm{T_p}$ value was also obtained by the LVDS tester but as it does not depends on the used cable, its value is always 17 ns as described in chapter 5. This table shows that for all the cable length tested an exact value for D was found, i.e. a BC delay when the *delayed pattern* does not give any errors. These measurements were obtained selecting the pseudo-random pattern in step 1 of the measurement procedure described in section 6.3. For a measurement that lasted about half an hour, these values are within the 10^9 level of accuracy (see below).

For a "realistic" bit-error rate (BER) measurement, the pseudo-random pattern should be selected in the step 1 of the measurement procedure. As mentioned earlier, the pseudo-random pattern repeats itself approximately every 53 s, which means that in order to test all the possible patterns, the error counting described in step 3 should take place during a time period of that length or multiple of it. Hence, with the clock frequency given by 40 MHz, there are approximately 2×10^9 bit transfers during the 53 s interval. This means that if N errors were counted, the corresponding bit-error rate will be approximately N divided by 2×10^9. Because the BC delay line has 31 steps, it would take approximately half an hour to complete the BER measurement for a given cable.

Notice that a measurement performed in such a way will corresponds to a "realistic" measurement because according to an accepted *rule of thumb* [97], if no error is detected at that level, the data link under test is considered reliable as the pseudo-random pattern will cover all the possible sequences that can occur. However, various tests were also carried out for a period of about 7 hours (BER at the standard 10^{12} level of accuracy).

Table 6.2 shows the measurements performed by the LVDS tester as a function of

Table 6.1: Measurement of the "transmission quality parameters" (T_c,T_s, and D) as performed by the LVDS tester for different cable length.

Cable length (m)	T_c (ns)	T_s (ns)	D (BC)
5	23	11	1
10	19	7	2
15	17	5	3
20	12	0	4
25	11	23	5
30	7	19	5
40	26	14	7
45	25	13	8
50	21	9	9
60	15	3	11

the cable length (from 5 to 100 m) for a BER at the 10^{12} level of accuracy. Because no errors were found, the BER was calculated using a 95% Poisson confidence level (CL, upper limit).

Table 6.2: Measurements performed by the LVDS tester for a BER at the 10^{12} level of accuracy as a function of the cable length using the pseudo-random pattern signal that repeat itself approximately every 53 s. Using a Poisson 95% CL (upper limit) the BER was calculated.

Length (m)	Number of errors	BER
5	0	$< 1.5 \times 10^{-12}$
10	0	$< 1.5 \times 10^{-12}$
15	0	$< 1.5 \times 10^{-12}$
20	0	$< 1.5 \times 10^{-12}$
25	0	$< 1.5 \times 10^{-12}$
30	0	$< 1.5 \times 10^{-12}$
40	0	$< 1.5 \times 10^{-12}$
45	0	$< 1.5 \times 10^{-12}$
50	0	$< 1.5 \times 10^{-12}$
60	0	$< 1.5 \times 10^{-12}$

6.5 Uncertainties on the BER measurements

In the measurement procedure described in previous sections, the “alignment” between the *synchronised pattern* and the *synchronised cable* input was performed by setting the BC delay (*BC_DELAY_ADD*) equal to T_s. Sampling the BC clock at T_s should give the least number of transmission errors for a given cable as described in section 6.3. However, one is likely to check the operation of the LVDS link at a set sampling point (BC delay) which is non-optimal and may violate the set-up and hold time requirements [2].

Therefore, in addition to the step 3 described in section 6.3, the calculation of the “uncertainties” of the BER for a given cable requires another measurement to determine the so-called “sampling window” determination where a complete scan of the BC delay (*BC_DELAY_ADD*) is carried out.

As before, the LVDS tester needs to carry out such a measurement in an automatic way, and this means the introduction of an addition “timing logic” table that deals with the automatic selection of the appropriate T_s parameter and the *DELAY_1* settings during the entire delay scan of the *BC_DELAY_ADD* word. This additional implementation turned out to be rather complicated and its technical details can be found in [97]. Essentially, the method to achieve this measurement consists on setting the *delayed pattern* (*DELAY_1*) to D ± 1 according to the different values of the BC delay (*BC_DELAY_ADD*) and observing the *edge rule*.

Contrary to what occurs in a standard measurement (i.e. when the BC delay is set to the T_s value), in the measurement of the BER uncertainties (“sampling window” determination) what matters is not the number of errors found but instead the number of consecutive BC delay bins with no error recorded; this number is called the *window* of the measurement, and for a good quality connection it should be 18

---

[2] The worst possible working margin setting occurs at $T_c = \pm 6.25$ ns (see appendix B) as it is left after the CTP trigger input synchronisation procedure.

or higher as described in [97].

Figure 6.7 shows the "uncertainties" of the BER measurement (called "sampling window") for a 60 m LVDS cable for about 2 $\times 10^9$ bit transfers. As found in the BER measurement, the delay at 15 ns (i.e. T_c) is the value with the largest number of errors. A Gaussian fit was performed to illustrate that error occurs around T_c. At the T_s value (3 ns as shown by the arrow in this plot), no error was found. This was also so between 0 to 11 ns, and between 20 to 31 ns in the BC delay line. Because the BC period is of 25 ns, this figure shows that there are only $T_s \pm$ 8 ns BC delay bins with no errors in a 60 m cable, i.e. a window of 17 was obtained.

Furthermore, a systematic test was carried out for various cable lengths in a similar way to that described above for the 60 m cable. These measurements concluded that for cables larger or equal than 60 m, impedance equalisers must be used to correct their signal transmission; i.e. the *sampling window* of these measurements was found to be larger than 18.

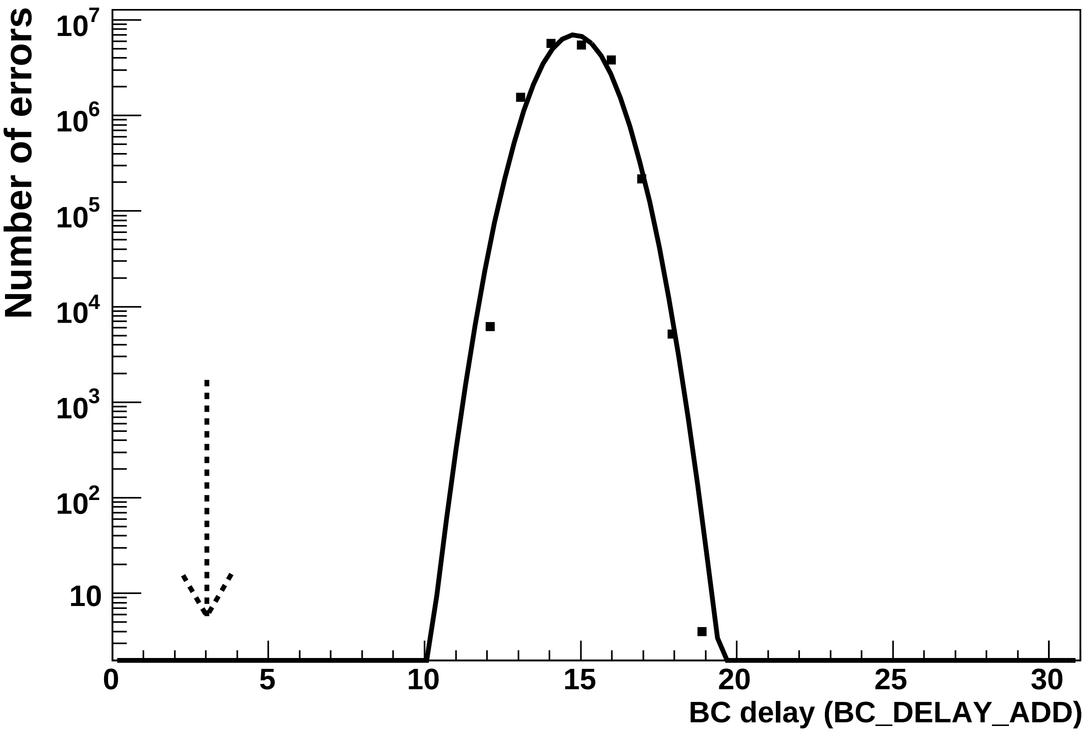

Figure 6.7: Error counting of the *delayed pattern* for the entire BC delay (*BC_DELAY_ADD*) called "sampling window". This measurement represents the "uncertainties" of the BER measurements for a LVDS cable 60 m long. The measurement was performed for about 2 $\times 10^9$ bit transfers (pseudo-random pattern), and the Gaussian fit is only used here to illustrate that the errors occurs around the T_p value of 15 ns in the BC delay. The ideal setting of the BC delay occurs at T_s (T_c - 12 = 3 ns) as indicated by the arrow. Taking into account that the BC clock period is 25 ns, the number of BC delay bins with no errors are located at $T_s \pm$ 8 ns, i.e. a *window* of 17 was obtained.

6.6 Summary and conclusions

The motivation for an instrument such as the LVDS tester was given. It is required to perform a systematic test of the LVDS cable signal transmission as a function of its length and in terms of relatively long period runs. The software that has been developed by the author allow us to calculate the bit-error rate of a given cable.

The LVDS tester measurements confirm the high quality of the ALICE standard LVDS cables. The tests have demonstrated the error-free transmission rate over the cable length of up to 60 m when the BC delay is set to its ideal value. Notice that these results were obtained even without the impedance equaliser circuit. The BER rate obtained for a cable length between 5 to 60 m is less than 1.5×10^{-12} using a 95% Poisson confidence level (upper limit).

A more sophisticated timing implementation was also developed in order to determine the “uncertainties” measurement of the obtained BER values (called “sampling window” determination). These measurements concluded that for cables equal or larger than 60 metres, an impedance equaliser must be used in order to correct the error rate of the signal transmission. The LVDS tester will allow us to prepare the development, testing and correct tuning of the impedance equaliser circuit.

Chapter 7

Prospects of lepton-pair production as a luminosity monitor at central rapidities in the ALICE experiment

This chapter is devoted to a feasibility study of the electromagnetic process $pp \rightarrow pe^+e^-p$ as a possible luminosity monitor in the ALICE experiment. Firstly, the motivations of this study are presented. Secondly, the general characteristics of lepton-pair production at the LHC are given. The aim of this analysis is to investigate and characterise the background for this process, from the minimum bias proton-proton interactions at central rapidities, in the ALICE experiment. Therefore, results based on ALICE physics performance studies are presented for pp collisions at centre of mass energy $\sqrt{s} = 14$ TeV.

7.1 Motivations and outlines

The lepton-pair process $pp \rightarrow pe^{+}e^{-}p$ is an electromagnetic process that has already been considered by other LHC experiments [101, 102, 103, 104] as a method of luminosity measurement, but so far in the forward rapidity range, where ALICE has no acceptance to measure this process. A study was needed to exploit the excellent tracking and particle identification capabilities of the ALICE experiment at mid-rapidity that were described in chapter 3, along with the already existing triggers for pp minimum bias interactions needed for such an analysis.

The ALICE detectors can identity electrons over a wide range of momentum at mid-rapidity [15]. However, for this analysis only the electrons identified by the ITS and TPC will be considered because these di-lepton pairs are typically centrally produced with low momentum (see section 7.2). In the case of the trigger requirements, a multiplicity of two-particle tracks per event in the ITS with no activity in the forward V0 detector is needed. An off-line selection condition can also be demanded by requiring “no activity” in FMD.

This chapter discusses a novel analysis to investigate the prospects of measuring this process in ALICE. Thus, the conclusions of this study are based on how many events will be needed to perform such a measurement.

7.2 Lepton-pair production at the LHC

The lepton-pair process is given by:

$$pp \rightarrow pl^+l^-p, \tag{7.1}$$

where $l = \text{e}$ or μ [105, 106]. As this is an electromagnetic process, it can be calculated using QED methods. It depends on the proton form factor, which is well known, rather than on the structure functions, which are not well known at the low values of x to be explored at the LHC. The theoretical uncertainty is about 1% [101] for the di-electron process at LHC.

Moreover, the main characteristics are the very small invariant mass of the lepton-pair, and its very small transverse momentum (see table 7.1).

Table 7.1: Characteristics of lepton-pair production via photon-photon fusion [106], where $\mathrm{M_{l^+l^-}}$ and $\mathrm{P_{t_{l^+l^-}}}$ are the mass and the transverse momentum of the di-lepton ($\mathrm{l^+l^-}$) pairs respectively.

	e^+e^- pairs	$\mu^+\mu^-$ pairs
$\mathrm{M_{l^+l^-}}$	<10-20 MeV	<M> $\sim$ 20 MeV
$\mathrm{P_{t_{l^+l^-}}}$	<10-20 MeV/c	$\sim$ 10-50 MeV/c

Figure 7.1 shows the associated diagrams for the signal and potential backgrounds of the lepton-pair production. The di-electron pairs are typically centrally produced with low momentum, and the signature in ALICE is experimentally easy to detect as only two leptons at mid-rapidity are required with no other particles.

Two possible sources of contamination for this process have been considered: re-scattering corrections (see 7.1 (b)) and proton dissociation (see 7.1 (c)). Prescriptions for taking these into account if they cannot be removed by cuts have been given in reference [106].

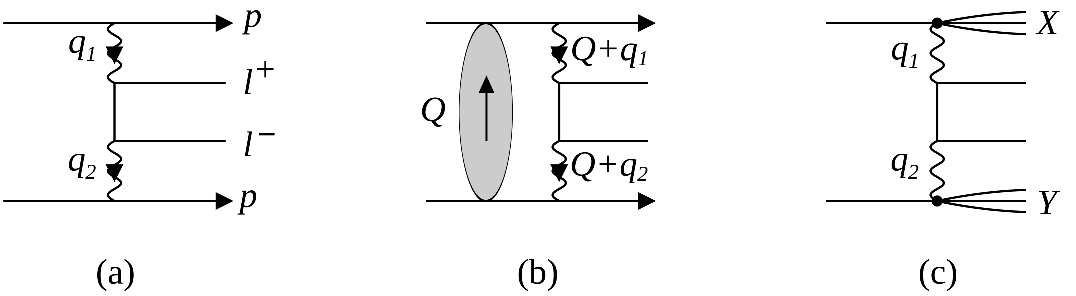

Figure 7.1: (a): Diagrams of the lepton-pair production in pp collisions, (b) a typical re-scattering correction, and (c) possible contamination coming from proton dissociation in X, Y systems [106].

7.3 Signal study of the lepton-pair (e^+e^-) process at central rapidities in the ALICE experiment

7.3.1 Generation level

The total cross-section of $pp \rightarrow ppe^+e^-$ at the LHC is 7.06 mb with a theoretical uncertainty of 1%. As in the studies carried out by other LHC experiments, the signal sample for the two-photon process was generated by the LPAIR event generator [107]. The event selection and kinematic cuts have been studied systematically already at the Tevatron and at ATLAS and CMS (see for example [102, 101, 108]). In particular, the invariant mass and transverse momentum cuts have been considered to reduce the background contributions from inelastic events; the distribution of the transverse momentum of the inelastically produced di-electron pairs (about 250 MeV/c) is relatively wider than the pairs elastically produced (about 10 MeV/c) [108]. A similar argument applies to the invariant mass distribution of the pairs. By applying cuts on both of these variables, the inelastic backgrounds were found to be below 1 %.

The acoplanarity is defined as the angular difference of two tracks from being back-to-back, when their respective tracks are projected on to the plane transverse to the beam axis [102, 108]. A cut on the acoplanarity angle has been proved to reduce the background. Table 7.2 shows the selection cuts used by this study in ALICE.

The signal sample and the cross-section calculation of this process were generated and obtained respectively by the collaboration with D. Bocian, who considered at least one of the cuts shown in 7.2. Table 7.3 shows the results for the signal cross-section, verifying that by applying the combination of all the kinematic cuts stated, the signal cross-section is 1.56 nb. However, after applying only a cut in pseudo-rapidity (cut 1) and transverse momentum (cut 2) of the charged-particles, the signal cross-section is 1.63 nb. This table also shows the number of events estimated for one normalised year (10^7 s).

In addition, although the ALICE detector has been optimised for tracking above 200 MeV/c, measurements from 100 MeV/c will also be possible (see section 3.3). Table 7.4 shows the signal cross-section in terms of the momentum range to which the electrons will be measured at mid-rapidity, indicating that a factor of two can be gained using a 100 MeV/c to 150 MeV/c cut in transverse momentum.

7.3.2 Full-simulation effects

The generated Monte Carlo sample, given by LPAIR, was passed through the AliRoot offline software framework [109] in order to obtain the detector performance effects. This means that the generated output, composed by a pair of electrons (e^+e^-) per event from the two-photon process, was sent to the transport stage that is carried out by GEANT [110] and to the reconstruction software. A total of 1,000 events were reconstructed fully for this analysis. It was found that the physical efficiency was (91.6 ± 0.6) % (see figure 7.2), and the percentage of fake tracks was (0.1 ± 0.0) %. This is including detector acceptance and reconstruction efficiency using particle identification.

Table 7.2: Selection cuts of the two-photon process analysis (generation level).

Selection cuts	Criteria
1. Production angle (Θ)	$\leq 44.25°$
2. P_t ($e^\pm$)	$\geq$ 200 MeV/c and $\leq$ 1.5 GeV
3. Pair invariant mass	$\leq$ 3.0 GeV
4. Pair transverse momentum	$\leq$ 600 MeV
5. Acoplanarity angle	$\leq 60\ °$

Table 7.3: Signal cross-section as a function of various kinematic cuts. These results were obtained at the generation level. The number of events, for the corresponding cross-section, is also shown for one normalised year (10^7 s).

Criteria	Cross-section	Number of events (1 year)
1	225.11 μb	$2.25\times10^9 \pm 4.74\times10^4$
$1 \cap 2$	1.63 nb	$1.63\times10^4 \pm 1.27\times10^2$
$1 \cap 2 \cap 3$	1.60 nb	$1.60\times10^4 \pm 1.26\times10^2$
$1 \cap 2 \cap 3 \cap 4$	1.59 nb	$1.59\times10^4 \pm 1.26\times10^2$
$1 \cap 2 \cap 3 \cap 4 \cap 5$	1.56 nb	$1.56\times10^4 \pm 1.25\times10^2$

Table 7.4: Signal cross-section as a function of the momentum range of the electrons tracks at mid-rapidity with all other cuts applied, i.e. $1 \cap 3 \cap 4 \cap 5$. These results were obtained at the generation level. The number of events, for the corresponding cross-sections, is also shown for one normalised year (10^7 s).

Momentum criteria	Cross-section	Number of events (1 year)
$\mathrm{P_t}(e^{\pm})\geq$ 100 MeV	7 nb	$7\times10^4 \pm 2.64\times10^2$
$\mathrm{P_t}(e^{\pm})\geq$ 150 MeV	3 nb	$3\times10^4 \pm 1.73\times10^2$
$\mathrm{P_t}(e^{\pm})\geq$ 200 MeV	1.56 nb	$1.56\times10^4 \pm 1.25\times10^2$

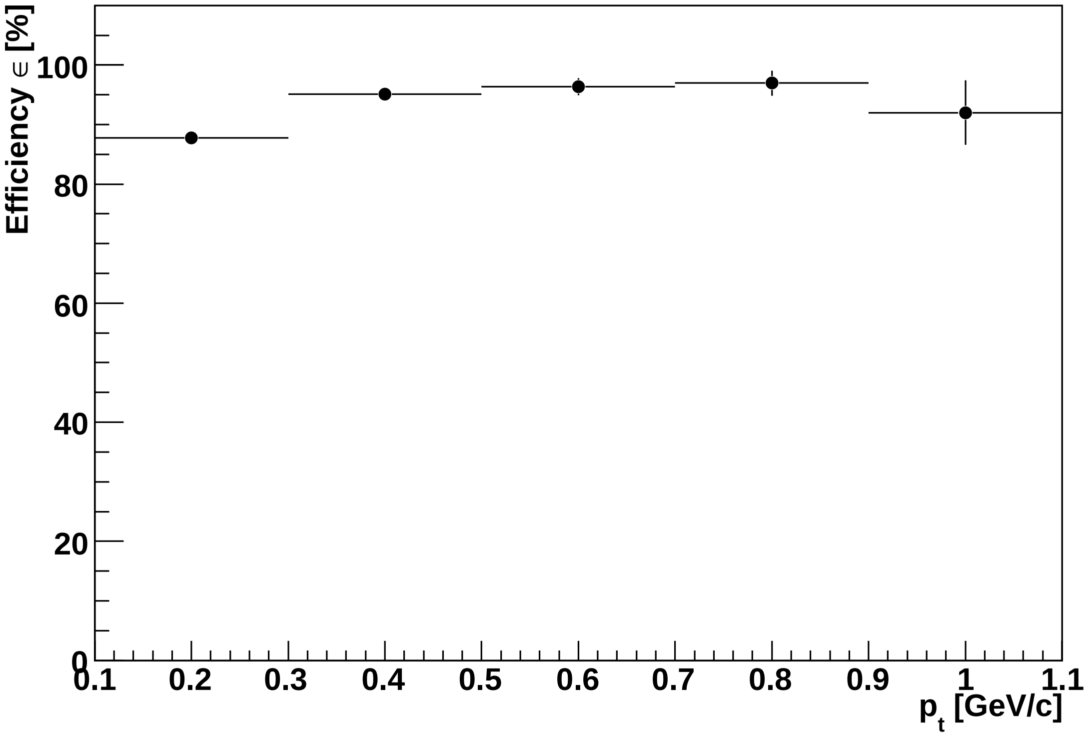

Figure 7.2: Physical efficiency of the electron tracks from the lepton-pair signal in pp collisions at $\sqrt{s} = 14$ TeV.

The particle identification efficiency in this momentum range is (68.3 ± 1.1) %, without doing any optimisation of the electron selection after the standard Bayesian approach described in section 3.3, and taking into account the information provided by the TPC particle identification only. When combining the particle ID information of the ITS along with the one given by the TPC, the overall efficiency for electron identification is greater than 70% for electrons as described in [15]. The overall contamination obtained here was about 25% from charged pions ($\pi^{\pm}$) and 6 % from charged kaons. The results and methodology used for the background study are presented in the following section.

7.4 Background study of the lepton-pair (e^+e^-) process at central rapidities in ALICE

7.4.1 Generation level

The study looks at the background of this process from the minimum bias pp interactions given by PYTHIA [111]. The events were generated by using the PYTHIA event generator 6.214 using the so-called "ATLAS tuning" parameters [112] at the highest LHC energy $\sqrt{s} = 14$ TeV. Both strong and electromagnetic decays were included in the simulation; only final-state particles were selected. The π^0 mesons generated were forced to decay at this level. These particles contribute to the background as its Dalitz decay ($e^+e^-\gamma$) has a branching ratio of $(1.198 \pm 0.032)\%$ [20].

This analysis requires no activity in the V0 detector, and two particles at the ITS mid-rapidity region. However, because no detector effects were considered at this stage, the "trigger selection" was not carried out using the standard trigger definitions, but instead the events were selected by taking into account the pseudo-rapidity ranges of the generated particles at the associated ALICE sub-detectors involved in this selection (see description of ITS and V0 detectors in chapter 3). The trigger cuts were (i) no particles at the V0 forward region and at the same time (ii) particles in the ITS region (mid-rapidity) equal to 1, 2, 3, 4 and less than 4 (i.e. low-multiplicity events).

Table 7.5 shows the estimated number of events for one normalised year of the background for 2×10^6 events as a function of the charged-particle multiplicity (μ), showing that for events with $\mu = 2$ (i.e. events with only two charged particles), the rate is of the order of 10^{-4}. This table also shows that by applying a more "tight" selection based on the proposed transverse momentum cut ($0.2 \leq P_t \leq 2.0$ GeV/c), the order of the magnitude of the production rate stays constant. This verifies that most of the events, with a very low charged-particle multiplicity at central rapidities, have particles with very low momentum.

More statistics than this was needed in order to investigate the kinematic distributions of any e^+e^- background pairs. Hence, a sample of 5×10^7 PYTHIA 6.214 minimum bias proton-proton events was generated, and a study consisting of the same selection cuts was carried out. However, it turned out that none of the samples contained any e^+e^- background pairs. Moreover, this turned out to be the same even for the "loose" condition that requires charged-particle multiplicity of $\mu \leq 4$ per event.

A study with even larger statistics will in principle be needed. Nevertheless, notice that there is not sufficient certainty in the physics output at such a level of detail using the current version of the PYTHIA Monte Carlo event generation in the predictions of the background for such process. Therefore, this study is as good as it can be obtained from a Monte Carlo study at the generation level.

7.4.2 Full-simulation effects

In order to study the background after the full detector performance effects, a sample of 2×10^6 events was used. The analysis was performed using the MC data provided by the ALICE Particle Data Challenge production during late 2006 (called PDC06 in ALICE terms). Additionally, the standard trigger definitions were used instead of simply select particles according to their associated pseudo-rapidity ranges in the sub-detectors involved (ITS and V0). Table 7.6 presents the estimated number of events for one normalised year for different logic selection of the involved physics triggers. The name of the classes used in this table follows reference [15].

As mentioned above, the proposed trigger for this process is an AND combination of the PIXELor trigger stated in chapter 4, no beam gas event and no activity in any of the two sections of the V0 forward detector. This makes the trigger selection to be $\overline{\text{V0or}} \odot \text{PIXELor} \odot \overline{\text{BEAMGASor}}$ using the name of the classes as described

Table 7.5: Estimation of the number of events for one normalised year (10^7 s) in pp minimum-bias collisions at $\sqrt{s}$ = 14 TeV, for the events that passed the selection criterion (after "trigger selection") in terms of the charged-particle multiplicity of the event (μ). These results were obtained at the generation level. The values σ_{MB} = 100 mb, and $\mathcal{L} = 10^{30}$ cm^{-2}s^{-1} were used.

Charged-particle multiplicity (μ)	Number of events (1 year)
$\mu \leq 4$	$3.97\times10^8 \pm 1.99\times10^4$
μ=4	$1.80\times10^7 \pm 4.24\times10^3$
μ=3	$5.60\times10^7 \pm 7.48\times10^3$
μ=2	$1.09\times10^8 \pm 1.05\times10^4$
μ=1	$2.14\times10^8 \pm 1.46\times10^4$
μ=2 and $0.2 \leq P_t \leq 2.0$ GeV/c	$1.03\times10^8 \pm 1.01\times10^4$

in chapter 4.

The obtained rate for the proposed trigger was 1.48×10^{-3} without demanding a particular event multiplicity of charged-particles. Figure 7.3 shows the multiplicity distribution of charged-particle tracks after requiring such trigger selection.

Moreover, the number of events (one normalised year) for this analysis was also obtained as a function of the multiplicity of charged-particle tracks (μ), and applying a transverse momentum of $0.2< p_t <1.5$ GeV/c on the charged tracks and an impact parameter cut to the primary vertex of less than 0.5 cm. Table 7.7 shows that the obtained results are of the same order of magnitude to those obtained at the generation level (as shown in table 7.5), which is consistent with a reconstruction efficiency of about 90%.

Based on the particle identification provided by the Bayesian method, this sample of fully reconstructed 2×10^6 events lacked of any e^+e^- pairs that passed any of the selection criteria used; as found in the study at the generation level based on 5×10^6 events. The MC "truth" information on these tracks also confirmed this result.

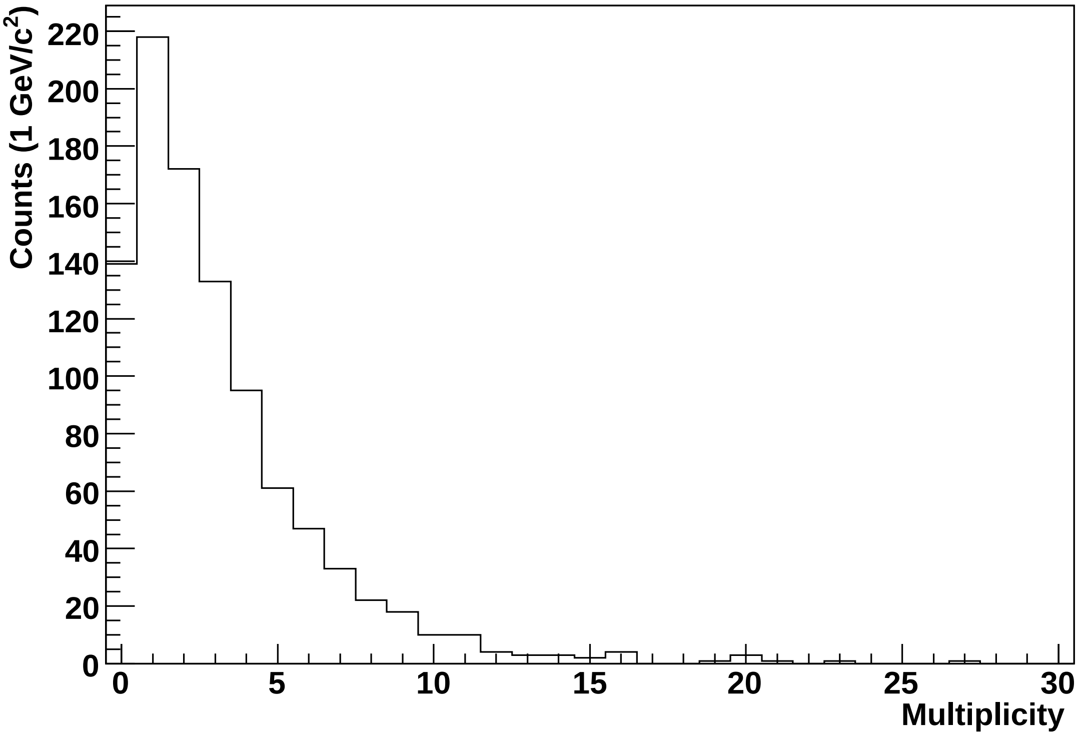

Figure 7.3: Multiplicity distribution of charged-particle tracks after requiring the global GF0 & $\overline{\mathrm{V0-BG}}$ & $\overline{\mathrm{V0or}}$ trigger used in the di-lepton pair analysis proposed as a possible luminosity monitor.

Table 7.6: Estimation of the number of events that passed the selection criterion for one normalised year (10^7 s) in pp minimum-bias collisions, as a function of different logic selection of the forward detector V0 and the global GFO trigger selection from 2×10^6 pp minimum-bias events. These results were obtained from a full-simulation analysis. The values σ_{MB} = 100 mb, and $\mathcal{L} = 10^{30}$ cm^{-2}s^{-1} were used.

Trigger condition	Number of events (1 year)
GFO	$8.91\times10^{11} \pm 9.44\times10^{5}$
GF0 & $\overline{\mathrm{V0-BG}}$	$8.89\times10^{11} \pm 9.43\times10^{5}$
GF0 & $\overline{\mathrm{V0-BG}}$ & $\overline{\mathrm{V0A}}$	$3.08\times10^{10} \pm 1.75\times10^{5}$
GF0 & $\overline{\mathrm{V0-BG}}$ & $\overline{\mathrm{V0A\&V0C}}$	$6.00\times10^{10} \pm 2.45\times10^{5}$
GF0 & $\overline{\mathrm{V0-BG}}$ & $\overline{\mathrm{V0or}}$	$1.48\times10^{9} \pm 3.85\times10^{4}$

So, by taking a limit at 95% Poisson confidence level (upper limit), we estimate the number of events in one normalised year in pp collisions (10^7s), allowing us to obtain an upper limit for the signal-to-background ratio (see next section).

Table 7.7: Estimated number of events as a function of the charged-particle multiplicity in the event for one normalised year (10^7s) in pp minimum-bias interactions at $\sqrt{s}$ = 14 TeV, and for the events that passed the GF0 & $\overline{\text{V0}-\text{BG}}$ & $\overline{\text{V0or}}$ trigger selection proposed for the lepton-pair process. The following cuts were used: 0.2< p_t <1.5 GeV/c, impact parameter b<0.5 cm, and for particle tracks at mid-rapidity. These results are based on 2 $\times 10^6$ pp minimum-bias events, and it correspond to a full-simulation analysis. The values σ_{MB} = 100 mb, and $\mathcal{L} = 10^{30}$ cm^{-2}s^{-1} were used.

Charged-track multiplicity (μ)	Number of events (1 year)
$\mu \leq 10$	$1.48\times10^9 \pm 3.85\times10^4$
$\mu \leq 4$	$1.48\times10^9 \pm 3.84\times10^4$
μ=4	$1.69\times10^7 \pm 4.11\times10^3$
μ=2	$1.61\times10^8 \pm 1.27\times10^4$

7.5 Summary and conclusions

A novel analysis based on the electromagnetic process $pp \rightarrow pe^+e^-p$ was given. The results presented show evidence that ALICE will be able to reconstruct the lepton-pair signal by identifying its decay products. It turns out that in all of the samples analysed, an absence of background candidate, e^+e^- pairs, was found. This was also the case even for the proposed “loose” condition. An estimation of the background (upper limit) was carried out using a 95% Poisson confidence level for one normalised year in pp minimum-bias collisions (see table 7.8). It indicates that the signal-to-background ratio (S/B) > 0.26 at 95 % CL. The values $\sigma_{MB} = 100$ mb, and $\mathcal{L} = 10^{30}$ cm^{-2}s^{-1} were used in the estimation of the background.

Table 7.8: Estimation of the signal, background (upper limit), and S/B values (upper limit) of the di-lepton (e^+e^-) process study, using a 95% Poisson confidence level, for one normalised year in pp minimum-bias collisions (10^7s).

Signal	Background (upper limit)	S/B
$1.56\times10^4 \pm 1.25\times10^2$	$6.00\times10^4 \pm 2.45 \times10^2$	> 0.26 at 95% CL

The results presented in this chapter allow one to recommend to the ALICE collaboration the use of this trigger to carry out the analysis in question during the first year of data taking. Further studies will be needed as described in the next section.

7.6 Outline of future directions

The following extensions to this analysis should be taken into account. From this analysis we have learnt that the current study is as good as it can be for a Monte Carlo study. Hence, the next step is to carry out this analysis using the first data to be collected for pp collisions before the end of 2008.

In particular, it will be necessary to study low-multiplicity pions and compare them with Monte Carlo studies. This will indicate how reliable is the predictions and extrapolations of the currently available MC methods for low-momentum particles at LHC energies at low-multiplicity and central rapidities. This has not been investigated in detail so far.

Notice that despite the absence of e^+e^- pairs in the proposed analysis selection, various $\pi^+\pi^-$ background pairs were found. Figure 7.4 shows the invariant mass distribution of the $\pi^+\pi^-$ background pairs obtained in the "loose" condition mentioned earlier. This figure shows the ρ^0 meson among other resonances.

If a similar conclusion for low-multiplicity pions, based on real data, is obtained to the one given in the present study, i.e. if the trigger rate is sustainable within ALICE, the next step will be to carry out pion and electron particle ID for low-multiplicity tracks at low transverse momentum, which has not been investigated yet.

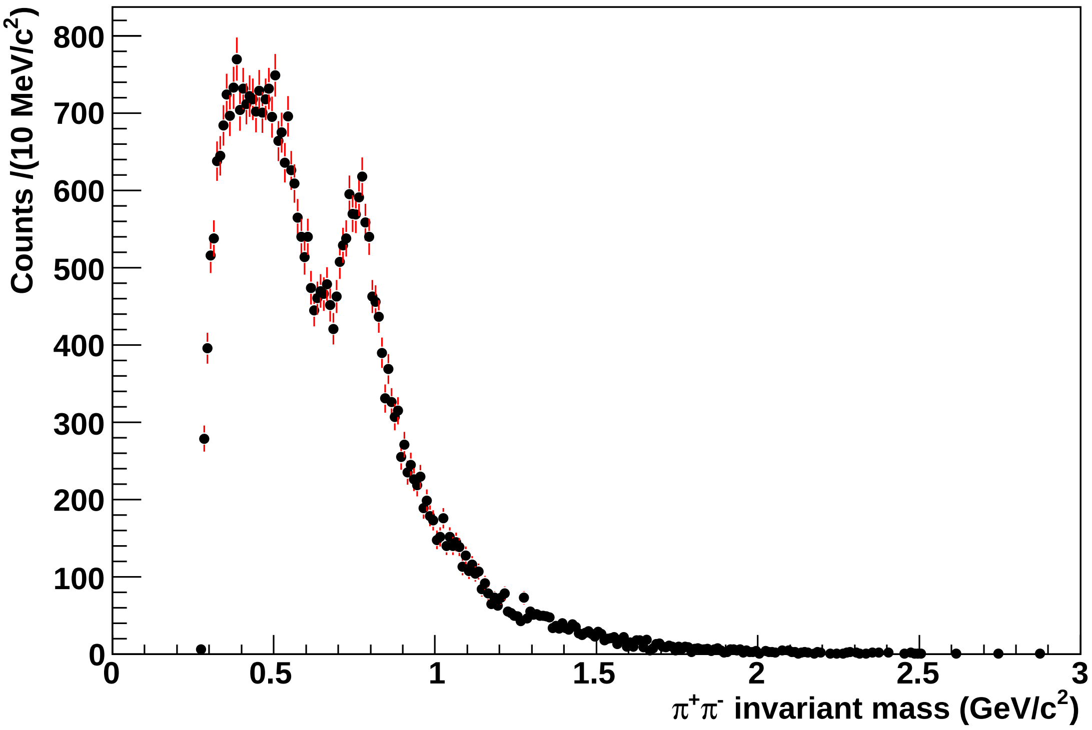

Figure 7.4: Invariant mass distribution of $\pi^+\pi^-$ background pairs from 50×10^6 pp minimum-bias (mb) events after applying the "loose" analysis criteria (charged-track multiplicity of $\mu \leq 4$ at mid-rapidity). This figure was obtained from the study at the generation level of the potential backgroun in the di-lepton process study.

Chapter 8

$\phi(1020)$ meson production: an experimental survey

This chapter gives a general overview of resonance production in high energy physics. In particular, it describes the current understanding of the properties of ϕ meson production, along with the physics motivation for studying it at the LHC. The capability of the ALICE experiment for reconstructing the ϕ resonance is discussed in chapter 9.

8.1 Introduction to resonance production

The properties of resonant states (mass, width, isospin, decay modes, spin, parity, etc.), and their production mechanisms have been the subject of study in fundamental particle physics since the 1950s [17, 113]. The first resonance was discovered in 1952 [114], and later became known as the $\Delta(1232)$. These particles decay by the strong interaction, and have extremely small lifetimes, typically around 10^{-23} s. In recent years, various resonances have been observed and studied in ultra-relativistic heavy ion collisions. It is believed that these particles can provide information about different stages of the evolution of the system, and may help to understand the transition from ordinary matter to the QGP phase.

Because the resonances lifetime is comparable to that of the fireball itself (see section 1.3), it is believed that during the expansion of the hot and dense matter produced in a heavy ion collision, a fraction of the resonances produced may decay inside such a fireball. This means that, for most resonances[1], information about the later stages of the evolution of the system can be obtained.

In addition, owing to the typically large re-scattering cross-sections presented in a high energy density medium, the hadronic decays of resonances are expected to be strongly affected by final-state interactions. This suggests that the measured yield of resonances would be different to those obtained by a thermal analysis (see section 2.3.2). This has been indeed observed at RHIC energies for short-lived resonances when comparing various particle ratios at STAR with the predicted values for Au-Au collisions [115, 116]. The predictions for some ratios of resonances to stable particles at LHC energies are given in table 8.1 [15].

---

[1] This is excluding the ϕ meson because, as discussed later, the lifetime of the ϕ in a vacuum is larger than that expected for a QGP state.

Table 8.1: Resonance to stable particle ratios in Pb–Pb collisions at freeze-out conditions expected at the LHC with $T = (161 \pm 4)$ MeV and $\mu_B = 0.8^{+1.2}_{-0.6}$ MeV for the predictions based on an equilibrium model [117] (second column). For the predictions based on a non-equilibrium model [118] (third column), the calculations were obtained with $T = 162$ MeV and $\mu_B = 2.7$ MeV . These values can be found in [56].

Ratio	Eq. model	Non. eq. model
ϕ/K^-	0.137	0.13
$\Lambda(1520)/\Lambda$	0.075	0.060
$K_0^*(892)\ /\mathrm{K}^-$	0.318	0.301

8.1.1 Re-scattering and re-generation effects

It can be assumed that a fraction of the resonances may decay before kinetic freeze-out, and daughter particles from their hadronic decay might be re-scattered by other particles in the hadron gas. Hence, it is thought that a loss of the resonance signal is expected in heavy ion collisions due to re-scattering effects. At the same time, the hadronic particles in the medium can interact with each other to regenerate resonances, which may compensate part of the signal lost.

Depending on the length $\Delta\tau$ of the time interval between chemical and kinetic freeze-out defined in chapter 1 (see figure 8.1), the magnitude of the suppression of the measured resonance yield will change due to contributions from re-scattering and recombination effects.

A model [119] was recently proposed to estimate the time interval $\Delta\tau$, by using yields of thermally produced particles at chemical freeze-out and considering an additional re-scattering phase. It also includes the lifetime of the resonances and the interaction of the decay products within the expanding fireball. The relative contribution of resonance production to various particles for three freeze-out temperatures (T=140,160 and 180 MeV) is shown in figure 8.2. It seems from this figure

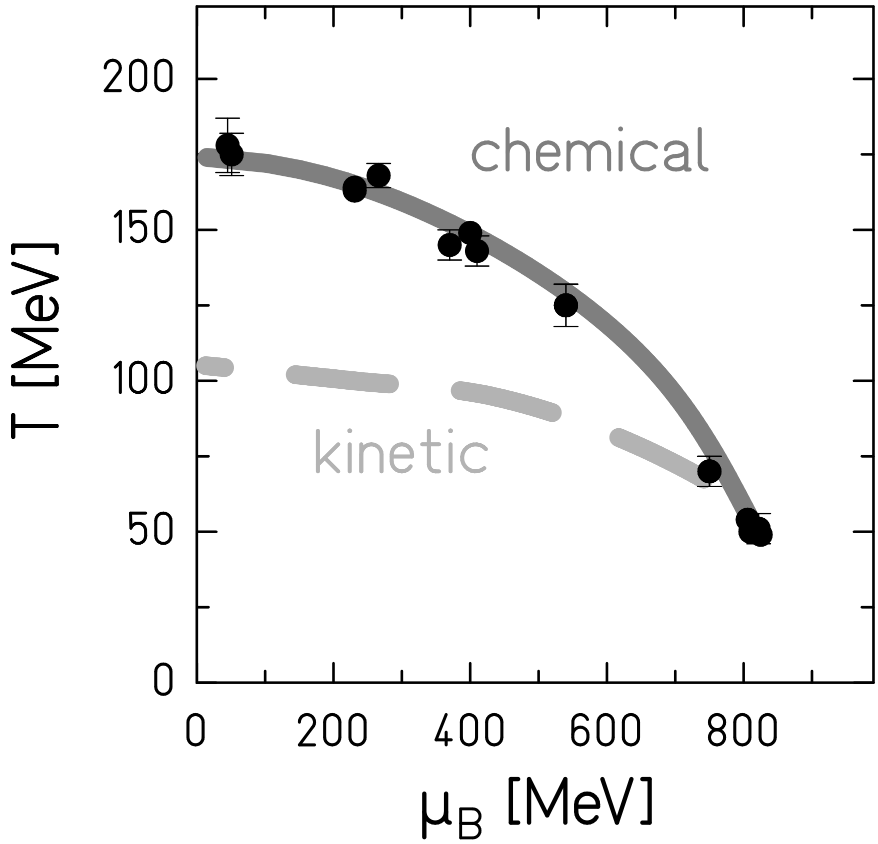

Figure 8.1: Compilation of chemical freeze out parameters at SIS, AGS, at the SPS at 40 AGeV and 160 AGeV and RHIC. The full line represent the phenomenological condition of chemical freeze out at fixed mean energy/particle $\simeq$ 1.0 GeV. The dashed line indicates the temperatures where kinetic freeze out is observed. More details about these results can be found in [15].

that the effect of freeze-out temperature T on the ϕ is much more significant than in any of the other particles. This is so because the ϕ resonances are relatively heavy, which leads to a larger variation of the resonance contribution as a function of the temperature. However, although not seen from this figure, the overall effect on the ϕ remains a small one compared to other states[2]. The mass difference between mesons and baryons also affects the relative meson to baryon ratio shown in this figure [53].

Figure 8.3 illustrates how the time interval $\Delta\tau$ between chemical and kinetic

---

[2] J. Rafelski, private communication.

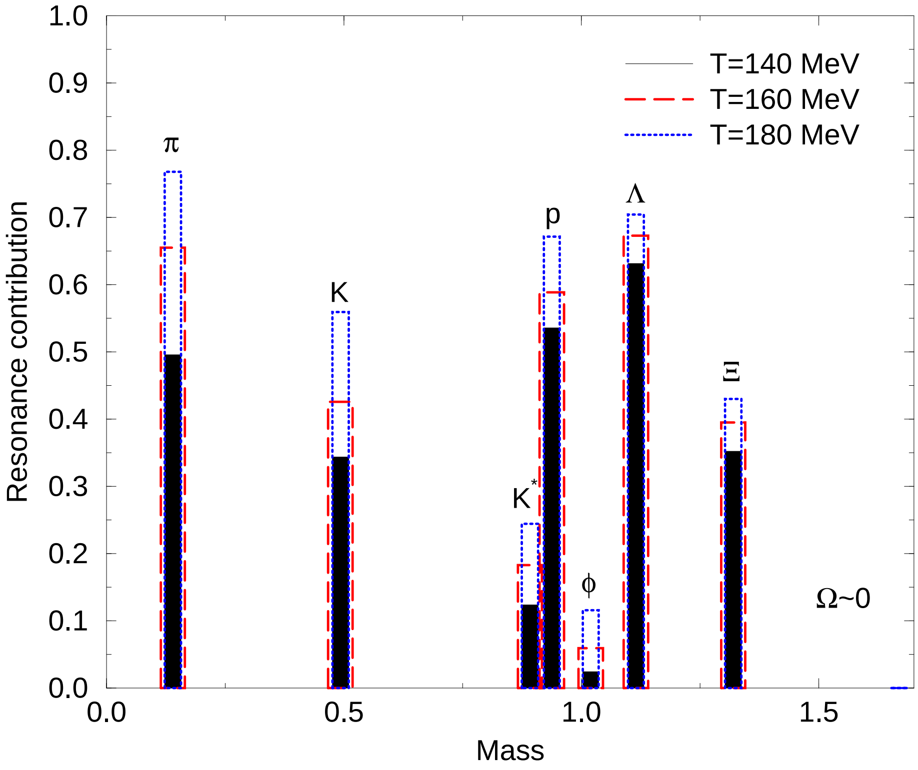

Figure 8.2: Percentage of particles (π,K, K*, p, Λ, ϕ, Ξ, Ω) that come from resonance decays. Figure shows three freeze-out temperatures of the thermal system [53].

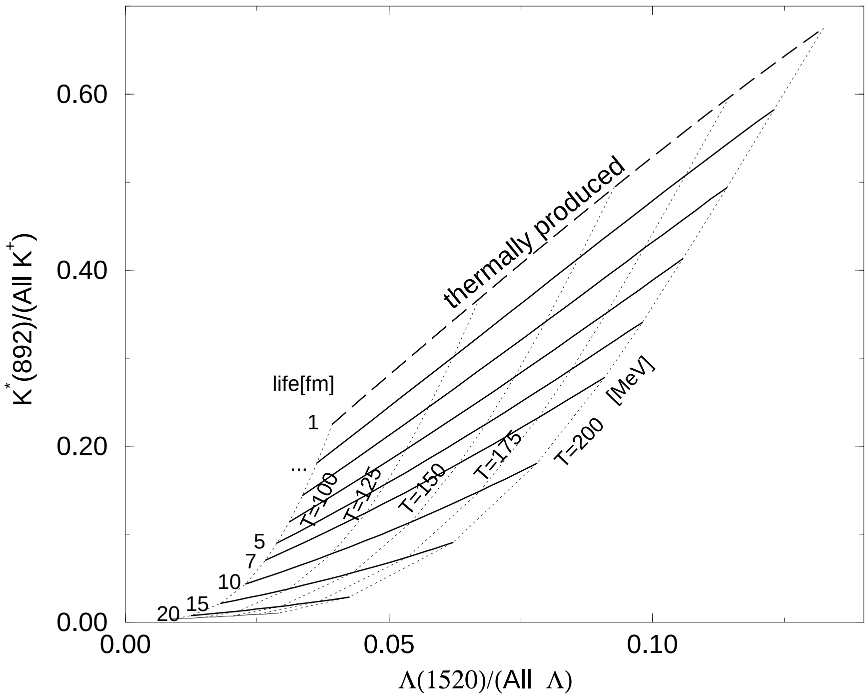

Figure 8.3: Dependence of two particle ratios, K^*/K and $\Lambda(1520)/\Lambda$, on the freeze-out temperature and the time interval between chemical and kinetic freeze out.

freeze-out can be constrained by using two measured ratios, say the K^*/K and $\Lambda(1520)/\Lambda$ ratios, where large re-scattering is expected, as shown in table 8.1. By including the decay of heavier particles, the particle ratios shown in figure 8.3 take into account the resonances produced at different stages. For example:

$$\frac{\Lambda(1520)}{\Lambda_{\mathrm{total}}} = \frac{\Lambda(1520)}{\Lambda + (\Sigma^0 \to \Lambda\gamma) + (\Sigma^* \to \Lambda\pi) + (\Sigma^* \to \Sigma^0\pi \to \Lambda\pi\gamma)} \tag{8.1}$$

Assuming a chemical freeze out at 160 MeV, a time interval $\Delta\tau > 4$ fm/c was obtained from this model [53]. Thus, if the decay products of a given resonance are subject to major re-scattering, its signal is expected to be suppressed.

8.1.2 Changes in line-shape of resonances

In addition, changes in line-shape of resonances have been predicted in heavy-ion collisions for two reasons: (*i*) the dense medium can induce significant collision broadening; (*ii*) shifts of both mass and width [23] could be produced as a result of partial chiral symmetry restoration (see section 2.1.3). Recent measurements from the STAR experiment suggest that a change in the mass and width of the K^*, Δ^{++} and ρ^0 were observed at low values of transverse momentum. However, the K^* shift, of the order of some MeV, was observed for all collision systems, including d-Au and pp, and is of the typical size observed for other particles in many experiments due to instrumental effects [120]. In addition, since discrepancies in rate production have been reported between PHENIX and STAR, more accurate measurements and further studies in resonance production are still needed [121]. In the remainder of this chapter, the motivations to study the ϕ meson will be covered as its study at LHC energies is the subject of chapter 9.

8.2 The ϕ meson at the LHC: physics motivations

The ϕ vector meson is believed to be an almost pure bound state of strange-quarks ($\phi = s\bar{s}$). It has a mass of 1,019.456 MeV/c^2, which is comparable to the proton and Λ baryon mass, and has a narrow width $\Gamma_\phi = 4.26$ MeV/c^2 $\pm$ 0.05 MeV/c^2 [17, 20]. The most prevalent decay mode for the ϕ meson is the decay into K^+K^- pairs which accounts for 49.1 % of its decays. Other decay modes into two charged particles, without multi-body kinematics, occur very rarely, as shown in table 8.2. The author has been involved with the Monte Carlo study of the di-kaon decay channel of the ϕ meson, which is the subject of chapter 9. There are physics motivations to study ϕ meson production at the LHC, both in heavy-ion and proton-proton collisions.

Table 8.2: Some of the ϕ(1020) decay modes [20]. The ALICE experiment will allow the study of the ϕ, both in the di-kaon and di-lepton decay modes, for various collision systems.

Mode	Fraction(Γ_i/Γ)
K^+K^-	(49.1$\pm$ 0.6)%
$K^0_L K^0_S$	(34.0$\pm$ 0.5)%
e^+e^-	(2.98$\pm$ 0.04)$\times$ 10^{-4}
$\mu^+\mu^-$	(2.85$\pm$ 0.19)$\times$ 10^{-4}
$\pi^+\pi^-$	(7.3$\pm$ 1.3)$\times$ 10^{-5}

8.2.1 The ϕ in heavy-ion collisions

As stated earlier, resonances, and in particular the ϕ meson, are useful probes to study the high density medium created in ultra-relativistic heavy ion collisions. Let us describe the current physics motivations behind the study of this particle, along with a brief survey of what has been learnt from other experiments. The hadronic cross-section associated with the ϕ meson is small, which makes this particle rather insensitive to the presence of other hadrons in the late stage of the collision. Therefore, the production of ϕ mesons has been suggested as a signature for strangeness production mechanisms [45, 122, 123].

- Significant medium modifications of its production and decay properties have been predicted [23, 124]. As a consequence of these modifications, the branching ratio for its decay into kaon and lepton pairs may change. The observation of such modifications might also provide information on the mechanism relevant for ϕ production in high energy collisions, which at present remains an open question. For example, it has been suggested that a double-peak in the di-kaon invariant mass spectrum can be observed as a possible signature for the QGP phase [125, 126], which could be due to the non-negligible time duration of the QGP phase ($\sim$ 10 fm/c) compared to the lifetime of the ϕ in vacuum (about 45 fm/c). It is believed that the mass of ϕ mesons decaying in the mixed phase is expected to be lower than the nominal one; this as a result of the partial chiral symmetry restoration (see section 2.1.3). The value of a shift in the mass invariant distribution depends on various factors such as the critical temperature, together with considerable theoretical uncertainties. Figure 8.4 shows the study that has been carried out to illustrate the capabilities of the ALICE detector to identify a double peak in the di-kaon invariant mass spectrum [127].

- Despite the non-observation of any changes in the mass and width of the ϕ meson at RHIC energies [128, 54, 129, 130][3], preliminary results from the STAR collaboration suggest that a strangeness enhancement might have been observed at RHIC energies when comparing the ϕ yields obtained in Au-Au collisions, and more recently in Cu-Cu collisions, with those obtained in pp collisions [131]. Measuring the ϕ at LHC energies will be possible in various collision systems (Pb-Pb, pp, pA), and it is expected to provide information about the strangeness content at the highest energy ever achieved (see below).

---

[3] At present, the only experimental claim of spectral property modification of ϕ mesons can be

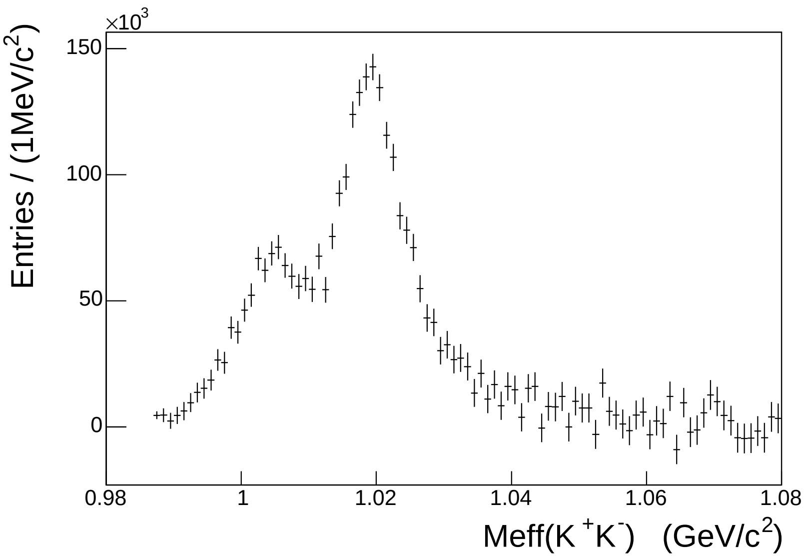

Figure 8.4: Di-kaon invariant mass distribution showing a double peak structure of the ϕ meson as carried out in a feasibility study carried out in ALICE [127]. A double-peak such as the one shown here could be interpreted as a possible QGP phase signature [125, 126].

- In the resonance leptonic decay, daughters should rarely be re-scattered by the hadronic medium since the lepton-hadron interaction cross-section is much smaller than the corresponding hadron-hadron decay channel. So, the dielectron or dimuon decays of ϕ mesons might shed light on the ϕ mesons produced earlier in the evolution of the fireball. However, various issues arise from such an analysis because of the large combinatorial background from gamma conversions and Dalitz decays, along with the low probability for the electromagnetic decays. At the CERN SPS the particle yield of the ϕ meson in both hadronic and leptonic channels was measured [134, 135, 136, 137], though thus far no clear evidence for any of the expected modifications has been observed [138]. With the unique particle identification system of ALICE described in chapter 3, the study of $\phi \to K^+K^-$ and its di-lepton counterparts $\phi \to e^+e^-$ and $\phi \to \mu^+\mu^-$ will be possible. This is expected to finally unfold the so-called "SPS puzzle" of the ϕ meson.

---

found at normal energy densities (12 GeV pA collisions), recently reported in [132, 133].

8.2.2 The ϕ in proton-proton collisions

- In order to understand heavy-ion collisions, the pp counterpart should be available. Hence, analysing resonances in pp collisions is needed as a benchmark for the heavy ion run. Additionally, the ϕ meson is an interesting particle in itself as a hadronic measurement that could be carried out at several energies and for various collision systems at the LHC. Moreover, ϕ production has not been measured to very high precision at the Tevatron [139] as shown in figure 8.5. The LHC experimental programme is currently considering to carry out a scan in energy during the early running which means that even "low energy" points from the LHC startup, of 0.9 TeV for example, would become the best data at that energy. Although the ϕ in pp interactions has been measured at RHIC, its centre of mass energy is considerably lower than that at the Tevatron.

- The ALICE experiment will play a key role in the description of the soft-physics regime in proton-proton collisions. Furthermore, ϕ meson production in pp collisions could be used as an indicator of strangeness production along with that of particles with open strangeness $(K^{\pm}, K^0, \Lambda, \Xi, \Omega)$ [140]. There are predictions that the strange sea could be large [141]. Additionally, at the LHC it would be possible to access the very low-x region, about which not much is known, which would allow HERA measurements on low-x strangeness production [142] to be compared with LHC pp results.

- The strangeness content is often given by the Wroblewski factor defined as $\lambda_s = 2\ \langle s\bar{s}\rangle/(\langle u\bar{u}\rangle +\ \langle d\bar{d}\rangle)$ [143]. The yields of hadrons from e^+e^-, pp, and p$\bar{\text{p}}$ collisions can be described by a statistical model in a canonical formulation [144], where the Wroblewski factor can be obtained as shown in figure 8.6, both for heavy-ion and elementary collisions. As shown in this figure, in pp collisions the Wroblewski factor has an almost constant value of $\lambda_s \sim 0.2$ as extracted from the data, and performing calculations based on the canonical model for μ_B=0. However, it has been demonstrated that this factor rises

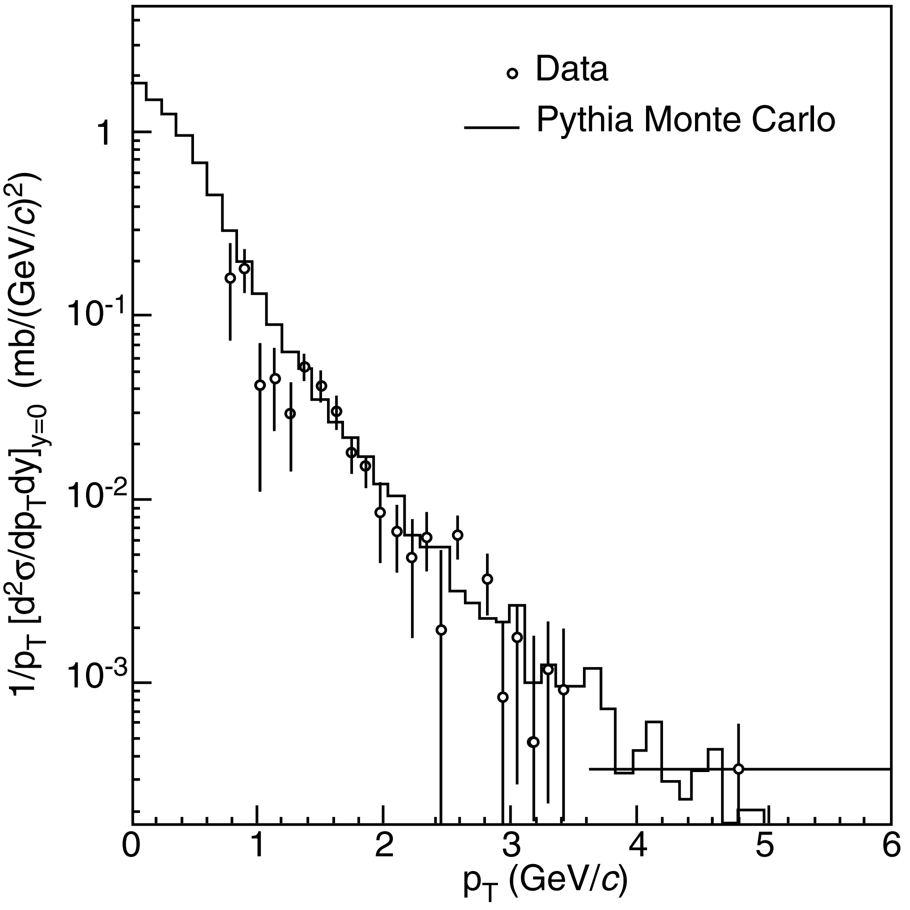

Figure 8.5: Transverse momentum distribution of ϕ mesons, after corrections, as measured at the Tevatron (p$\bar{\text{p}}$ at $\sqrt{s}$ = 1.8 TeV). The PYTHIA event generation predictions (line) was compared with the data. The study suffered from statistics as only 900 ϕ were reconstructed, not allowing the physics of ϕ meson to be explored at high-multiplicity (see text).

with increasing temperature for a given μ_B, causing the largest value in the case of heavy ion collisions because of the finite μ_B. Measuring strange particles (including hidden strangeness particles such as the ϕ and η'), will allow a better understanding of this factor and its implications in modelling the soft-physics regime. The currently available Monte Carlo event generators, such as PYTHIA [111] based on the Lund Model [145], consider such a factor as universal. The agreement of λ_s between e^+e^- and hadronic collider is reasonably consistent although not perfect. At the high energies available at the LHC, a final conclusion on the universality of these values can be drawn.

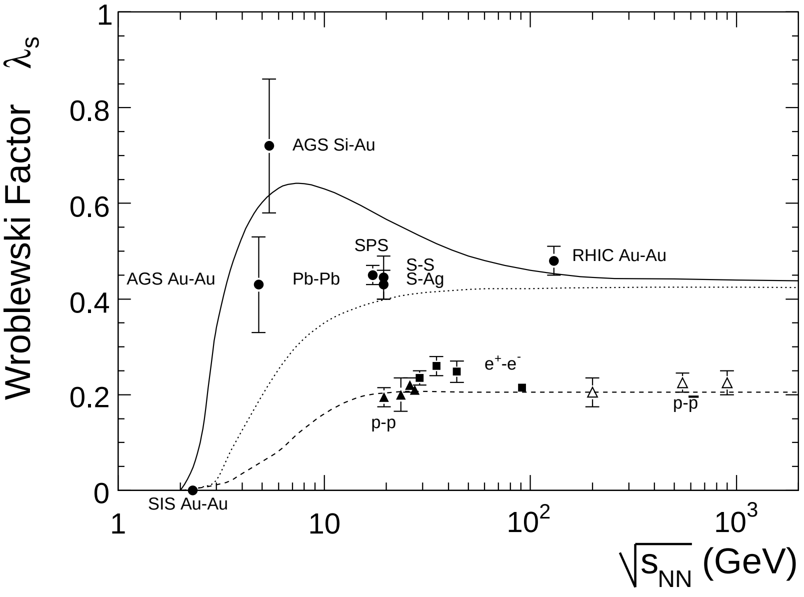

Figure 8.6: The Wroblewski factor λ_s as a function of $\sqrt{s}$. The thick solid line has been calculated using the freeze-out values [146]. The dotted line reflects a calculation using the same T but keeping $\mu_B = 0$. This demonstrates that the maximum is caused by finite baryo-chemical potential. The dashed line has been calculated using a radius of 1.2 fm, keeping $\mu_B = 0$ and taking the energy dependence of T as determined previously. In heavy ion collisions, λ_s is around 0.43 in the hadron-gas approach, which is the value associated with parameter values T = 170 MeV and $\mu_B = 0$, i.e. a QGP phase at T_c. For more details refer to [15].

- At the Tevatron, the ϕ was measured as a function of multiplicity. This was carried out because a QGP phase may be correlated with high entropy density that is a consequence of high multiplicity environment. The way used to characterise such a study was in terms of the ratio of ϕ mesons to all charged particles. Figure 8.7 (b) shows this ratio in the pseudo-rapidity range of $|\eta| \leq 3.25$ as a function of the charged multiplicity intervals. The multiplicity determination is an essential measurement in heavy ion physics because the initial energy available in the reaction, that is redistributed for producing particles in the final state, is connected to the energy density reached in the early phase of the collision [15]. This is usually estimated by the Bjorken formula [147]:

$$\epsilon_{Bjorken} = \frac{\langle m_t \rangle}{2\pi R_A^2 \tau_{th}} (\frac{dN_{ch}}{dy})_{y=0} \tag{8.2}$$

where $\langle m_t \rangle$ is the average transverse mass of the produced particles, R_A is the nuclear radius, τ_{th} is the thermalisation time, and $(\frac{dN_{ch}}{dy})_{y=0}$ is the charged particle multiplicity at mid-rapidity. At the Tevatron this analysis suffered from low statistics as shown in figure 8.7. Hence, measuring the ϕ at high multiplicity in ALICE will allow us to explore a new energy range, offering the possibility to study the role of a QGP phase transition in elementary collisions.

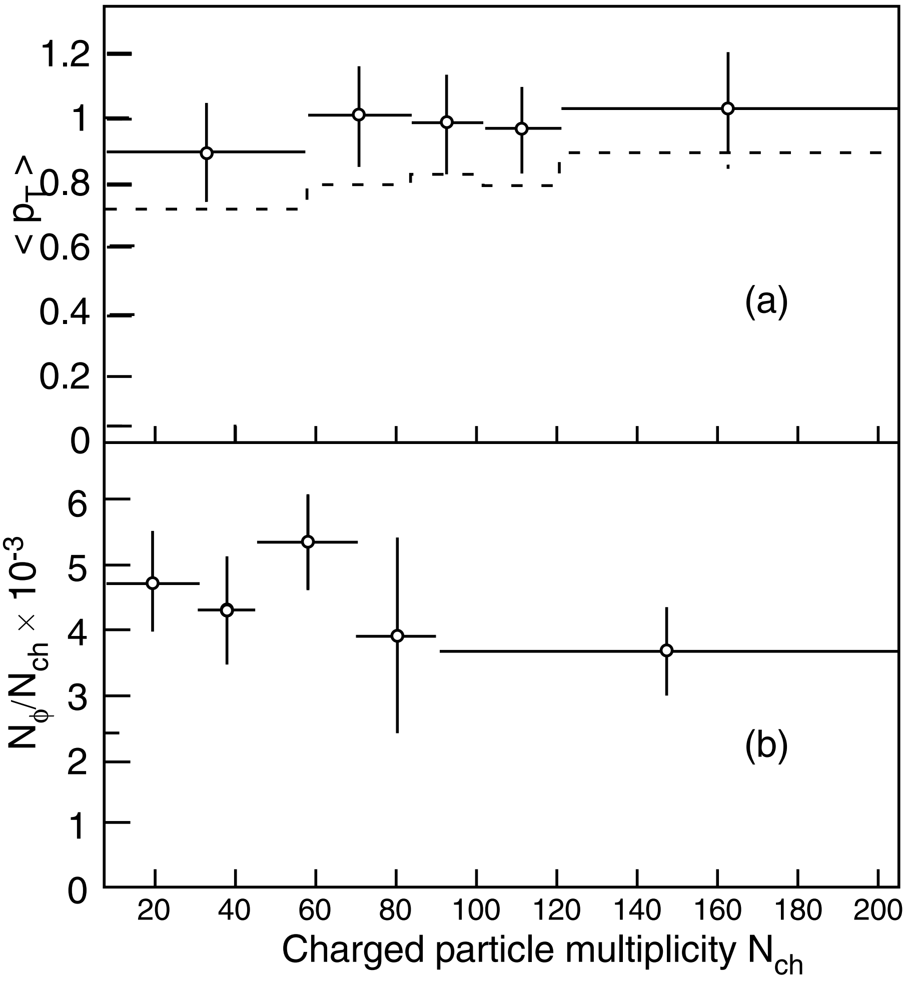

Figure 8.7: Panel (a): Average transverse momentum $\langle p_t \rangle$ of ϕ mesons versus charged multiplicity as obtained at the Tevatron, compared to the PYTHIA Monte Carlo predictions (dashed line). Panel (b): Ratio of ϕ to total number of charged tracks for $|\eta| \leq 3.25$ as a function of the charged multiplicity intervals. This figure also has a $\frac{dN_{ch}}{dN}$ scale, obtained from the current x-scale by $\frac{dN_{ch}}{dN}$ = $\frac{1}{6.5}$ N_{ch}. In ALICE the measurable multiplicity range is different (and much larger).

Chapter 9

Prospects for reconstructing $\phi(1020)$ mesons in pp collisions at the ALICE experiment

The analysis presented in this chapter summarises a performance study of the two-body decay of the ϕ meson into a charged kaon pair at the ALICE experiment. In particular, the subject of this chapter is the description of the analysis techniques used, and the predictions of reconstructed ϕ resonance signals and backgrounds in proton-proton collisions at LHC energies.

9.1 Analysis overview

This analysis considers the impact of the particle identification of charged tracks on the measurement of the resonance in question. This chapter is divided into four sections. In the first section, an overview of the kinematic distribution for the study of ϕ meson production is given, along with a preliminary study of the uncertainties on different tuning parameters of the PYTHIA Monte Carlo event generator used. In the second section, the basis of the background subtraction methods in resonance production is given. It is followed by a discussion of the errors in calculation of ϕ particles parameters. In order to obtain a reference point for the rest of the analysis, the reconstructed yields, mass and width are described when the particle identification (PID) is ideal. Results are also presented for the LHC startup when the particle PID system is not used. This chapter concludes with a summary of the results obtained, and a discussion of the list of resonance properties that can be measured during the early physics programme. Finally the particle identification performance in pp collisions is discussed briefly.

The results presented here have been achieved using the AliRoot computing framework [109], which is the official analysis software in the ALICE experiment. In order to simulate high-energy proton-proton collisions at $\sqrt{s}$= 14 TeV, the ALICE experiment has chosen the PYTHIA MC event generator [111] for its minimum bias interactions. The interface to PYTHIA includes the use of nuclear structure functions provided by LHAPDF [148]. Unless otherwise stated, the version used in this analysis was PYTHIA 6.214, and the tuning parameters were based on extrapolations to LHC energies using the so-called "ATLAS tuning" [112]. This output is passed to the detector simulation through GEANT3 [109] and then to the reconstruction process. Each of the following subsections start by describing the MC event sample that was used, followed by a description of the analysis strategy implemented. Results from both fast-simulation and full-simulation methods are discussed.

9.2 PYTHIA event generation predictions

In order to understand the event inputs that were passed to the reconstruction software, this chapter starts presenting an analysis of the generation level. A sample of 100,000 events was generated for this purpose. This event sample contained a total of 59,720 ϕ mesons, corresponding to an average of about 0.6 ϕ mesons per event. The percentage of ϕ mesons that decay into a charged kaon pair was 48.89%, which is consistent with the branching ratio (B.R.) reported from different measurements on the Particle Data Group compilation (PDG) [20]. The scatter plot (P_t,Y) of generated ϕ mesons is shown in figure 9.1, confirming that ϕ mesons can be found mostly at mid-rapidity and at low values of transverse momentum.

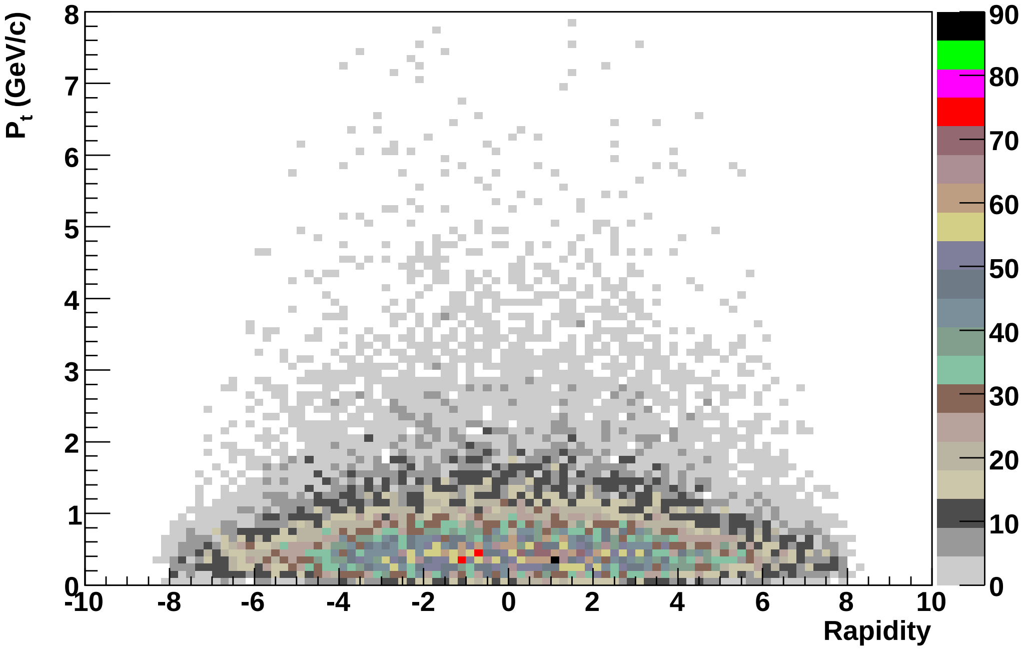

Figure 9.1: Scatter plot of transverse momentum versus rapidity (P_t,Y) for generated ϕ mesons in proton-proton collisions at $\sqrt{s}$=14 TeV.

9.2.1 Discrepancies between different extrapolations to LHC energies

Because discrepancies have been reported between the output given by different Monte Carlo event generators and their tuning parameters [112, 149], a study was carried out to check for any modifications on the kinematic distributions, or production yield of ϕ and $K^{\pm}$ mesons. This in the context of PYTHIA event generator predictions. In order to do so, a more recent version of PYTHIA and two different tuning parameters at LHC energies were used. Thus, three samples of 100,000 events were produced by implementing the following configurations:

- Sample 1: PYTHIA 6.214 with ATLAS tuning [4, 15];
- Sample 2: PYTHIA 6.326 with ATLAS tuning; and
- Sample 3: PYTHIA 6.326 with minimum bias tuning [149].

Sample 1 is the standard configuration that has been used in the ALICE physics performance studies. Because the same tuning parameters were used on sample 1 and sample 2, a comparison between them can provide an indication of any possible changes in their kinematic distributions due to the PYTHIA version used. It was found that the multiplicity and pseudo-rapidity distributions of charged kaons in both predictions are in good agreement. Similarly, the rapidity, transverse momentum and multiplicity for ϕ mesons are essentially unchanged.

Samples 2 and 3 were also studied. Their comparison should shed light on the significance of the tuning parameters since both event samples were produced using PYTHIA 6.326 [150]. It was found that the multiplicity of generated kaons, for example, is reduced dramatically for sample 3 (see figure 9.2 (a)). In particular, the rate of generated ϕ mesons is about 31% less in sample 3 relative to sample 2.

In figure 9.2 (d), a clear discrepancy in the transverse momentum of ϕ mesons is observed between the mentioned predictions for $P_t \leq 1.2$ GeV/c.

In order to summarise these results, table 9.1 presents a comparison between the three samples studied in terms of the average number of particles per event. It can be concluded from this table that when the tuning parameters were unchanged, the kinematic distributions (multiplicity, P_t, and Y) of these particles remained fairly similar. There are in fact a significant number of parameters involved in these changes, the most important of them to point out are:

- The Parton Distribution Functions (PDF). However, all these three samples use a PDF set provided by the CTEQ group.
- The parameters of PYTHIA related to strangeness production (e.g. the strange suppression factor relative to the up and down quark) were unchanged.
- The parameter associated to the probability of a given particle to be a vector (1^{-+}) rather than a pseudoscalar (O^{-+}) was not modified.
- The $\phi \rightarrow K^+K^-$ branching ratio was essentially unchanged for all predictions.

Table 9.1: Comparison of the particle production rate of generated ϕ mesons between PYTHIA 6.214 and 6.326 version along with different MC tuning parameters. The table shows the true values.

	sample 1	sample 2	sample 3
ϕ meson (average per event)	0.6	0.6	0.4
$\phi \rightarrow K^+K^-$ B.R.	48.9%	49.0%	48.6%
$\pi^\pm$ (average per event)	61	68	48
$K^\pm$ (average per event)	8	8	5

The average number of "findable" ϕ mesons per event (upper row in table 9.2) is similar for sample 1 and 2, but different for 1 (2) and 3. 'Findable" refers to those

Table 9.2: Comparison of the "findable" generated $\phi \rightarrow K^{+}K^{-}$ mesons (i.e. inside the ALICE geometrical acceptance for the central detectors) between different PYTHIA 6.214 and 6.326 version along with different MC tuning parameters. The table shows the true values.

Average per event	sample 1	sample 2	sample 3
Findable	0.02	0.02	0.02
Findable/generated	0.08	0.08	0.08

particles found inside the geometrical acceptance at mid-rapidity ($|\eta| \leq 0.9$). As expected, the ratio of findable divided by the generated ϕ mesons is the same for all three samples as this value is just an estimate of the mean acceptance with slightly different values. At least to first approximation, a conclusion can be drawn by stating that the observed discrepancies in the ϕ production rate is correlated with changes in the charged-particle multiplicity of the minimum bias pp event. However, particle ratios such as K/π and ϕ/π do not seem to be exactly constant, so the correlation is not perfect. More studies in this direction are needed to investigate this further.

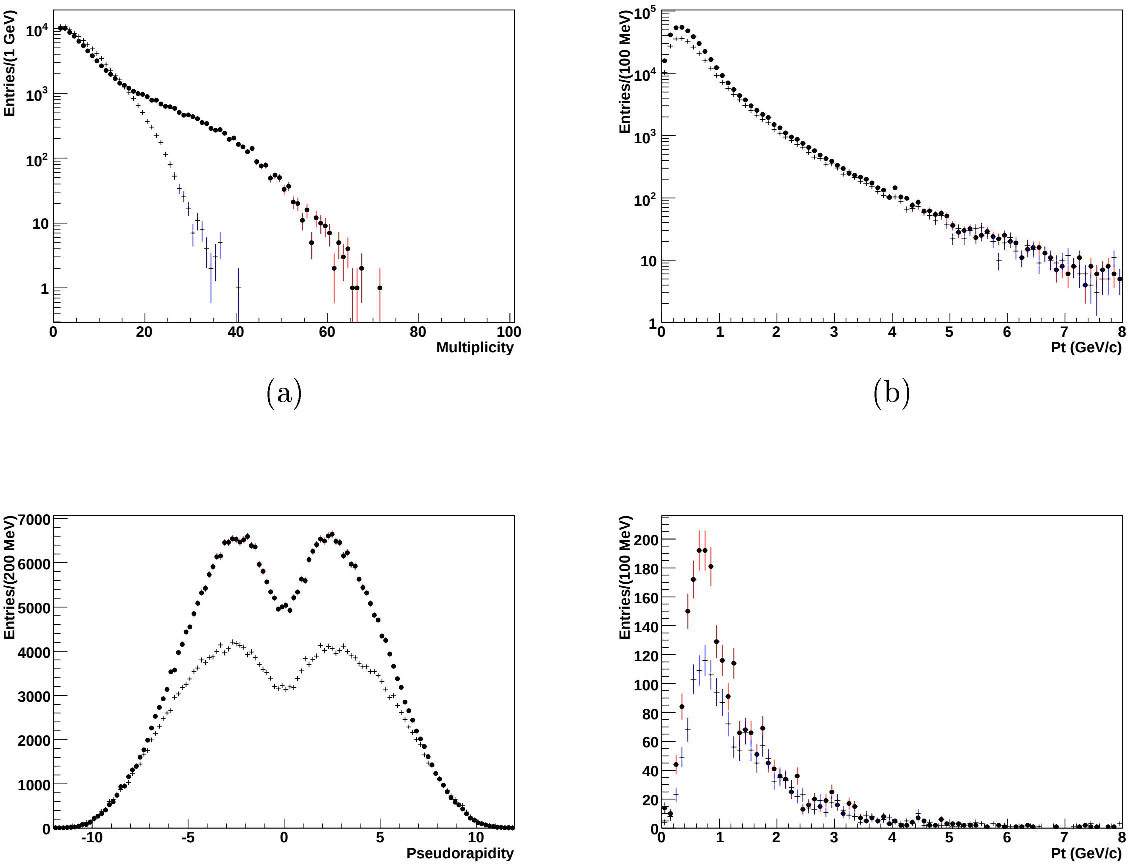

(a) (b)

(c) (d)

Figure 9.2: Comparison of PYTHIA 6.326 with the ATLAS tuning (dots, sample 2) relative to the minimum bias tuning (crosses, sample 3). Panel (a): multiplicity of charged kaons. Panel (b): transverse momentum of K^+. Panel (c): pseudo-rapidity distribution of K^+. Panel (d): transverse momentum of $\phi \rightarrow K^+K^-$ at mid-rapidity.

9.3 Steps in analysing the ϕ meson in pp collisions

The steps in analysing the ϕ meson start firstly with the identification of all possible charged kaons and retrieving the momentum of each. Secondly, the reconstruction of the invariant mass of each K^+K^- pair within each event for different rapidity and transverse momentum regions is carried out. Thirdly, the combinatorial background is subtracted making use of a background estimation technique. Finally, a fit to the K^+K^- spectrum is performed using a (relativistic) Breit-Wigner distribution [113], which allows one to calculate, for example, the ϕ meson yields as a function of transverse momentum.

9.3.1 Invariant mass calculation

After the reconstruction process, the invariant mass distribution for each K^+K^- pairs can be obtained by calculating:

$$|M_{\mathrm{inv}}|^2 = (E_{K^+} + E_{K^-})^2 - |\vec{p}_{K^+} + \vec{p}_{K^-}|^2, \qquad (9.1)$$

where the quantities E and $\overrightarrow{p}$, on the right hand side, refer to the kinematic energy and momentum of the K^+ and K^- tracks in each pair respectively. The typical invariant mass spectrum exhibits peaks above the curve, which are around the known masses of the associated resonances at their specific decay mode.

The usual way to reconstruct the signal of resonances is by pairing all charged tracks in the same event and evaluate the effective mass, as given in 9.1. The challenge ahead is to subtract the combinatorial background so the signal can be extracted and analysed. A problem arises as most of the invariant mass distribution is composed of the combination of highly uncorrelated tracks.

9.3.2 Errors in calculation of resonance properties

Resonance properties are studied by measuring the resonance momentum components, transverse momentum, mass and rapidity. These measurements are obtained through the momentum of the decay tracks. In section 3.3 a description of the ALICE physics performance is given, including the track momentum measurement. Errors in this measurement can propagate to the reconstruction of resonance properties. In this section, a review of the invariant mass and transverse momentum resolution of ϕ mesons is given.

Mass resolution

Figure 9.3 shows the invariant mass resolution of charged kaon pairs, defined as the generated invariant mass minus the reconstructed invariant mass. As expected, and in contrast to what has been reported for other resonances, such as the ρ^0 meson [151], the invariant mass resolution does not present any mass shift. A Gaussian fit to the invariant mass resolution was performed obtaining a resolution of 1.04 ± 0.02 MeV/c^2 within a selected mass window of 1.019 ± 0.02 GeV/c^2, for all values of transverse momentum.

Transverse momentum resolution

Figure 9.4 shows the errors in the reconstructed transverse momentum of ϕ mesons. This has been defined in terms of the “inverse resolution” given by

$$(\frac{1}{P_{t,rec}(\phi)} - \frac{1}{P_{t,sim}(\phi)})/P_{t,sim}(\phi), \tag{9.2}$$

where $P_{t,sim}(\phi)$ and $P_{t,rec}(\phi)$ are the generated and reconstructed transverse momentum of the ϕ particle respectively. From a Gaussian fit to the inverse transverse

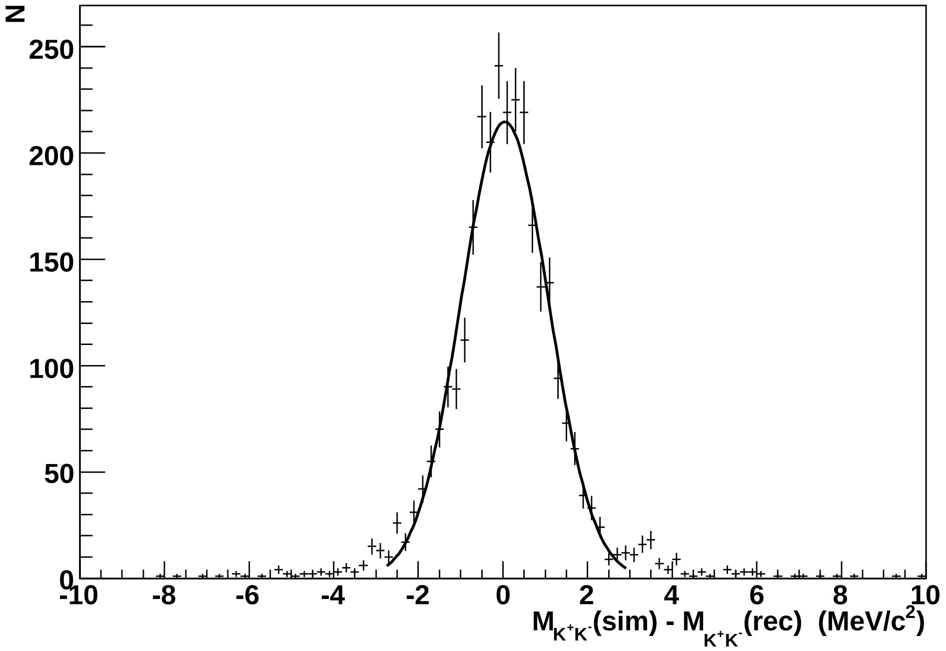

Figure 9.3: Distribution of the difference between the generated invariant mass of charged kaon pairs, and the reconstructed invariant mass. A fit with a Gaussian curve is performed. A sigma value of 1.04 ± 0.02 MeV/c^2 was obtained within a selected mass window of 1.019 ± 0.02 GeV/c^2.

momentum resolution, a $\sigma = 0.60 \pm 0.03$ GeV/c was obtained for $0.2 < P_t < 2.2$ GeV/c. This means that for a ϕ meson with transverse momentum equal to 1.5 GeV/c, a resolution of about 2.6 MeV/c is obtained.

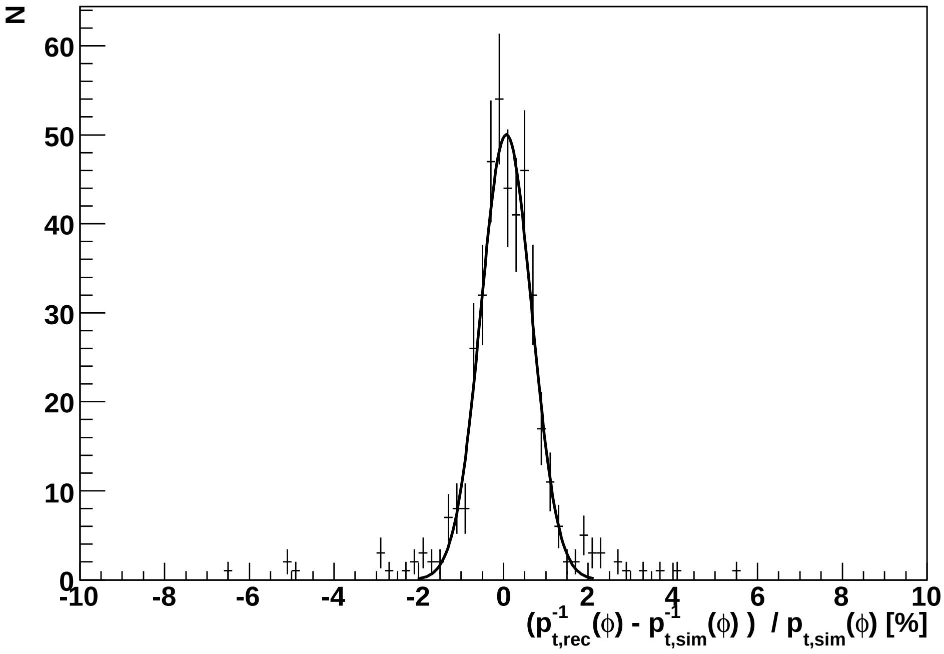

Figure 9.4: Errors in the measurement of the ϕ transverse momentum, defined in terms of the inverse transverse momentum resolution (see equation 9.2). A fit with a Gaussian curve is performed. A $\sigma = 0.60 \pm 0.03$ GeV/c was obtained for $0.2 < P_t < 2.2$ GeV/c.

Conclusions

The errors obtained in this section for the mass and inverse transverse momentum resolution have been found to be small. These come from track momentum measurement. The consequence is that the uncertainties on the calculation of the ϕ meson properties (invariant mass, transverse momentum) are also small, and they should not affect the results presented in the remainder of this chapter.

9.3.3 Background subtraction

Like-sign method

The methods performed on a same-event basis are known as "like-sign" methods as they work by pairing like-sign pairs (K^+K^+ and K^-K^-) in the same event. Two generic versions of this technique can be used for resonance studies. They are known as the "sum" like-sign option and the "product" like-sign one, related to the arithmetic and geometric mean respectively. The first of them is described by equation 9.3 and the second one is given by equation 9.4. A derivation of these formulae can be found in [129].

$$N^{+-} = N^{++} + N^{--}, \tag{9.3}$$

$$N^{+-} \approx 2\sqrt{N^{++}N^{--}}. \tag{9.4}$$

In equation 9.3, the multiplicity distribution of pairs is modelled by a binomial distribution. On the other hand, for equation 9.4 a Poisson distribution is used as a more realistic approach for the combinatorial background.

Mixing event method

In addition, it turns out that it is possible to perform a similar calculation to that of the like-sign method by matching pairs where tracks are from different events [152, 153]. The mixed event method is particularly common when analysing backgrounds in high-multiplicity environments such as those presented in heavy ion collisions. As there are more tracks in an event, any possible kinematic effect that one of them might have on another "far apart", should be less significant than in small-multiplicity events, especially so when no correlation between tracks is assumed. Based on this idea, the estimation of the combinatorial background by mixed events uses positive tracks taken from one event and negative tracks from a different but "similar" event. Figure 9.5 shows a schematic description of the event mixing method. The event similarity is defined in terms of specific criterion that have to be imposed depending on the analysis in question. In section 9.5 a description of the background subtraction in terms of the mixing event method is given. An example of a event similarity is the restriction that those events that are to be mixed contain a similar number of charged tracks. The total number of entries in the mixed-event distribution would usually have bigger statistics than its associated same-event estimation; each event can be combined with many other events.

It was found that in qualitative terms, mixed-events reproduce the shape of the background very well but the signal can easily be distorted [153]. In the heavy-ion physics community there is not currently a complete agreement on how best to construct a mixed-event background. Both methods were studied for the present analysis.

Errors in background subtraction

The background subtraction represents a significant source of systematic errors when the invariant mass distribution is overpopulated by background pairs. If this is so, the systematic error needs to be taken into account. When particle ID is used, the background is relatively small and it can be modelled easily.

9.3.4 Fitting method

In order to extract the mass, width and yields of the ϕ particles, a fit is necessary. The mass window selected for the ϕ does not need to be very large as the ϕ peak is narrow. The selected interval was 20 MeV/c^2 around 1,019.456 MeV/c^2. The resonance peaks were fitted both to a non-relativistic (RBW) and relativistic Breit-Wigner function (RBW) [113]. The fit itself was carried out by MINOS [154]. This

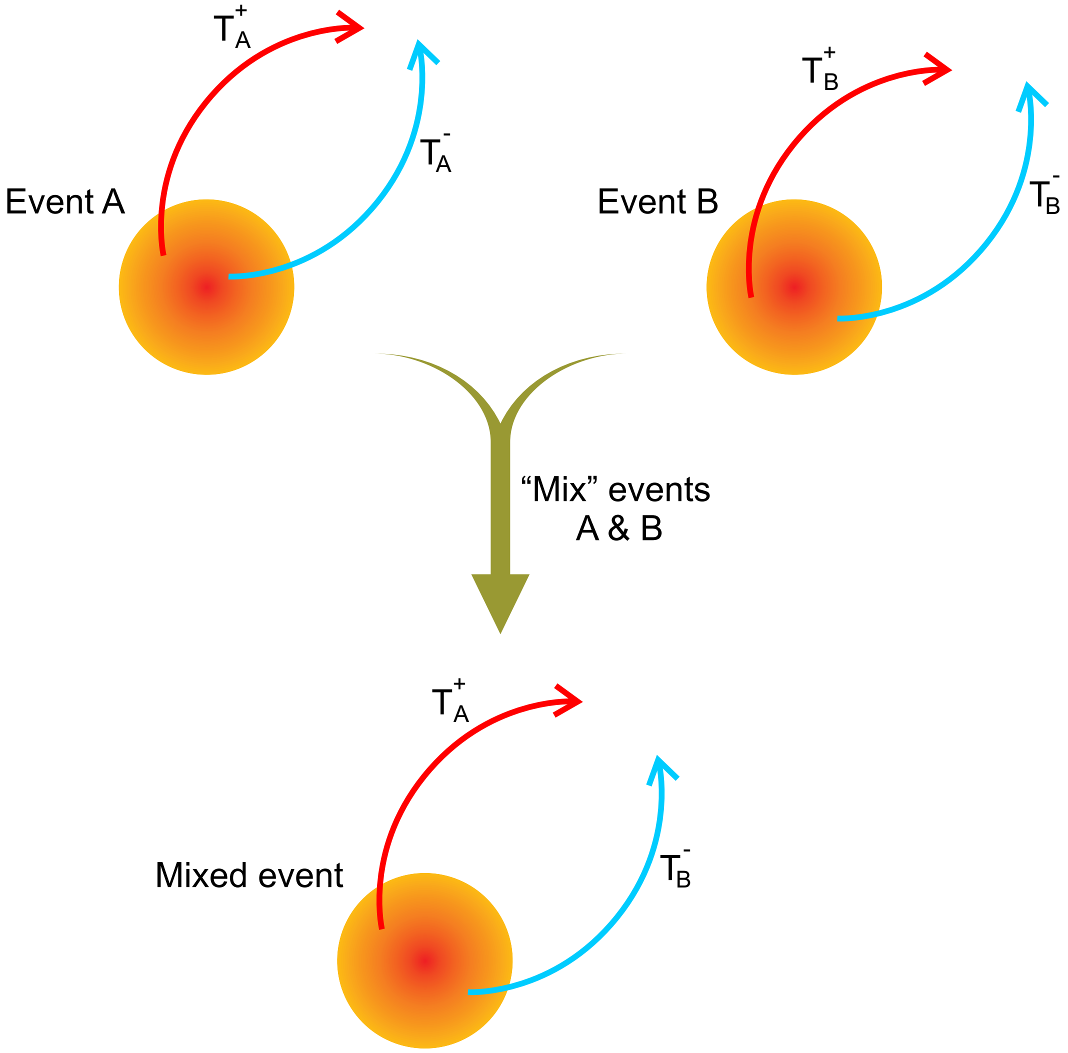

Figure 9.5: Schematic description of the event mixing method. The mixed event shown here has a multiplicity equal to two. One of its charged tracks belongs to the event A (T_A^+) and the other track to event B (T_B^-)

.

routine makes adjustments to the parameters in order to minimise the χ^2.

Non-relativistic Breit-Wigner (BW)

The non-relativistic Breit-Wigner is given by:

$$\frac{dN}{dm} = A \times \frac{\Gamma}{(m - m_0)^2 + \frac{\Gamma^2}{4}}, \tag{9.5}$$

where the mass (m_0), width (Γ) and size (A) are free parameters. The Breit-Wigner is used here as the PYTHIA event generator uses a Breit-Wigner function to generate the ϕ particles. However, a relativistic Breit-Wigner should be used in the real data [113].

Relativistic Breit-Wigner (RBW)

The relativistic Breit-Wigner used for a ϕ meson is given by:

$$\frac{dN}{dm} = \frac{m m_0 \Gamma(m)}{(m^2 - m_0^2)^2 + (m_0 \Gamma(m))^2}, \tag{9.6}$$

where

$$\Gamma(m) = 2\Gamma_0 \frac{(q/q_0)^3}{(q/q_0)^2 + 1} \tag{9.7}$$

$$q_0 = \sqrt{m_0^2/4 - m_K^2} \tag{9.8}$$

$$q = \sqrt{m^2/4 - m_K^2} \tag{9.9}$$

9.3.5 Signal significance estimation

The signal significance is defined as the number of ϕ signals divided by the statistical fluctuation of the number of ϕ mesons plus the number of background pairs, which is given by:

$$\text{Significance} = \frac{S}{\sqrt{S + B}} \tag{9.10}$$

where S is the number of ϕ signals in a particular mass window region, and B is the number of the combinatorial background pairs in the same mass region. Because the signal significance is proportional to $\sqrt{N_{\text{events}}}$, it improves as the number of events increase. The signal significance obtained in this thesis were carried out by calculating the signal S from the fitted value of the reconstructed yields, after background subtraction.

If a significance Sig_0 is obtained for a sample with number of events N_0, the number of events required (N) in order to obtain a significance Sig is:

$$\text{N} = \text{N}_0(\frac{\text{Sig}}{\text{Sig}_0})^2. \tag{9.11}$$

This is so assuming that the signal-to-background ratio is a constant value. Projections can be obtained from this formula as shown later in this thesis.

9.4 Reconstructed $\phi(1020)$ mesons in pp collisions at the ALICE experiment

9.4.1 Event generation and track selection

Events distributed by GRID services were not available at the time this analysis was carried out. Hence, the Monte Carlo data sample used in this analysis was produced using a fast-simulation method developed by the Birmingham group [151]. This routine attempted to reproduce the output given by the detailed simulation that passed through the full chain of the reconstruction software. It has been successfully applied in the analysis of the ρ^0 meson both in pp and Pb-Pb collisions [15]. A sample of 7×10^6 minimum bias PYTHIA events was analysed, and the track selection was based on the following points:

- Because the short lifetime of resonances, they all decay at the primary vertex, so the track selection excludes particles from secondary interactions. Impact parameter cuts were applied to the primary vertex as described in [151]. The remaining secondary particles are few in number and they have been ignored by the fast simulation method.

- The tracks were selected at mid-rapidity ($|\eta| \leq 0.9$).

- No cuts, either on multiplicity, or on in transverse momentum were used.

- The particle ID was used with a 100% PID efficiency for kaons, i.e. although the reconstruction was carried out fully, the Monte Carlo truth information was used to identify the true kaons.

9.4.2 Errors in fitting reconstructed signals

Reconstructed mass and width

Fits to the reconstructed ϕ meson signal were performed removing the background using the Monte Carlo truth information. For example, figure 9.6 shows the relativistic Breit Wigner fit to ϕ signals with a transverse momentum of $1.4 < \mathrm{P}_{t,K^+K^-} \leq 1.6$ GeV/c.

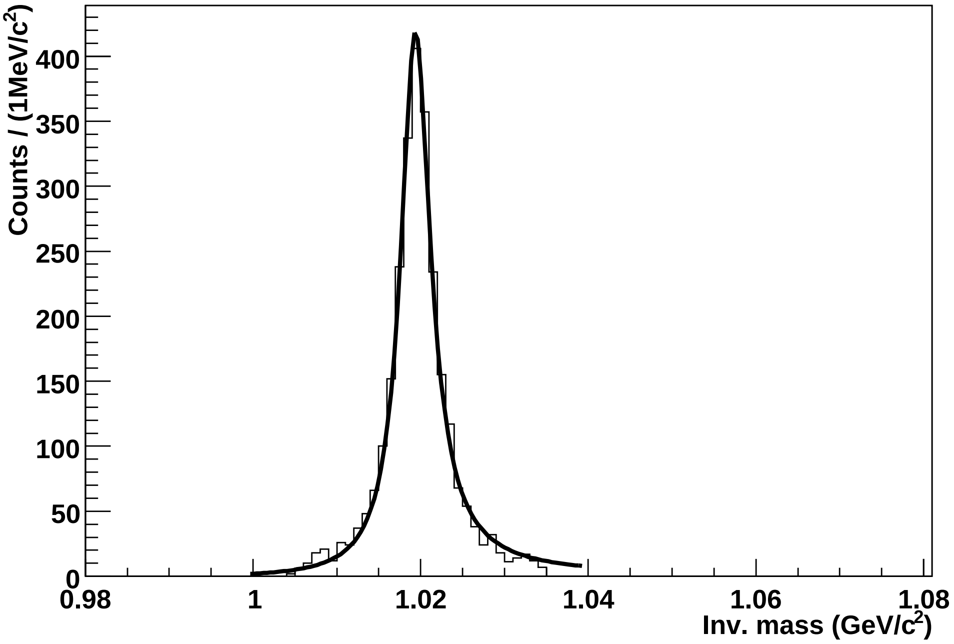

Figure 9.6: Relativistic Breit Wigner fit to reconstructed ϕ signal ($1.4 < \mathrm{P}_{t,K^+K^-} \leq 1.6$ GeV/c), with background removed using the MC truth information.

In order to determine any possible effect of the line shape distortion described in chapter 8, the fitted masses and widths are obtained as shown in table 9.3 and table 9.4. As expected, the fitted masses do not show a mass shift with respect to the generated value, and with respect of the PDG value: $\mathrm{m_{PDG}} = 1019.456$ MeV/c^2 and $\Gamma_{\mathrm{PDG}} = 4.26 \pm 0.05$ MeV/c^2 [20]. However the width is slightly away from the generated value, therefore the effects on efficiency correction on the measurement of width should be studied in the future. The errors for both measurements, mass and width, are small, and their central values are not significantly deviated from the generated values. Figure 9.7 shows the widths of the reconstructed ϕ mesons as a function of transverse momentum of the charged kaon pairs, with background removed using the Monte Carlo true information. The values shown correspond to the fitted values obtained by a RBW fit.

Table 9.3: Reconstructed ϕ meson mass and width as a function of transverse momentum from P_t >0.2 GeV/c to P_t ≤2.0 GeV/c. The fitted values were obtained from both a non-relativistic (BW) and relativistic Breit-Wigner (RBW) fit, in presence of no background.

P_t (GeV/c)	Mass (MeV/c^2)		Width (MeV/c^2)	
	RBW	BW	RBW	BW
All	1019.25±0.02	1,019.50±0.02	4.28±0.035	4.35±0.035
$0.2 < P_t \leq 0.4$	1019.54±1.02	1,020.16±1.18	8.78±3.95	9.61±4.51
$0.4 < P_t \leq 0.6$	1019.21±0.09	1,019.43±0.09	4.13±0.19	4.34±0.20
$0.6 < P_t \leq 0.8$	1019.24±0.05	1,019.48±0.05	4.27±0.11	4.29±0.11
$0.8 < P_t \leq 1.0$	1019.21±0.05	1,019.46±0.05	4.28±0.10	4.34±0.10
$1.0 < P_t \leq 1.2$	1019.26±0.05	1,019.48±0.05	4.07±0.10	4.11±0.10
$1.2 < P_t \leq 1.4$	1019.21±0.06	1,019.46±0.05	4.32±0.12	4.38±0.12
$1.4 < P_t \leq 1.6$	1019.30±0.06	1,019.57±0.06	4.36±0.12	4.32±0.12
$1.6 < P_t \leq 1.8$	1019.28±0.06	1,019.50±0.07	3.94±0.12	4.00±0.12
$1.8 < P_t \leq 2.0$	1019.31±0.075	1,019.55±0.07	4.20±0.14	4.31±0.145

9.4.3 Background estimation

Figure 9.8 shows the K^+K^- invariant mass distribution and the estimation of the background using the like-sign method by assuming 100% PID efficiency for kaons. The ϕ signal is clearly seen over the combinatorial background obtained for the K^+K^- pairs. The main focus of this chapter will be on reconstructing ϕ mesons

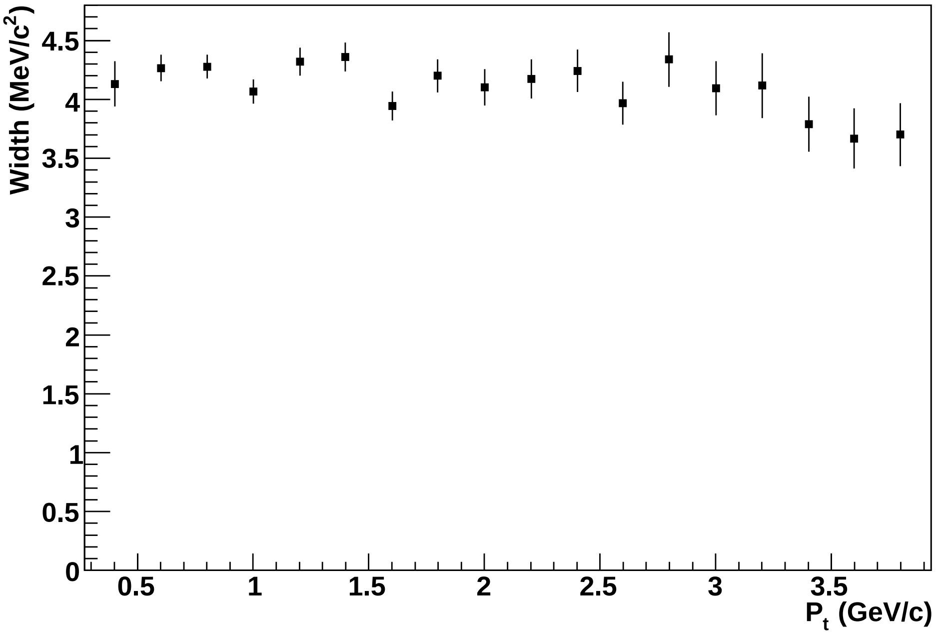

Figure 9.7: Width of the reconstructed ϕ mesons as a function of transverse momentum of the charged kaon pairs, with background removed using the Monte Carlo true information. The values shown corresponds to the fitted value obtained by a RBW fit.

Table 9.4: Reconstructed ϕ meson mass and width as a function of transverse momentum from P_t >2.0 GeV/c to P_t ≤4.0 GeV/c. The fitted values were obtained from both a non-relativistic (BW) and relativistic Breit-Wigner (RBW) fit, in presence of no background.

P_t (GeV/c)	Mass (MeV/c^2)		Width (MeV/c^2)	
	RBW	BW	RBW	BW
$2.0 < P_t \leq 2.2$	1019.20±0.07	1,020.42±0.07	4.10±0.155	4.17±0.16
$2.2 < P_t \leq 2.4$	1019.21±0.09	1,019.46±0.08	4.17±0.165	4.13±0.16
$2.4 < P_t \leq 2.6$	1019.22±0.09	1,019.48±0.09	4.24±0.18	4.28±0.18
$2.6 < P_t \leq 2.8$	1019.45±0.09	1,019.67±0.09	3.97±0.18	4.01±0.18
$2.8 < P_t \leq 3.0$	1019.34±0.155	1,019.59±0.11	4.34±0.23	4.47±0.23
$3.0 < P_t \leq 3.2$	1019.42±0.11	1,019.65±0.10	4.10±0.23	4.05±0.22
$3.2 < P_t \leq 3.4$	1019.26±0.13	1,019.48±0.12	4.12±0.28	4.10±0.26
$3.4 < P_t \leq 3.6$	1019.39±0.14	1,019.64±0.14	3.79±0.23	3.86±0.24
$3.6 < P_t \leq 3.8$	1019.63±0.15	1,019.84±0.14	3.67±0.255	3.65±0.25
$3.8 < P_t \leq 4.0$	1019.11±0.093	1,019.40±0.155	3.70±0.27	3.80±0.28

without using the particle ID information provided by the detectors. Therefore, a description of the background subtraction will be given in the following section.

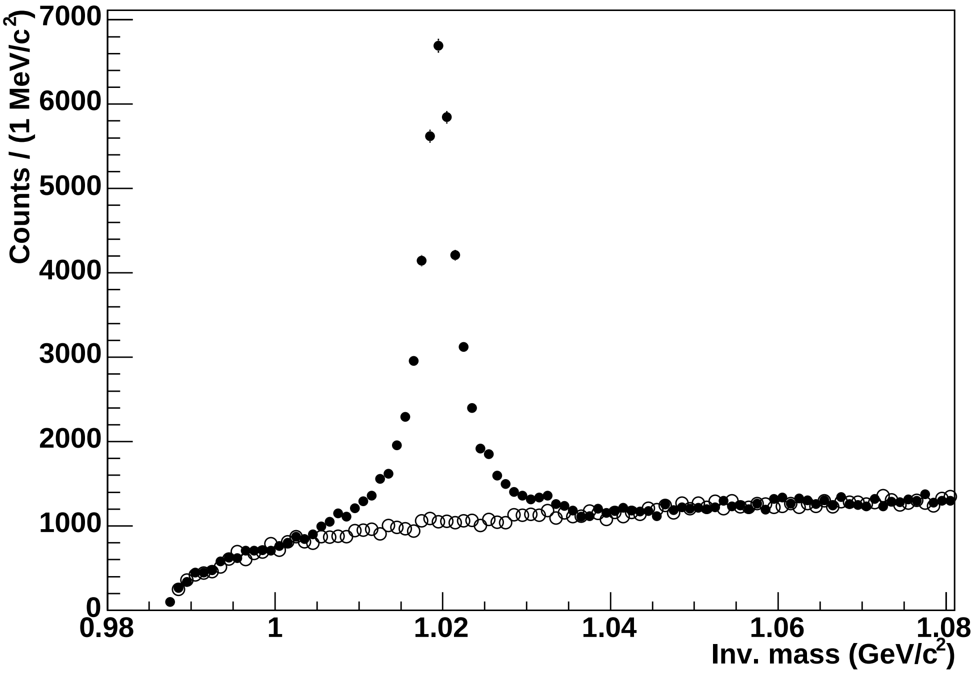

Figure 9.8: K^+K^- invariant mass spectrum for pp collisions, assuming perfect particle identification efficiency for charged particles (black dots). The invariant mass of like-sign kaon pairs (open dots) is also shown.

9.5 Prospects of ϕ meson production at the LHC startup: early physics in ALICE

9.5.1 Motivations

The narrow width and the good signal-to-background ratio for the ϕ imply that the ALICE experiment should be able to detect it early in the running of the LHC. Hence, prospects of ϕ meson measurements during the LHC start-up were studied. However, during that period the particle identification system might not be fully tuned. A study was carried out to investigate the prospects for measuring ϕ mesons without accessing any of the PID information provided by the detectors. The extraction of the signal was performed for different sub-ranges of transverse momenta, and an estimation of the signal-to-background ratio and the signal significance were obtained.

9.5.2 Event and track selection

A sample of 7×10^6 minimum bias PYTHIA events at $\sqrt{s} = 14$ TeV was analysed, as described in section 9.4. The track selection was the following:

- The track selection was such that only charged tracks with a transverse momentum greater than 0.1 GeV/c, and less than or equal to 4 GeV/c were studied.
- Secondary tracks were removed as described in 9.4.
- The background subtraction was carried out using both the like-sign and mixing event method (see below).

- In order to separate events with low-multiplicity charged tracks, the event sample was divided into multiplicity ranges so that events with high correlations between track particles can be ignored. Therefore, three cases were defined as a function of the multiplicity of negative tracks.
- No particle ID was used, i.e. the invariant mass distribution for two charged tracks was produced assuming all tracks to be kaons.

9.5.3 Charged track multiplicity measurement

Figure 9.9 shows the multiplicity of charged tracks at mid-rapidity (i.e. $|\eta| \leq 0.9$) for this sample of 7×10^6 minimum bias PYTHIA events. The total number of events selected from this sample was 5.25 $\times10^6$ events. Table 9.5 shows the number of events and mean multiplicity as a function of the charged track multiplicity for the selected sample.

9.5.4 Background subtraction

Figure 9.10 shows the invariant mass distribution for two charged tracks, not using the information provided by the particle identification (PID) with both tracks assigned as kaons; the negative charged multiplicity was required to be in the range between 5 and 25, and only tracks at mid-rapidity ($|\eta| \leq 0.9$) were considered. The peak observed at 1.019 GeV/c^2 belongs to the ϕ meson.

The mixed event method was also studied for background subtraction purposes. The condition of "similarity" in the mixed event method was imposed by ordering the events according to the multiplicity of the negatively charged tracks; only events where the difference in the negative charged track multiplicity is less than 10 were mixed. Similar results were obtained for maximum difference of less than 5, or 7. Figure 9.11 shows the comparison between the mixed event background (open

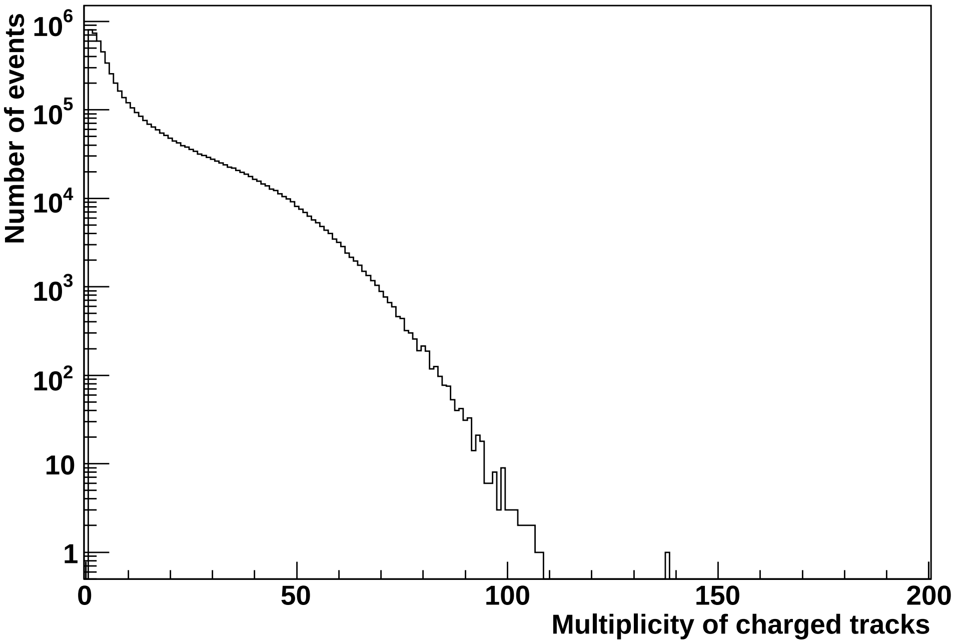

Figure 9.9: Multiplicity of charged tracks at mid-rapidity (i.e. $|\eta| \leq 0.9$) for this sample of $7{\times}10^6$ minimum bias PYTHIA events.

Table 9.5: Number of events as a function of the charged track multiplicity at mid-rapidity (i.e. $|\eta| \leq 0.9$), and its associated mean multiplicity.

Multiplicity range	Number of events	Mean multiplicity
μ_{chg} <5	2.6 $\times 10^6$	2
$5 \leq \mu_{chg} < 25$	2.1 $\times 10^6$	11
$25 \leq \mu_{chg} < 50$	510,449	34
$50 \leq \mu_{chg} < 100$	81,806	58
$100 \leq \mu_{chg} < 150$	20	105

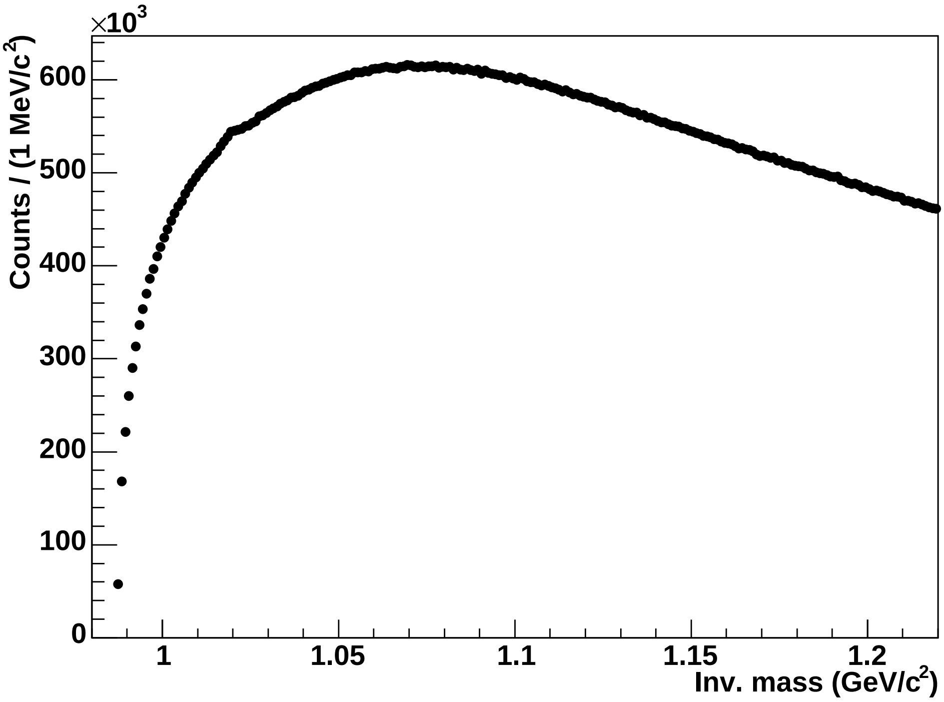

Figure 9.10: Invariant mass of two charged tracks when no particle ID is used, in pp collisions at 14 TeV. The peak at 1.019 GeV/c^2 corresponds to the ϕ resonance.

circles) with the like-sign estimation (full dotted). Because of the difficulties in constructing a mixed event distribution, and taking into account the good performance of the like-sign method, only the same-event like-sign background estimation will be considered for the remainder of this chapter.

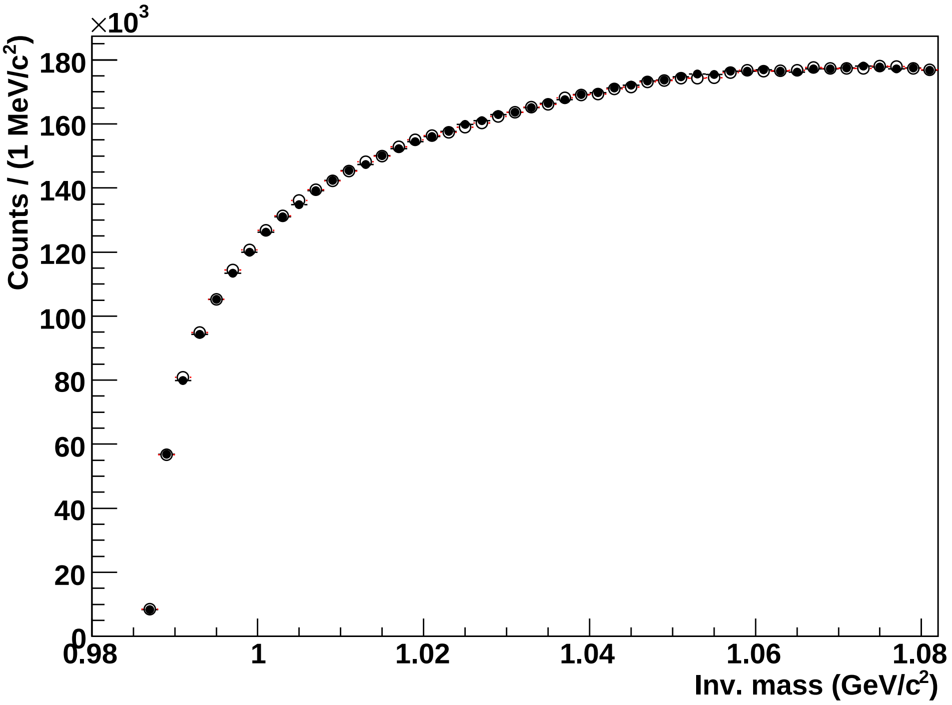

Figure 9.11: Comparison of the mixed event background (open circles) with the estimation provided by the like-sign method (full dotted). The mass distribution was obtained from 2×10^6 pp minimum bias events.

It was found that by applying a relatively high transverse momentum cut on the candidate pair, the ϕ meson peak could be resolved. Figure 9.12 shows the results for the K^+K^- invariant mass spectrum in pp collisions for pairs with $2.4 < p_t < 2.8$ GeV/c and figure 9.13 shows this spectrum after the subtraction of the background, showing that a resonance signal above the combinatorial background can be obtained from 7×10^6 events. The resonance peak was fitted as described in section 9.3.4.

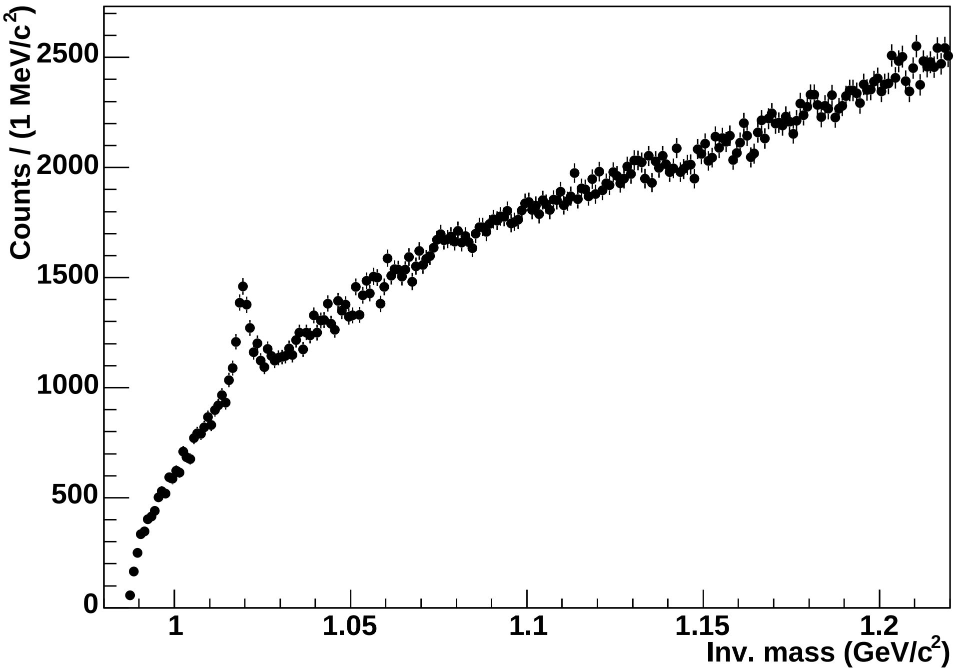

Figure 9.12: Invariant mass spectrum in pp collisions without accessing the PID information from the detectors. A cut on the transverse momentum of the pair of 2.4$< p_t <$2.8 GeV/c was used.

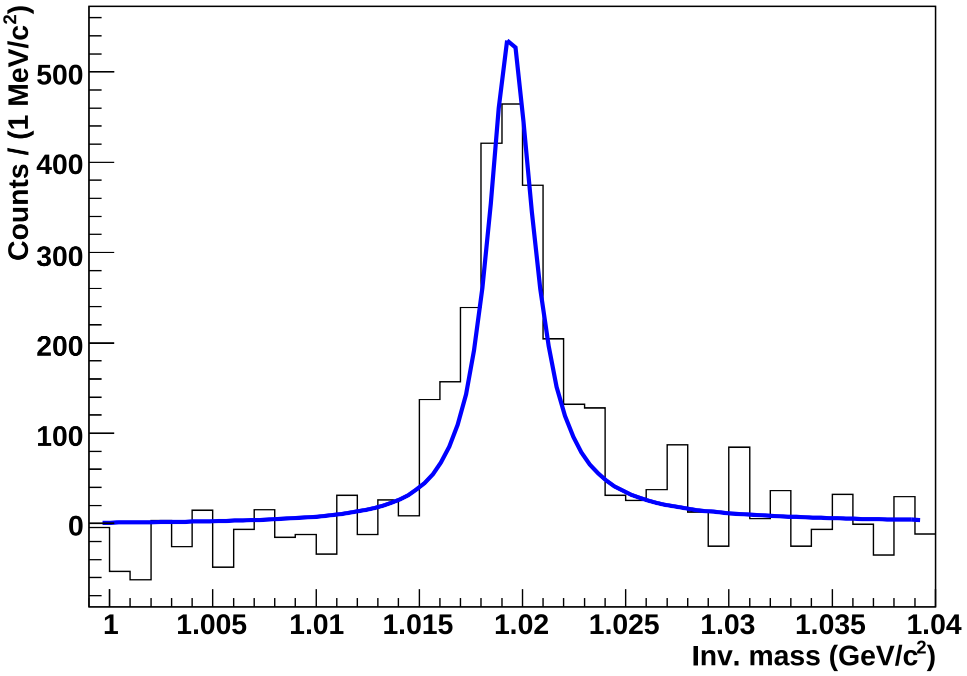

Figure 9.13: Invariant mass spectrum in pp collisions without accessing the PID information from the detectors, after background subtraction. A cut on the transverse momentum of the pair of 2.4< p_t <2.8 GeV/c was used, along with a selection of charged negative track multiplicities of 5≤ μ_{neg} <25.

9.5.5 Reconstructed mass and width

Table 9.6 shows the reconstructed mass and width of the ϕ after background subtraction. In the same way as described above for the reconstructed yield measurements, the fitted values of both the mass and width were obtained by a relativistic Breit-Wigner (RBW) fit described in section 9.3.4, with a mass window of 20 MeV/c^2 around 1019.456 MeV/c^2. The fitted mass values are consistent with those presented in section 9.4.2. However, the width values are underestimated. This comes from a systematic error in the background subtraction due to an invariant mass distribution dominated by the combinatorial background. Further studies will be needed in order to assess the best way to estimate the systematic errors in these measurements.

Table 9.6: Reconstructed mass and width of ϕ meson signals after background subtraction, when no particle ID is used. The fitted values are shown as a function of transverse momentum and charged negative track multiplicity.

P_t (GeV/c)	Mass (MeV/c^2)		Width (MeV/c^2)	
	All	5≤ μ_{neg} <25	All	5≤ μ_{neg} <25
$1.2 < P_t \leq 1.6$	1019.37 ± 0.04	1,019.54 ± 0.04	4.02 ± 0.07	3.76 ± 0.08
$1.6 < P_t \leq 2.0$	1019.26 ± 0.04	1,019.95 ± 0.03	3.05 ± 0.05	2.28 ± 0.05
$2.0 < P_t \leq 2.4$	1019.55 ± 0.04	1,019.78 ± 0.05	3.50 ± 0.075	3.67 ± 0.09
$2.4 < P_t \leq 2.8$	1019.22 ± 0.05	1.019.39 ± 0.06	3.34 ± 0.078	2.68 ± 0.07

9.5.6 Reconstructed yields: signal and backgrounds

The reconstructed yields of ϕ signal and the combinatorial backgrounds were obtained. After background subtraction, the invariant mass spectrum was fitted by a relativistic Breit-Wigner (RBW) fit described in section 9.3.4. The mass window used was 20 MeV/c^2 around 1019.456 MeV/c^2. Table 9.7 shows the reconstructed signal after background subtraction and the combinatorial background yields as a function of transverse momentum of the charged track pairs. This was calculated for all multiplicities and for the case when the charged negative track multiplicity was $5\leq \mu_{neg} < 25$. The signal-to-background ratio and signal significance (defined in section 9.3.5) of these values are shown in table 9.8. As envisaged, the signal-to-background ratio does not appear to change significantly with respect to the multiplicity ranges used. As expected, this ratio increases with higher values of transverse momentum cuts.

Table 9.7: Signals and backgrounds for reconstructed ϕ mesons after background subtraction as a function of transverse momentum of the charged track pairs. These values were obtained for all multiplicities and for negative charged track multiplicities of $5\leq \mu_{neg} < 25$.

P_t (GeV/c)	Signal		Background	
	All	$5\leq \mu_{neg} < 25$	All	$5\leq \mu_{neg} < 25$
$1.2 \leq P_t < 1.6$	5,263 ± 67	4,291 ± 61	$1.06\times10^6 \pm 1.03 \times10^3$	75,3707 ± 868
$1.6 \leq P_t < 2.0$	3,872 ± 54	2,656 ± 44	310,024 ± 557	222,507 ± 472
$2.0 \leq P_t < 2.4$	2,920 ± 48	2,171 ± 41	117,401 ± 343	85,183 ± 292
$2.4 \leq P_t < 2.8$	2,225 ± 41	1,457 ± 32	54,950 ± 234	40,174 ± 200

Table 9.8: Signal-to-background ratio and signal significance for reconstructed ϕ mesons after background subtraction as a function of transverse momentum of the charged kaon pairs. These values were obtained for all multiplicities and for negative charged track multiplicities of $5\leq \mu_{neg} < 25$.

P_t (GeV/c)	S/B		$\mathrm{S}/\sqrt{\mathrm{S}+\mathrm{B}}$	
	All	$5\leq \mu_{neg} < 25$	All	$5\leq \mu_{neg} < 25$
$1.2 \leq P_t < 1.6$	$0.005 \pm 6\times10^{-5}$	$0.006 \pm 8\times10^{-5}$	5	5
$1.6 \leq P_t < 2.0$	$0.01 \pm 2\times10^{-4}$	$0.012 \pm 2\times10^{-4}$	7	6
$2.0 \leq P_t < 2.4$	$0.025 \pm 4\times10^{-4}$	$0.025 \pm 5\times10^{-4}$	8	7
$2.4 \leq P_t < 2.8$	$0.04 \pm 7\times10^{-4}$	$0.04 \pm 8\times10^{-4}$	9	7

9.5.7 Projections for early physics programme

Using an average signal significance of 7 (see table 9.8), projections for an early physics programme can be obtained. Table 9.9 shows the projections for the number of events needed to obtain the signal significance quoted. This was obtained by extrapolating from a significance equal to 7, and assuming that the signal-to-background ratio is a constant value. The data taking time needed to obtain the estimated number of events is also shown for 80 Hz of inelastic rate ($\mathcal{L} = 10^{30}$ cm^{-2}s^{-1} and $\sigma_{MB} \sim 100$ mb). This can be considered as a realistic estimation for the LHC startup.

Table 9.9: Projections for the number of events needed to obtain the signal significance quoted, extrapolating from a significance equal to 7 and assuming that the signal-to-background ratio is constant. The data taking time needed to obtain the estimated number of events is also shown for an inelastic rate of 80 Hz.

Significance	Number of events	Data taking need (time in weeks) 80 Hz
10	1.4×10^7	0.3
15	3.2×10^7	0.7
20	5.7×10^7	1.2
25	8.9×10^7	1.8

9.5.8 Reconstructed transverse momentum distribution

The reconstructed transverse momentum of ϕ mesons after background subtraction, without using particle ID, was compared to the associated MC truth distribution. Figure 9.14 shows this comparison, only reconstructed signals between about 1.2 and 2.8 GeV/c are shown here. The region above 3 GeV/c was not explored in this study as it requires better statistics than those available for this analysis.

In order to compare the two distributions shown in figure 9.14, figure 9.15 shows

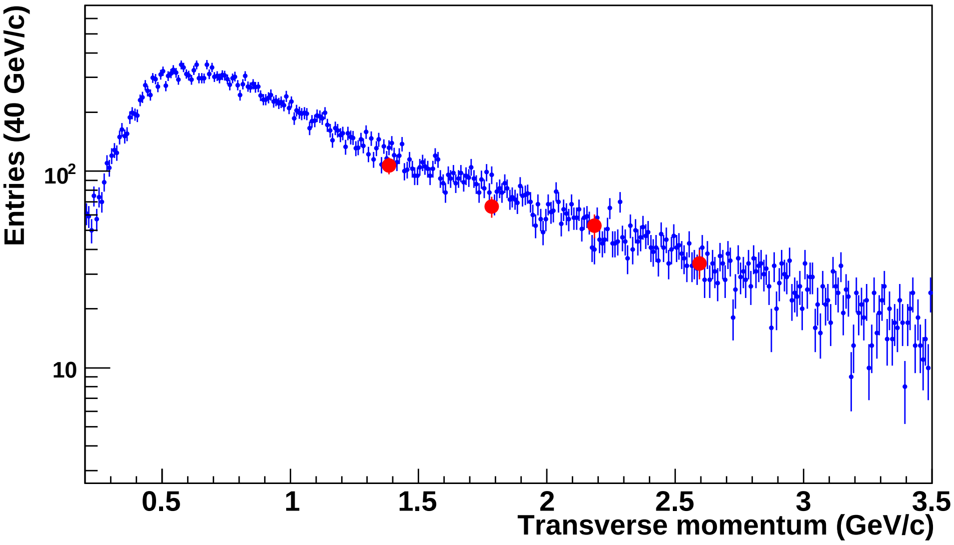

Figure 9.14: Comparison of the reconstructed ϕ meson transverse momentum (the four filled circles shown here) with the associated MC truth distribution given by PYTHIA. Distribution for negative charged tracks multiplicities of $5 \leq \mu_{neg} < 25$.

the reconstruction efficiency of reconstructed ϕ mesons as a function of transverse momentum, which was defined as the reconstructed signal divided by the associated one from the MC truth information, and then multiplied by 100. This figure shows that the efficiency is not a constant but increases as a function of transverse momentum. This is in agreement with what has been presented previously (see section 9.5.6) regarding the signal significance, i.e. both of them increase as the transverse momentum of the pair increases.

Further studies will be needed in order to carry out corrections for such a distribution. With the use of particle ID, the transverse momentum region below 2 GeV/c will be reconstructed fully. This study concludes that only using a relatively high transverse momentum cut on the candidate pair can the ϕ signal be resolved without the use of particle ID.

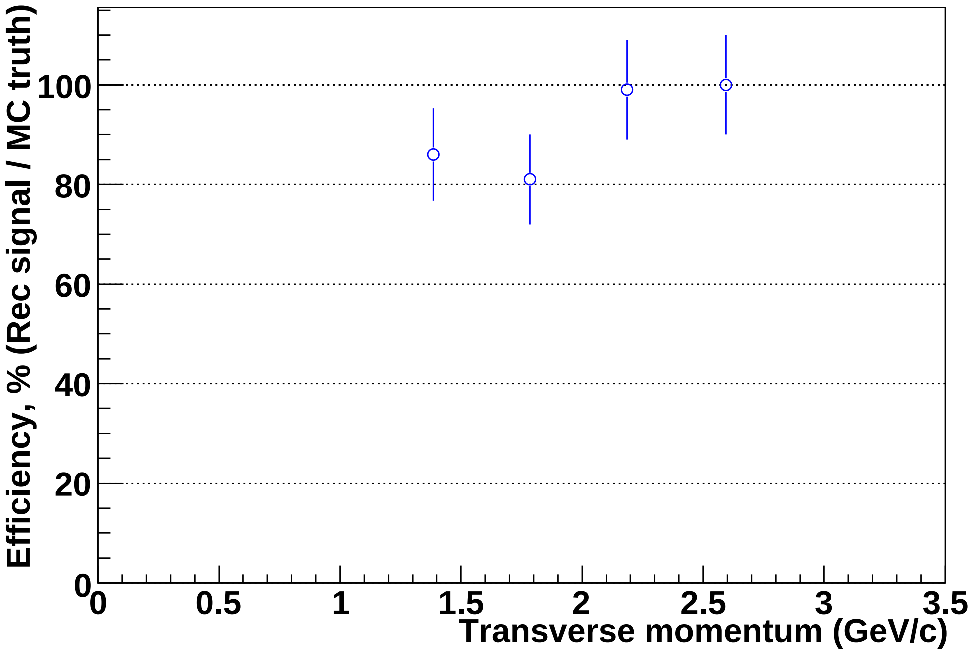

Figure 9.15: Reconstruction efficiency of ϕ mesons in pp collisions at 14 TeV, as a function of transverse momentum (see figure 9.14).

9.6 PID performance in pp collisions

A detailed simulation was carried out to perform the full-simulation effects of the PID system. A sample of 140,000 full-simulated pp events was generated using the Particle Data Challenge (PDC'05) configuration [109]. All the main tracking detectors (ITS, TPC, TRD and TOF) were included in the full chain of the execution flow of the simulation and reconstruction software. A description of the particle ID performance was given in section 3.3. As mentioned in this section, in order to identify any charged particles, a Bayesian approach is used [109]. There are basically two possibilities to obtain the particle identification information provided by the ALICE detectors: one of them is to identify kaons using a specific detector, and the other option is to combine information coming from several detectors, with the aim to decrease the probability of misidentification. In the present study, all tracks were required to have a "combined PID", i.e. all PID central detectors were involved in the process. For this analysis, the kaon-like tracks were defined as all tracks where the PID weights for being a kaon is greater than any other species. All tracks surviving this PID process were treated as kaons.

Figure 9.16 shows the reconstructed invariant mass distribution of K^+K^- pairs obtained from this event sample. A peak corresponding to the ϕ meson can clearly be seen above the combinatorial background, as estimated by the like-sign method. In this study, no cuts on the multiplicity of charged particles were used since the sample analysed was relatively small in size.

After subtraction of the combinatorial background, the ϕ meson signal can be extracted. Although the PID method included all the central detectors mentioned above, it was not optimised fully. In figure 9.17 kaons misidentified as electrons (γ conversions) are observed at low values of the effective mass distribution. More strict cuts on the impact parameter or transverse momentum cuts will remove such background as was shown in previous sections. Alternatively, the TOF and TPC

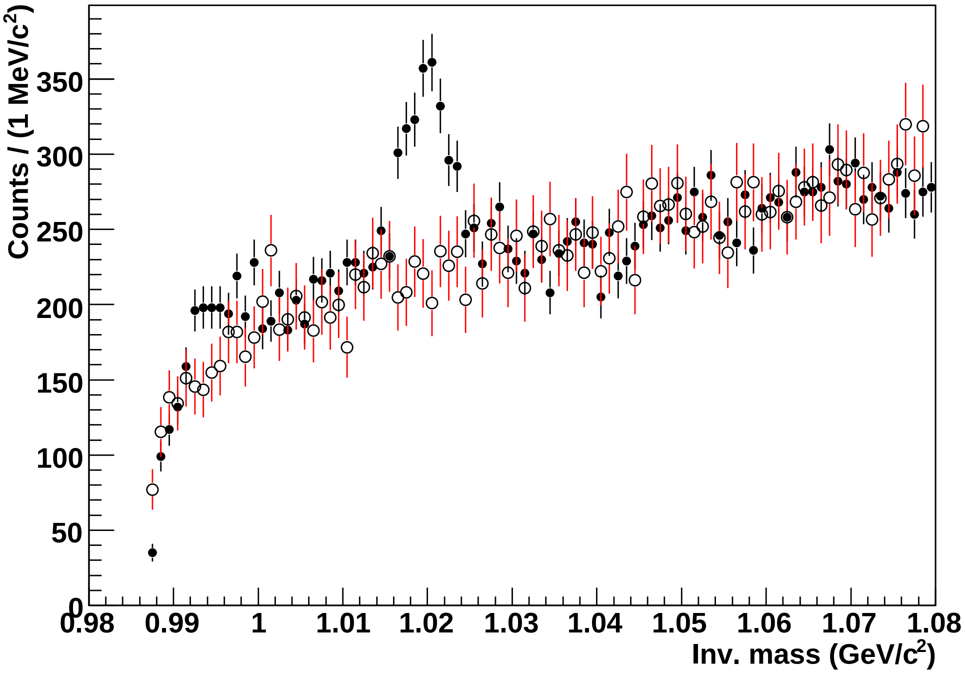

Figure 9.16: Reconstructed invariant mass distribution of K^+K^- pairs obtained from 140,000 pp minimum bias events. Realistic particle identification was used.

capabilities at different ranges of momentum can also be used for this purpose.

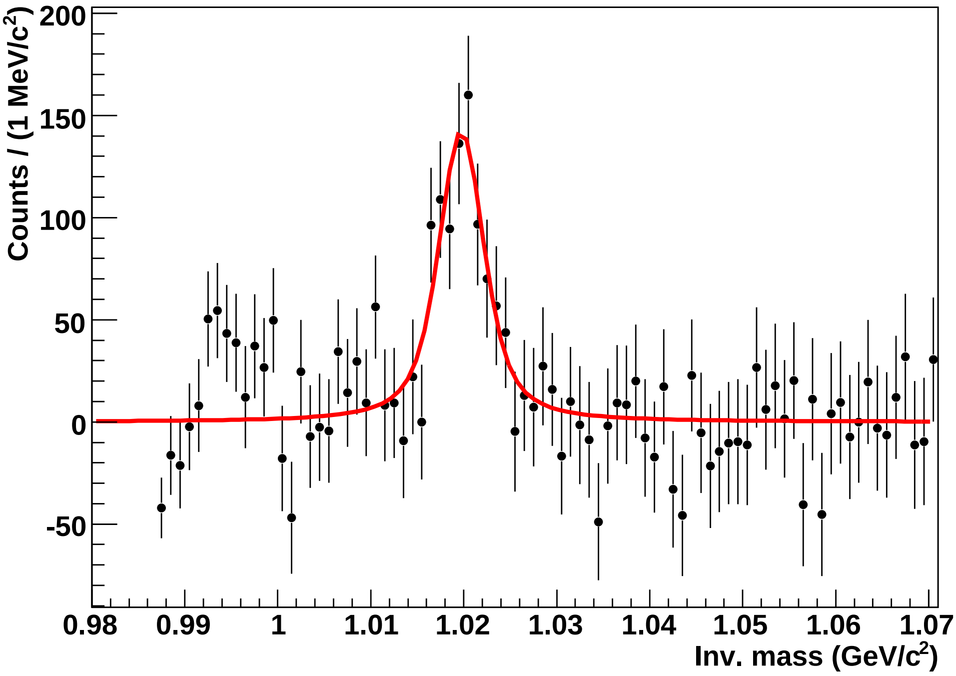

Figure 9.17: Reconstructed invariant mass distribution of K^+K^- pairs obtained from 140,000 pp minimum bias events. Realistic particle identification was used.

The conclusion of this analysis is that, using the particle ID system, the ϕ meson can be extracted from the background easily in pp collisions, allowing the measurement, for example, of transverse momentum, mass, width, yields, rapidity with a relatively small data sample. The particle ID performance has been found to have a significantly larger impact on the measurements of ϕ mesons in Pb-Pb collisions. Studies in this direction can be found in [15].

9.7 Conclusions and outlook

A performance study of the ϕ meson in proton-proton collisions has been described in this chapter. Special attention was paid on the effect of the particle identification in the measurement of the mass and the width of reconstructed ϕ meson signals after background subtraction. The reconstructed yields were also obtained. This study concluded that the like-sign method can be used for background subtraction in pp collisions. These results indicate that ALICE should be able to obtain a signal significance good enough to produce a publication by the end of the first week of data taking, assuming the particle identification is the main issue of the analysis during that period. This study concluded that this can only be achieved by using a relatively high transverse momentum cut on the charged track pair. Such a first publication on the ϕ can provide a first measurement of its mass and the width at LHC energies, as well as its transverse momentum distribution.

Further studies as a function of the event multiplicity are needed, because it is at high multiplicities where the ϕ meson can provide an insight into the role of the QGP phase transition in elementary collisions as described in chapter 8. Further studies will be needed to assess the use of high multiplicity triggers so that the ϕ meson study will remain part of the early physics programme in the ALICE experiment.

Conclusions

The role of ALICE in the LHC experimental programme is based on the most fundamental concepts of QCD physics. An insight into the novel aspects of heavy-ion physics at the LHC was given in this thesis. Although each chapter contains a conclusion section, a summary of them is given below.

A systematic test of cable signal transmission

A systematic test of cable transmission was carried out. This was achieved by using a specially modified version of the Local Trigger Unit (LTU) called a LVDS tester. This software allow us the calculation of bit-error rate measurements (BER). A rather sophisticated timing implementation was developed in order to calculate the uncertainties of the BER measurements (called “sampling window” determination). Measurements have demonstrated almost error-free transmission over cable lengths of up to 60 m, even without the use of an impedance equaliser circuit.

Lepton-pair production at central rapidities in pp collisions at $\sqrt{s} = 14$ TeV

Another study based on the use of the electromagnetic process $pp \to ppe^+e^-$ at central rapidities was carried out in order to investigate its use as a luminosity monitor in ALICE. The study looks at this process in the case where the e^+e^- pairs are produced at mid-rapidity ($|\eta| \leq 0.9$). An estimate of the signal-to-background of S/B > 0.26 at 95% Poisson confidence level was obtained for one normalised year of data taking. The outlines of future directions of this analysis were also discussed.

ϕ meson production in pp collisions at $\sqrt{s} = 14$ TeV

A physics performance study of ϕ meson production was carried out. This study includes a careful study of how the $\phi \rightarrow K^+K^-$ is reconstructed in the ALICE experiment with particular attention to particle identification. The combinatorial background for resonances, such as the ϕ meson, is expected to be extremely large at the LHC due to the high-multiplicity environment. The combinatorial background was successfully estimated using the like-sign method. This is a relevant result as it would be easier to perform it than the mixed-event method during LHC start-up. A preliminary study of the uncertainties in the predictions made by different currently available versions of the PYTHIA event generator was also carried out. This analysis concluded that there are discrepancies which come from the different estimations available of the charged particle multiplicity at low values of transverse momentum in the event. In pp collisions, a performance study of measurements of ϕ meson production during the first physics period of ALICE running, i.e. when particle identification is not tuned, demonstrated that measurement of ϕ production yields, and measurements of its mass and width will be possible, even with limited statistics. The estimations are that an early study of the ϕ meson can be carried out after one week of data taking at LHC startup estimated conditions.

The physics performance analyses discussed in this thesis will be carried out on the first dataset that the ALICE experiment is due to accumulate in pp collisions by the end of next year. Therefore, the results obtained in this thesis will be used by the LHC physics community in anticipation of the LHC start-up.

Appendix A

Luminosity measurement

For rare events with a small production cross-section, the number of interactions for a given process is an essential quantity. The concept of luminosity was introduced to describe such information by relating the cross-section and the number of interactions of a particular event. In other words, the luminosity gives information about the capabilities of a particle accelerator to produce the number of interactions required for a specific process. The event rate is given by

$$R = \mathcal{L} \cdot \sigma, \tag{A.1}$$

where L is the luminosity (in cm^{-2}s^{-1}), and σ is the cross-section for such process. The luminosity depends on the beam parameters, and the beam-beam interactions. It can be defined, assuming two oppositely directed beams of relativistic particles that overlap completely, as

$$\mathcal{L} = fn\frac{N_1 N_2}{A}, \tag{A.2}$$

where f is the revolution frequency, n is the number of bunches in either beam around the ring, N$_1$ and N$_2$ are the number of particles in each bunch and A is the cross-sectional area of the beams. The expected luminosity for ALICE is about 10^{31} cm^{-2}s^{-1} and 10^{27} cm^{-2}s^{-1} in pp and Pb-Pb collisions respectively (see table 3.2).

In order to estimate the luminosity, one can measure any of the following processes[1]:

- **The total cross-section and the inelastic cross-section**:

  By using the optical theorem [155], it is possible to obtain a relation between the rate of elastic events in the forward direction and the total rate of the pp collisions (R_{tot}). The TOTEM experiment will perform such a measurement to obtain the total cross-section at the LHC [78]. In other words, the total cross-section is measured by a luminosity-independent method:

  $$\sigma_{\text{tot}} = \frac{16}{1+\rho^2}\frac{(dN_{el}/dt)_{t=0}}{N_{el}+N_{inel}}, \tag{A.3}$$

  where ρ is the ratio of the real to the imaginary part of the forward elastic amplitude, and t is the Mandelstam variable t. The total cross-section can be measured with an absolute error of about 1 mb. A more detailed information about this method and its current status in the TOTEM physics programme can be found in various documents [78, 156].

  In ALICE, the event rate R can be obtained by multiplying the detector acceptance (Acc) to the total rate of the pp collisions. Thus, the luminosity can be measured and monitored from:

  $$\mathcal{L} = \frac{R}{Acc \cdot \sigma_{inel}}. \tag{A.4}$$

  The inelastic rate is in principle composed of the sum of the rates of the inelastic non-diffractive, the single-diffractive and the double-diffractive processes. Figure A.1 shows the detector acceptance in pseudo-rapidity for these processes. Experience at the Tevatron has indicated that the error in the detector acceptance can be reduced to a few per cent and the total uncertainty is dominated by the error in inelastic rate (about 5%) [4].

- **Z^0 and $W^{\pm}$ boson production**: In order to use a specific production process for luminosity measurement, its cross-section must be well-known. In other words, the uncertainties in the theoretical calculations should be similar to or better than the envisaged experimental accuracies. In recent years, both Z^0 and $W^\pm$ particle production have been considered to be key processes for luminosity control due to their clean signal and because their cross-sections are large, with theoretical calculations available at a good accuracy level.

- **The lepton-pair process** $pp \rightarrow pl^+l^-p$: As the ALICE experiment has not been designed to perform precision measurements of Z^0 and W^+W^- bosons, a study of the lepton pair (l^+l^-) production is needed to investigate the potential of this exclusive process as a luminosity monitor. Chapter 7 presents a novel study in this direction.

---

[1] A review of non-physics process methods, such as the "Van der Meer Scan" measurement, is not covered here (see references [20, 101]).

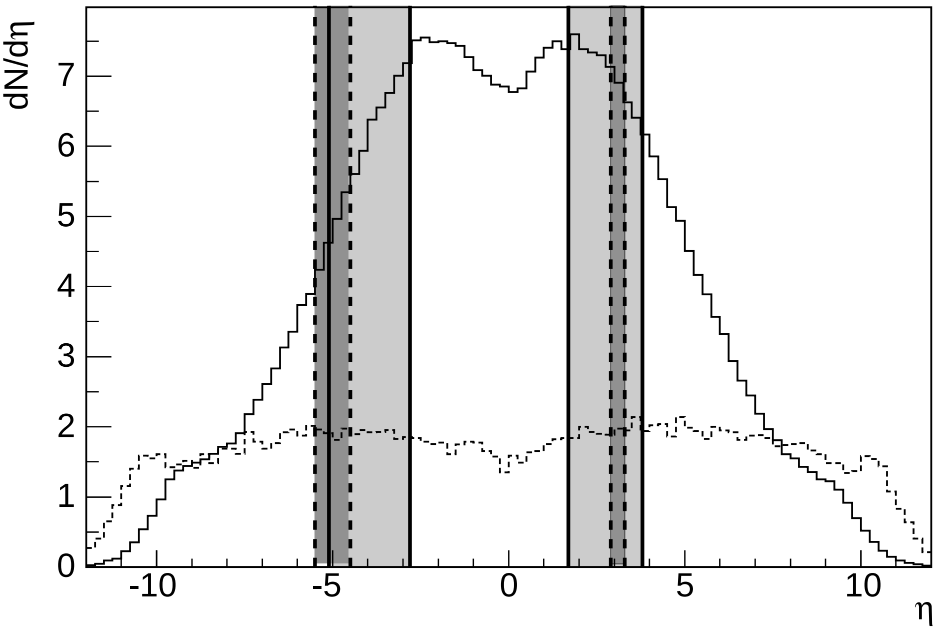

Figure A.1: Charged-particle pseudo-rapidity distribution for pp collisions at $\sqrt{s} = 14$ TeV from PYTHIA predictions. It includes the contribution of different interaction processes: inelastic non-diffractive (solid line), and diffractive interaction (dashed line). The vertical lines indicate the acceptance of the forward detectors V0 (solid line) and TO (dashed lines) [4].

Appendix B

Definition of the CTP time-parameters

Both the L0 and L1 trigger inputs from an event in a given bunch crossing (BC) arrive at the Central Trigger Processor (CTP) with a considerable delay, as shown in figure B.1. In section 4.3.1 we discussed all the trigger levels and their latencies, and it must be emphasised that each trigger input latency must include the trigger generation time in the front-end electronics and the signal transmission over the electrical cables (which as mentioned earlier, they are typically between 40 m to 60 m long). Therefore, for all the trigger levels a *maximum* value for the delay to the corresponding CTP input has been defined, as shown in table B.1.

Table B.1: Latencies associated with different trigger levels in the CTP.

Signal Status	L0 (μs)	L1 (μs)	L2(μs)
Last trigger input at CTP	0.8	6.1	87.6
Trigger output at CTP	0.9	6.2	87.7
Trigger output at detector	1.2	6.5	88.0

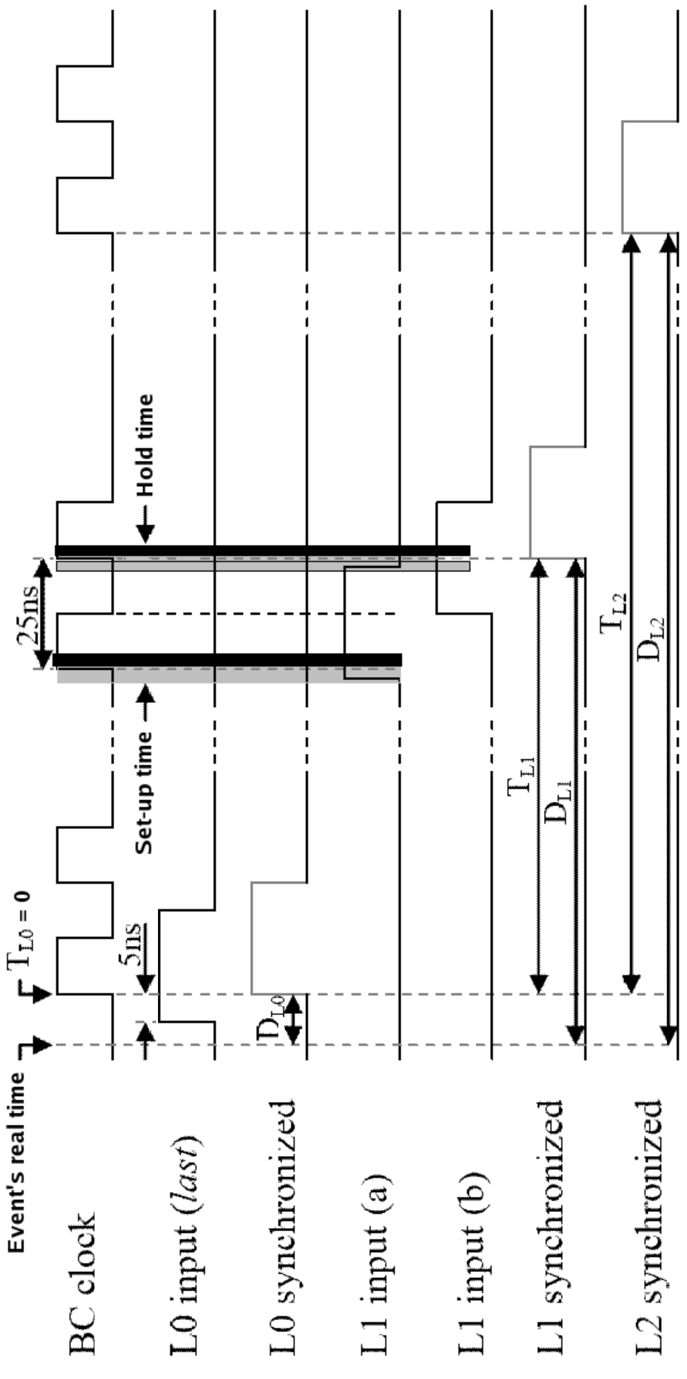

Figure B.1: Definition of the CTP time-parameters. The set-up time (grey range) and the hold time (black range) time interval are shown.

As a consequence of the values shown in table B.1, the local BC clock has to be adjusted in order to ensure that the last-arriving L0 trigger input is sampled with the active positive transition of the clock as early as possible. This then ensures that the L0 latency is the shortest possible value, but adopting at the same time a reasonable compromise delay (of 5 ns) in order to fulfil the set-up and hold time requirements. Hence, taking these considerations into account, a synchronised L0 trigger input will be delayed, say by a D_{L0} delay, in respect to the corresponding LHC bunch crossing event, as shown in figure B.1.

The principle of the synchronisation process used for the L1 and L2 trigger input is the same as mentioned for the L0 trigger input, i.e. if signal transitions violate the set-up (grey range) and hold-time (black range) requirements of the CTP's BC clock (see figure B.1), the signal is first registered with the negative edge of the clock, and then re-registered with the normal positive edge as shown in figure B.1 for the case of the L1 input (a). Otherwise, the signal is just clocked with the positive edge as shown in figure B.1 for the case of the L1 input (b). Notice that in both cases, the synchronised L1 trigger signal used by the CTP logic is delayed by the D_{L1} delay in respect to the corresponding LHC bunch crossing event. The synchronised L2 signal is carried out in the same way (D_{L2} delay).

In addition, in figure B.1 three other parameters are also shown: T_{L0}, T_{L1}, and T_{L2}. The first of them, T_{L0}, is the natural reference point for all the CTP time-settings because it defines the timing of the trigger levels. Therefore, T_{L1} and T_{L2} are defined in respect to the T_{L0} reference point and expressed in BC periods (25 ns).

References

[1] E. Witten, *Phys. Rev.* **D30**, 272–285 (1984).

[2] J. Letessier and J. Rafelski, Hadrons and Quark-Gluon Plasma, Cambridge University Press (2002).

[3] S. Margetis et al., *Ann. Rev. Nucl. Part. Sci.* **50**, 299–342 (2000).

[4] F. Carminati et al., *J. Phys.* **G30**, 1517–1763 (2004).

[5] S.A. Bull, Strange Particle and Antiparticle Production in Proton-Beryllium Interactions at 40 GeV/c at the CERN NA57 Experiment, PhD thesis, The University of Birmingham, UK, 2005.

[6] R. Hagedorn, *Nuovo Cim. Suppl.* **3**, 147–186 (1965).

[7] J. Rafelski, *Int. J. Mod. Phys.* **E16**, 813–828 (2007).

[8] C. Alt et al., *Phys. Rev.* **C75**, 064904 (2007).

[9] D. Miskowiec, *Nucl. Phys.* **A774**, 43–50 (2006).

[10] H. Helstrup, *J. Phys.* **G32**, S89–S95 (2006).

[11] R. Arnaldi et al., *J. Phys.* **G32**, S51–S60 (2006).

[12] T. W. Ludlam, *Nucl. Phys.* **A447**, 349c–369c (1986).

[13] N. P. Samios, *J. Phys.* **G34**, S181–S189 (2007).

[14] C. Hohne, *Nucl. Phys.* **A749**, 141–149 (2005).

[15] B. Alessandro et al., *J. Phys.* **G32**, 1295–2040 (2006).

[16] S. Weinberg, *Eur. Phys. J.* **C34**, 5–13 (2004).

[17] R. N. Cahn and G. Goldhaber, The Experimental Foundations of Particle Physics, Cambridge University Press (1989).

[18] R. K. Ellis, W. J. Stirling, and B. R. Webber, QCD and collider physics, Cambridge University Press (1996).

[19] S. Hands, *Contemp. Phys.* **42**, 209–225 (2001).

[20] S. Eidelman et al., *Phys. Lett.* **B592**, 1 (2004).

[21] W. J. Stirling, *Int. J. Mod. Phys.* **A20**, 5234–5243 (2005).

[22] S. Chandrasekharan et al., *Phys. Rev. Lett.* **82**, 2463–2466 (1999).

[23] R. Rapp and J. Wambach, *Adv. Nucl. Phys.* **25**, 1 (2000).

[24] K. Gottfried and V. F. Weisskopf, Concepts of Particle Physics. Vol. 2, Oxford University Press (1986).

[25] B. Müller, *Rept. Prog. Phys.* **58**, 611–636 (1995).

[26] A. Olchevski (Ed.), CERN 1999 European school of high-energy physics, (see K. Šafařík lecture, p. 267).

[27] S. P. Klevansky, hep-ph/9810399.

[28] R. D. Pisarski and F. Wilczek, *Phys. Rev.* **D29**, 338–341 (1984).

[29] G. E. Brown and M. Rho, *Phys. Rept.* **363**, 85–171 (2002).

[30] J. Rafelski and J. Letessier, *J. Phys. Conf. Ser.* **50**, 176–191 (2006).

[31] J. C. Collins and M. J. Perry, *Phys. Rev. Lett.* **34**, 1353 (1975).

[32] E. V. Shuryak, *Phys. Rept.* **61**, 71–158 (1980).

[33] R. Hagedorn and J. Rafelski, *Phys. Lett.* **B97**, 136 (1980).

[34] A. Chodos et al., *Phys. Rev.* **D9**, 3471–3495 (1974).

[35] A. Chodos et al., *Phys. Rev.* **D10**, 2599 (1974).

[36] B. H. Lavenda, *J. Phys.* **G34**, 2045–2051 (2007).

[37] L.D. Landau and E.M. Lifshitz, Statistical Physics (Third Edition, part 1), Butterworth Heinemann (2002).

[38] K. G. Wilson, *Phys. Rev.* **D10**, 2445–2459 (1974).

[39] M. Creutz, *Phys. Rev.* **D21**, 2308–2315 (1980).

[40] F. Karsch, *Nucl. Phys. Proc. Suppl.* **15**, 157–186 (1990).

[41] F. Karsch, *AIP Conf. Proc.* **842**, 20–28 (2006).

[42] F. Karsch, *Nucl. Phys.* **A698**, 199–208 (2002).

[43] S. Hands, *Nucl. Phys. Proc. Suppl.* **106**, 142–150 (2002).

[44] J. R. Ellis, *J. Phys. Conf. Ser.* **50**, 8–21 (2006).

[45] J. Rafelski and B. Müller, *Phys. Rev. Lett.* **48**, 1066 (1982).

[46] F. Antinori et al., *Nucl. Phys.* **A663**, 717–720 (2000).

[47] F. Antinori et al., *Eur. Phys. J.* **C14**, 633–641 (2000).

[48] H. Caines, *Nucl. Phys.* **A698**, 112–117 (2002).

[49] M. Lamont, *J. Phys. Conf. Ser.* **50**, 192–200 (2006).

[50] J. Rafelski and J. Letessier, *J. Phys.* **G35**, 044042 (2008).

[51] G. G. Barnafoldi et al., *J. Phys.* **G35**, 044057 (2008).

[52] A. Andronic et al., *Nucl. Phys.* **A772**, 167–199 (2006).

[53] G. Torrieri and J. Rafelski, *Nukleonika* **49**, S109–S114 (2004).

[54] J. Adams et al., *Phys. Lett.* **B612**, 181–189 (2005).

[55] C. Markert, *J. Phys.* **G35** 044029 (2008).

[56] S. Abreu et al., hep-ph/0711.0974.

[57] T. Matsui and H. Satz, *Phys. Lett.* **B178**, 416 (1986).

[58] R. Vogt, *Phys. Rept.* **310**, 197–260 (1999).

[59] M. C. Abreu et al., *Phys. Lett.* **B521**, 195–203 (2001).

[60] A. Adare et al., *Phys. Rev. Lett.* **98**, 232301 (2007).

[61] C. Adler et al., *Phys. Rev. Lett.* **89**, 202301 (2002).

[62] S. S. Adler et al., *Phys. Rev.* **C69**, 034910 (2004).

[63] B. B. Back et al., *Phys. Lett.* **B578**, 297–303 (2004).

[64] I. Arsene et al., *Phys. Rev. Lett.* **91**, 072305 (2003).

[65] D. A. Appel, *Phys. Rev.* **D33**, 717 (1986).

[66] J. Adams et al., *Phys. Rev. Lett.* **91**, 072304 (2003).

[67] N. Armesto et al., *J. Phys.* **G32**, S421–S427 (2006).

[68] B. I. Abelev et al., *Phys. Rev. Lett.* **98**, 192301 (2007).

[69] J. Ollitrault, *Phys. Rev.* **D46**, 229–245 (1992).

[70] P. Huovinen et al., *Phys. Lett.* **B503**, 58–64 (2001).

[71] P. Sorensen, *J. Phys.* **G30**, S217–S222 (2004).

[72] R. Snellings, *Eur. Phys. J.* **C49**, 87–90 (2007).

[73] A.J. Barr, Studies of Supersymmetry Models for the ATLAS Experiment at the Large Hadron Collider, D.Phil thesis, University of Oxford, UK, 2002.

[74] ATLAS: Letter of Intent for a General Purpose pp Experiment at the Large Hadron Collider at CERN, CERN-LHCC-92-04.

[75] A. Ball et al., *J. Phys.* **G34**, 995–1579 (2007).

[76] S. Barsuk, *Nucl. Phys. Proc. Suppl.* **156**, 93–98 (2006).

[77] O. Adriani et al., CERN-LHCC-2006-004.

[78] V. Berardi et al., CERN-LHCC-2004-020.

[79] H. D. Haseroth, Presented at the 16th Biennial Particle Accelerator Conference - PAC 95, Dallas, TX, USA, 1 - 5 May 1995.

[80] M. Gyulassy and X-N. Wang, *Comput. Phys. Commun.* **83**, 307 (1994).

[81] P. Cortese et al., CERN-LHCC-2003-062.

[82] G. Dellacasa et al., CERN-LHCC-99-12.

[83] G. H. Corral, *AIP Conf. Proc.* **674**, 200–212 (2003).

[84] P. Cortese et al., CERN-LHCC-2004-025.

[85] D. C. Zhou, *J. Phys.* **G34**, S719–S723 (2007).

[86] P. Cortese et al., CERN-LHCC-2006-014.

[87] R. Luchsinger and C. Grab, *Comput. Phys. Commun.* **76**, 263–280 (1993).

[88] E. J. Wolin and L. L. Ho, *Nucl. Instrum. Meth.* **A329**, 493–500 (1993).

[89] A. Dos Anjos et al., *IEEE Trans. Nucl. Sci.* **53**, 990–994 (2006).

[90] B. Frühwirth et al., Data Analysis Techniques for High-Energy Physics, Second Edition, Cambridge University Press (2000).

[91] O. Villalobos Baillie et al., Prepared for 11th Workshop on Electronics for LHC and Future Experiments (LECC 2005), Heidelberg, Germany, 12-16 September 2005.

[92] A. Bhasin et al., Presented at 15th IEEE Real Time Conference 2007 (RT 07), Batavia, Illinois, 29 Apr - 4 May 2007.

[93] S. Baron, Prepared for 11th Workshop on Electronics for LHC and Future Experiments (LECC 2005), Heidelberg, Germany, 12-16 September 2005.

[94] A. Jusko et al., Presented at 10th Workshop on Electronics for LHC and Future Experiments, Boston, Massachusetts, 13-17 Sep 2004.

[95] T.R. McCalla, Digital Logic and Computer Design, Macmillan Publishing Company (1992).

[96] Texas Instruments, LVDS Application and SLLD009 Data Handbook (2002).

[97] LVDS Transmission Tester Based on the LTU Board, http://www.ep.ph.bham.ac.uk/user/pedja/alice (2007).

[98] G. Amsel et al. *Rev. Sci. Instrum.* **42**, 8 (1971).

[99] R. Kowalewski et al., Evaluation of the Twisted Pair Data Transmission for the SCT, INDET-NO-172, 24 June 1997.

[100] M. Mandl, High-Density Digital Links, PhD thesis, Technical University of Vienna, Austria, 2000.

[101] D. Bocian, Luminosity Measurement of pp Collisions with the Two-Photon Process, PhD thesis, Polish Academy of Sciences, Poland, 2004.

[102] B. L. Caron, Luminosity Measurement at the Large Hadron Collider, PhD thesis, Alberta University, Canada, 2006.

[103] S. De Capua, Large Mass Dimuon Detection in the LHCb Experiment, PhD thesis, CERN-THESIS-2006-035.

[104] M. W. Krasny et al., *Nucl. Instrum. Meth.* **A584**, 42–52 (2008).

[105] A. G. Shamov and Valery I. Telnov, *Nucl. Instrum. Meth.* **A494**, 51–56 (2002).

[106] V. A. Khoze et al., *Eur. Phys. J.* **C19**, 313–322 (2001).

[107] S. P. Baranov et al., Proceedings, Physics at HERA, vol. 3 1478-1482. (see High Energy Physics Index 30 (1992) No. 12988).

[108] D. Bocian and K. Piotrzkowski, *Acta Phys. Polon.* **B35**, 2417–2424 (2004).

[109] P. Cortese et al., CERN-LHCC-2005-018.

[110] CERN Program Library Long Writeup W5013, GEANT Detector Description and Simulation Tool.

[111] T. Sjöstrand et al., hep-ph/0108264.

[112] C. Buttar et al., hep-ph/0604120.

[113] J. D. Jackson, *Nuovo Cim.* **34**, 1644–1666 (1964).

[114] M. Alston et al., *Phys. Rev. Lett.* **6**, 300–302 (1961).

[115] P. Fachini, *J. Phys.* **G30**, S735–S742 (2004).

[116] C. Markert, *J. Phys.* **G31**, S169–S178 (2005).

[117] P. Braun-Munzinger et al., *Phys. Lett.* **B518**, 41–46 (2001).

[118] J. Rafelski and J. Letessier, *Eur. Phys. J.* **C45**, 61–72 (2006).

[119] G. Torrieri and J. Rafelski, *Phys. Lett.* **B509**, 239–245 (2001).

[120] F. Antinori, *J. Phys.* **G35** 044055 (2008).

[121] J. Rafelski et al., *Phys. Rev.* **C72**, 024905 (2005).

[122] P. Koch et al., *Phys. Rept.* **142**, 167–262 (1986).

[123] S. A. Bass et al., *Nucl. Phys.* **A661**, 205–260 (1999).

[124] F. Klingl et al., *Phys. Lett.* **B431**, 254–262 (1998).

[125] M. Asakawa and C. M. Ko, *Nucl. Phys.* **A572**, 732–748 (1994).

[126] C. M. Ko and M. Asakawa, *Nucl. Phys.* **A566**, 447c–450c (1994).

[127] B. Batyunya et al., *Phys. Part. Nucl. Lett.* **2**, 110–115 (2005).

[128] S. Blyth, *J. Phys.* **G32**, S461–S464 (2006).

[129] S.S. Adler et al., *Phys. Rev.* **C72**, 014903 (2005).

[130] S. Afanasiev et al., *Phys. Rev. Lett.* **99**, 052301 (2007).

[131] N. Xu, *J. Phys.* **G35** 044031 (2008).

[132] R. Muto et al., *Phys. Rev. Lett.* **98**, 042501 (2007).

[133] F. Sakuma et al., *Phys. Rev. Lett.* **98**, 152302 (2007).

[134] S. V. Afanasev et al., *Phys. Lett.* **B491**, 59–66 (2000).

[135] M. C. Abreu et al., *Phys. Lett.* **B368**, 239–243 (1996).

[136] B. Alessandro et al., *Phys. Lett.* **B555**, 147–155 (2003).

[137] R. Arnaldi et al., *Eur. Phys. J.* **C49**, 255–260 (2007).

[138] A. Marin, *J. Phys.* **G31**, S1175–S1178 (2005).

[139] T. Alexopoulos et al., *Z. Phys.* **C67**, 411–416 (1995).

[140] O. Villalobos Baillie, *J. Phys.* **G31**, S701–S707 (2005).

[141] J. R. Ellis, *Nucl. Phys.* **A684**, 53–70 (2001).

[142] S. Chekanov et al., *Nucl. Phys.* **B718**, 3–31 (2005).

[143] A. Wroblewski, *Acta Phys. Polon.* **B16**, 379–392 (1985).

[144] F. Becattini et al., *Phys. Rev.* **C64**, 024901 (2001).

[145] B. Andersson, The Lund Model, Cambridge University Press (1998).

[146] J. Cleymans and K. Redlich, *Phys. Rev. Lett.* **81**, 5284–5286 (1998).

[147] J. D. Bjorken, *Phys. Rev.* **D27**, 140–151 (1983).

[148] M. R. Whalley et al., hep-ph/0508110.

[149] A. Moraes et al., *Eur. Phys. J.* **C50**, 435–466 (2007).

[150] T. Sjöstrand et al., hep-ph/0308153.

[151] R.J. Platt, Measurement of Ξ yield in NA57 and a Monte Carlo Study of the ρ Resonance at ALICE, PhD thesis, The University of Birmingham, UK, 2008.

[152] D. Drijard et al., *Nucl. Instr. Meth.* **A225**, 367 (1984).

[153] D. L'Hôte, *Nucl. Instrum. Meth.* **A337**, 544–556 (1994).

[154] F. James and M. Roos, *Comput. Phys. Commun.* **10**, 343–367 (1975).

[155] A. D. Martin, hep-ph/0103296.

[156] F. Ferro, *PoS* **DIFF2006**, 019 (2006).